ENGINEERING A BRAIN TUMOR MICROENVIRONMENT WITH CONTROLLED PHYSICAL FEATURES

A Dissertation
Presented to
The Academic Faculty

by

Jungeun Lim

Doctor of Philosophy in Mechanical Engineering
Joint Ph. D. Program with Seoul National University
George W. Woodruff School of Mechanical Engineering

Georgia Institute of Technology
August 2022

ENGINEERING A BRAIN TUMOR MICROENVIRONMENT WITH CONTROLLED PHYSICAL FEATURES

Approved by:

Dr. YongTae Kim, Advisor
George W. Woodruff School of Mechanical Engineering
Georgia Institute of Technology

Dr. Noo Li Jeon, Advisor
School of Mechanical Engineering
Seoul National University

Dr. Levi Wood
George W. Woodruff School of Mechanical Engineering
Georgia Institute of Technology

Dr. Yongdae Shin
School of Mechanical Engineering
Seoul National University

Dr. Tobey MacDonald
School of Medicine
Emory University

Dr. Hong Nam Kim
Brain Science Institute, Korea Institute of Science and Technology
Korea Institute of Science and Technology

Date Approved: April 28, 2022

To my family

ACKNOWLEDGEMENTS

First of all, I would like to express my sincere appreciation to my advisor in Seoul National University, Dr. Noo Li Jeon, for his mentoring and support for 6 years as a Ph.D. student. His priceless advice has led me to my career goal as a researcher. I also would like to express my deepest gratitude to my co-supervisor in Georgia Institute of Technology, Dr. YongTae Kim, for his support, invaluable advice and critical review of my research work. I also wish to thank my committee members, Dr. Tobey MacDonald, Dr. Levy Wood, Dr. Yongdae Shin, and Dr. Hong Nam Kim, for their insightful comments and encouragement on my research. I would like to express my appreciation to Dr. Sung Youb Kim, who always encourages me and gives valuable advice. I would also like to thank Dr. Jangho Kim, who provided priceless research experience with his deep insights.

I am also grateful to my lab members in Seoul National University and Georgia Institute of Technology. I would especially like to thank Stephen Rhee, my soulmate and great research partner. My Ph.D. journey would not have been possible without your help. I would like to extend my greatest gratitude to Dr. Jungho Ahn, Dr. Song Ih Ahn, Dr. Jeong-Kee Yoon, Dr. Jinhwan Kim, Dr. Bing Yu, Dr. Sunho Park, Hyeri Choi, and James Yu for their support and dedication to my research. I would not have come this far without you. I would like to extend my sincere thanks to my friends. I was the happiest student during my Ph.D. journey because of you.

Last but the most, my deepest appreciation goes to my family. I would like to express my heartfelt gratitude to my parents and my elder brother for their support and endless love. I am the luckiest daughter to have my beloved family.

TABLE OF CONTENTS

LIST OF TABLES

LIST OF FIGURES

LIST OF SYMBOLS AND ABBREVIATIONS

2D	Two-dimensional
3D	Three-dimensional
BBB	Blood-brain barrier
B-CSF-B	Blood-cerebrospinal fluid
BSA	Bovine serum albumin
ChP	Choroid plexus
CNS	Central nervous system
Con	Control
CSCs	Caner stem cells
CSF	Cerebrospinal fluid
DMEM	Dulbecco's Modified Eagle's Medium
ECM	Extracellular matrix
EGF	Epidermal growth factor
F+M	The mixture of fibrin and Matrigel
FE-SEM	Field emission scanning electron microscopy
FGF	Fibroblast growth factor
GAPDH	Glyceraldehyde 3-phosphate dehydrogenase
GFAP	Glial fibrillary acidic protein
HA	Human astrocytes
HBMEC	Human brain microvascular endothelial cells
HBVP	Human brain vascular pericytes
HCPEpiC	Human choroid plexus epithelial cells
HER2	Human epidermal growth factor receptor 2

JPA	Juvenile pilocytic astrocytoma
LM	Leptomeningeal metastasis
MGMT	Methylguanine-DNA methyltransferase
PFA	Paraformaldehyde
PDMS	Polydimethylsiloxane
PLL	Poly-L-lysine
PMA	Phorbol 12-myristate 13-acetate
PS	Polystyrene
PVN	Perivascular niche
RPMI-1640	Roswell Park Memorial Institute Medium-1640
TMZ	Temozolomide
Tras	Trastuzumab
VE-cad	Vascular endothelial cadherin
VEGF	Vascular endothelial growth factor
ZO-1	Zonula occluden-1

SUMMARY

Brain tumors account for nearly 90% of all central nervous system (CNS) tumors and are one of the deadliest types of cancer. Furthermore, brain metastasis, which is when cancer cells infiltrate into the brain, greatly increases the fatality rate and makes the cancer harder to treat. Advances in the field of neuro-oncology have unveiled previously unappreciated molecular characterizations and diverse therapeutic approaches to treat brain tumors. Despite these advances, methods assessing targets in preclinical and clinical studies are still very limited. Although many components of the brain tumor microenvironment such as dynamic fluid flow and a unique extracellular matrix have been studied and shown to contribute to the development of cancer, the mechanisms of these components have not been clearly unveiled. To tackle this problem, organ-on-a-chip technology has the capabilities to reconstruct the physiology of complex three-dimensional microenvironments as well as recreate their mechanisms. Previous studies have employed the technique to recapitulate the brain tumor microenvironment. However, biological components required for the physiological reconstruction of the brain tumor microenvironment were absent in the platforms. By using organ-on-a-chip technology, we developed a microfluidic platform that can recapitulate the key structure, function, and dynamic microenvironment of the human brain tumor microenvironment, including dynamic fluid flow, an engineered extracellular matrix, and complex cellular components such as microvasculature and an immune system. The goal of this thesis dissertation is to conduct anti-cancer drug screening using our physiologically relevant brain tumor organ-on-a-chip, allowing for efficient administration of tumor treatment to brain tumor patients.

CHAPTER 1. INTRODUCTION

1.1 Background

1.1.1 Brain tumor microenvironment

Primary brain and central nervous system (CNS) tumors represent a substantial cause of morbidity and mortality worldwide and are among the most lethal cancers [1, 2]. Particularly, pediatric brain tumors are the most common solid childhood tumors and the leading cause of childhood cancer-related death [3]. Cancer cells in other organs also migrate into the human brain, called brain metastasis, where tumor metastasis cause approximately 90% of cancer-associated death, and brain metastases occur in 15 – 20% of adults and 5 – 10% of children with malignancies [4, 5]. The vascular systems in the brain tumor microenvironment play an important role since the perivascular niche (PVN) is deeply related to prognosis and serves as a tumor-initiating cells' reservoir, while the vasculature provides the route for the metastasis (Figure 1) [6]. Among the various brain vascular systems, the capillaries in the choroid plexus (ChP) with its epithelium occasionally serve as the path for cancer cells infiltration toward cerebrospinal fluid (CSF) where the circulating cancer cells advance into the brain metastasis, called leptomeningeal metastasis (LM) [7]. Likewise, the brain tumor microenvironment consists of numerous affecting factors and complex mechanisms in its progression. However, the pathophysiology of the brain tumor microenvironment should be unveiled more for a better understanding and drug development.

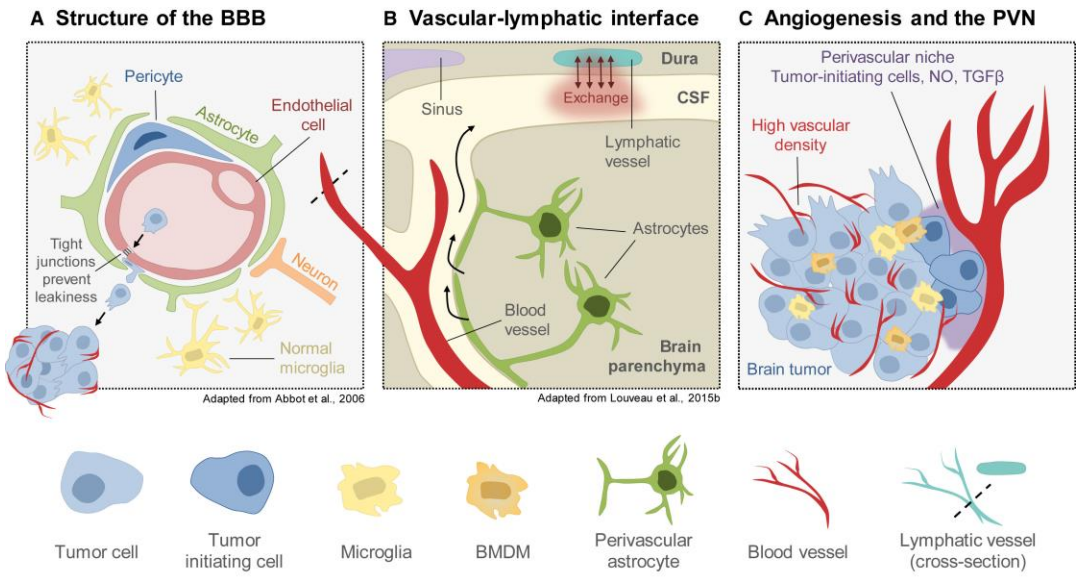

Figure 1. Brain tumor – vascular system interaction [6].

1.1.2 Physical traits in brain tumor microenvironment

Recently, the physics of cancer, which significantly affects cancer pathophysiology and its treatment, has been gaining attention (Figure 2) [8]. Extracellular matrix (ECM) is one of the key determinants of these physical properties. The ECM can vary solid stresses, stiffness, and geometry of the microenvironment [9-11]. The brain consists of distinctive ECM components including laminin, which can contribute to specialized physical features affecting its physiology [12-18]. In addition to the ECM, brain-specific biofluid such as CSF can influence fluid pressure in the brain microenvironment, which affects cancer development in the brain [19]. The flow dynamic also plays a critical role in tumor pathophysiology, affecting treatment response as well as tumor progression. [20, 21]. Despite the importance of the relationship between physical traits and oncology, a number of aspects of the relation are still unexplored.

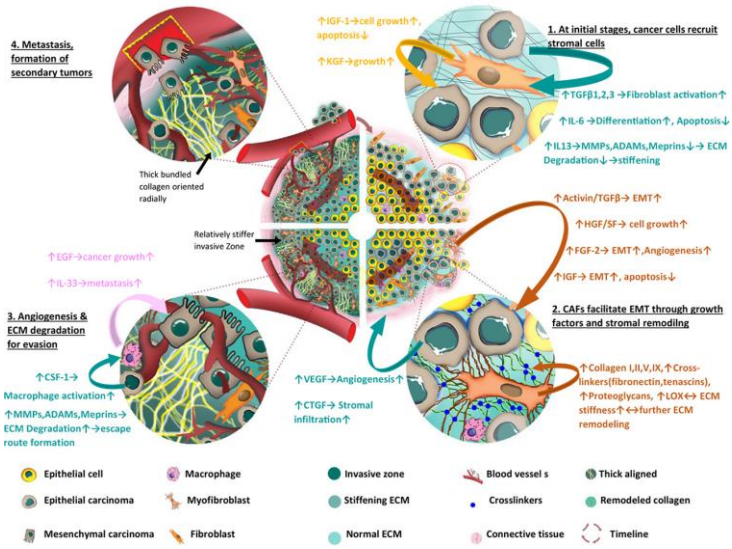

Figure 2. Schematic description of physical traits of cancer [22].

1.1.3 In vitro models of the human brain tumor microenvironment

Many research groups have contributed to the development of 3D preclinical cancer *in vitro* models for drug screening and the study of oncology [23]. Specifically, organoids, which are self-organizing 3D *in vitro* models to recapitulate certain organs using stem cell technology, are commonly utilized in cancer research [24]. Though these organotypic models have enabled recapitulating many crucial pathophysiological factors and *in vivo*-like drug responses, they have not been able to recreate dynamic stimulation and 3D complex architecture of organs with crucial parts such as vasculature and an immune system [25, 26]. To date, organ-on-a-chip technology has contributed to reconstructing the complex physiology of three-dimensional tumor microenvironments [27, 28]. Organ-on-a-chip models enable the application of dynamic flow and the construction of complex multilayered 3D structures using microfluidic technology [29]. Many preclinical brain

tumor models reconstitute the brain tumor microenvironment by taking advantages of this innovative technology, especially to mimic brain tumor-vasculature pathophysiology. Several microfluidic platforms have been developed for the investigation of tumor migration in the brain barrier system, which recapitulate brain metastasis by constructing brain endothelial barriers with tumor migration while subjected to dynamic flow (Figure 3a, b) [30, 31]. However, these models lack brain-specific ECM components and an immune system. Yi et al. developed a glioblastoma-on-a-chip using a 3D printed microfluidic platform by utilizing decellularized ECM and conducted drug screening (Figure 3c) [32]. Though this model reconstructed glioblastoma-vasculature structure with brain-specific ECM, dynamic flow and immune constituents were not recapitulated. Other research groups reconstructed the interaction between brain tumor stem cells and vasculature using microfluidic devices (Figure 3d, e) [33, 34]. The behaviors of brain tumor stem cells were deeply examined through the platforms, but these models failed to recreate the brain-specific ECM, fluidic stimulation, and immune reactions of the brain tumor microenvironment. Likewise, though various 3D *in vitro* models recapitulating the brain tumor microenvironment have elucidated unrevealed neuro-oncology and drug mechanisms, many challenges in mimicking the pathophysiology still remain.

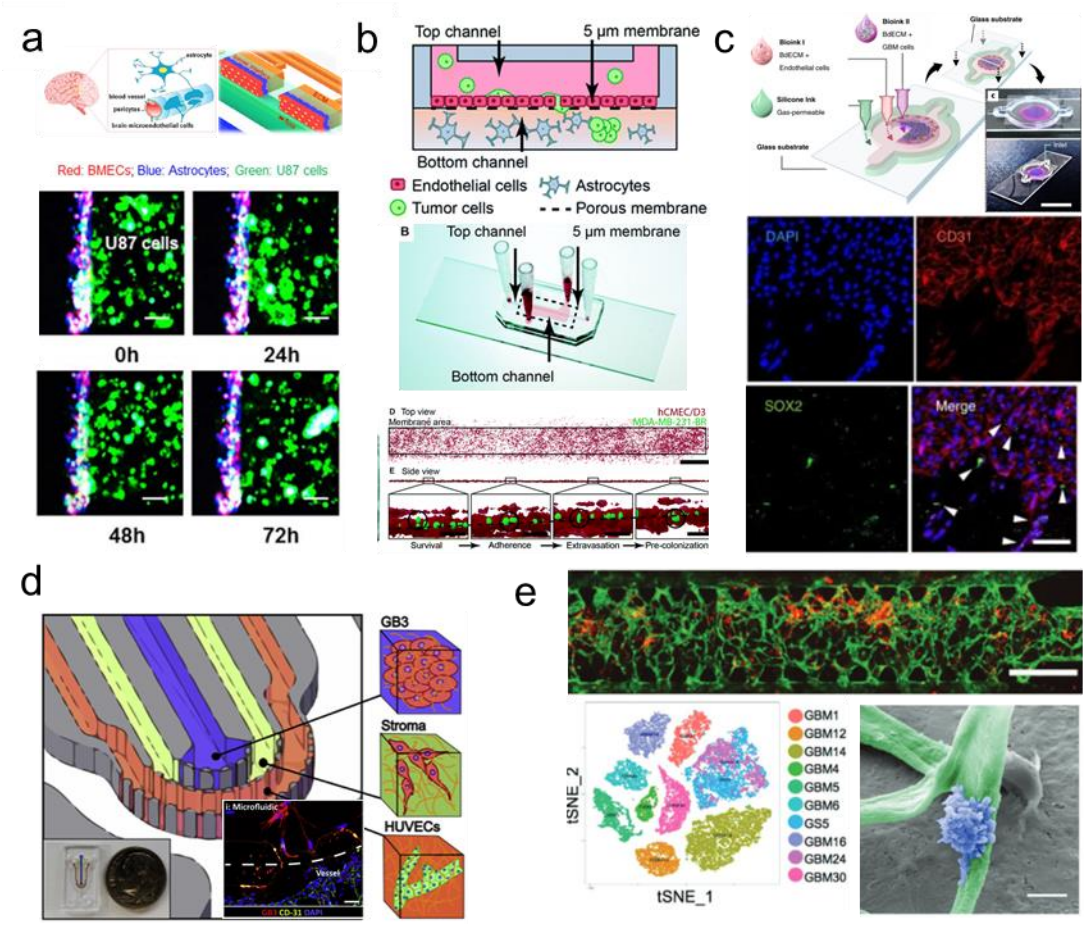

Figure 3. Brain tumor-vasculature interaction recapitulated in microfluidic platforms. (a) A blood-brain barrier model to mimic brain metastasis with dynamic flow [30]. (b) An artificial intelligence-based analysis platform to investigate brain metastasis [31]. (c) A bioprinted glioblastoma-on-a-chip for chemotherapy testing [32]. (d) A microfluidic device to mimic glioma stem cells-vascular interactions [33]. (e) A glioblastoma-microvasculature-on-a-chip [34].

1.1.4 Understanding therapeutics and immune system for brain tumor / metastasis

Advances in neuro-oncology have allowed various types of therapeutic methods to target specific mechanisms such as immune reactions and receptors of cancer cells in the brain microenvironment have been widely developed [35-37]. However, more studies on

the resistance mechanisms to the targeting drugs are still needed to treat the brain tumor microenvironment. One of the reasons a lack of understanding of this resistance mechanism exists is the lack of preclinical models to reconstitute physiological relevance. For instance, the perivasulcar niche (PVN) functions as a cancer stem cell (CSC) reservoir which creates cytotoxic drug resistance, but few preclinical brain cancer tools have recreated the characteristics of this component [38, 39]. Moreover, few robust *in vitro* preclinical models faithfully recapitulate the brain tumor microenvironment with an immune system, and this lack of an immune microenvironment leads to the inability to examine the response of cancer cells to immunotherapy [40].

1.1.5 Needs for physiologically relevant in vitro human brain models for the understanding of neuro-oncology

Few preclinical *in vitro* tools recapitulating the brain tumor microenvironment recreate specific microarchitecture and characteristics of the human brain. For instance, to recapitulate the human ChP, not only does the distinct multi-layered structure with capillaries need to be recreated, epithelium integration, brain-specific ECM composition, and dynamic stimulation exposure by CSF flow, also need to be taken into consideration [41]. Due to the difficulty in reconstituting the physiology, it has been challenging to developing a powerful preclinical tool enabling the investigation of pathophysiology and the therapy testing in human ChP. In previous cases, the disparities in drug response between the human ChP and preclinical tools led to clinical trial failures [42]. For example, the use of BIA 10-2472, which is a fatty acid amide hydrolase inhibitor used to treat chronic pain and multiple sclerosis, was halted during phase 1 clinical trials due to fatal neurotoxicity related to the response in the ChP [43-45]. There have been attempts with

pervious preclinical *in vitro* models that addressed these limitations [46, 47]. Recently, Pellegrini et al. developed a ChP organoid that recapitulated blood-CSF barrier (B-CSF-B) properties and functioned to successfully produce CSF (Figure 4a) [46]. Furthermore, they were able to reproduce an *in vivo*-like drug response in the ChP organoids similar to those from clinical trials. However, though the organoid model was able to recreate these critical characteristics of the ChP barrier, it lacked a vascular system as well as an immune microenvironment which are crucial to its physiology. Also, tumor modelling was absent in this organoid model. Moreover, the group did not recreate *in vivo*-like CSF dynamic stimulation, which is a main component of ChP physiology. Another group reconstructed a neurovascular unit under the CSF effect using organ-on-a-chip technology, through which the group was able to successfully reconstruct the complex 3D structure and introduce breast cancer cells to recreate a brain tumor microenvironment (Figure 4b) [47]. This neurovascular-unit-on-a-chip represented BBB contact with brain parenchyma and was used for stroke modeling and stem cell therapy testing. However, although this microfluidic model included a CSF channel, it was not able to fully represent ChP and CSF dynamics. Few *in vitro* models have been developed that can investigate ChP physiology while under CSF flow dynamics, which is required for a better understanding of ChP physiology [48]. The recapitulation of a brain tumor microenvironment with this specialized tissue is necessary for the development of drugs targeting this system.

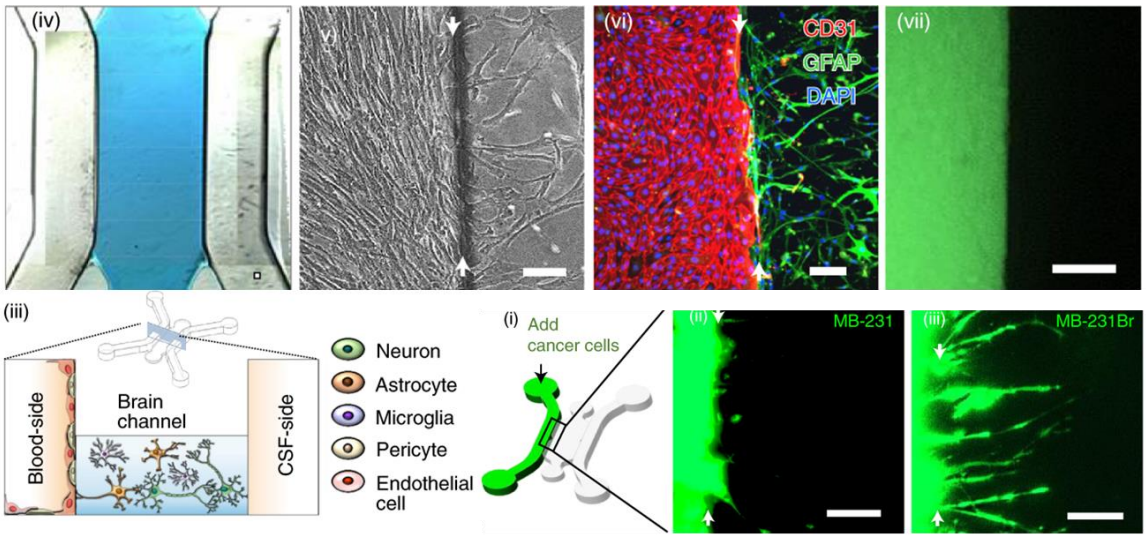

Figure 4. Human ChP *in vitro* preclinical models. A neurovascular-unit-on-a-chip to reconstruct the human ChP for disease modeling [47].

1.2 Research Objectives

The lack of reliable preclinical models that recapitulate the brain tumor microenvironment is one of the primary reasons drug development for primary brain tumor treatment and brain metastases have such high failure rates. Therefore, the need for accurate brain tumor microenvironmental models is rapidly growing to study unexplored neuro-oncology. To enable the development of physiologically relevant preclinical tools, several crucial features of the brain tumor microenvironment need to be recreated: dynamic fluid flow, brain-specific ECM, and complex cellular components such as microvasculature and an immune system. Currently, no preclinical *in vitro* models allow for high-throughput drug screening or recapitulate these essential traits of the brain tumor microenvironment.

The main goal of this work is to develop human brain tumor/metastasis *in vitro* models, which recapitulate critical physiological factors in the brain tumor microenvironment. One of the platforms, a microvascularized pediatric brain tumor-on-a-chip, utilizes engineered ECM and an integrated microvascular system to enhance its physiological relevance and capabilities as a drug screening platform. The second platform, a human ChP-on-a-chip, contains several more features in its design that increased its physiological relevance. Firstly, the physical design of the microfluidic device enables the construction of a multi-layered capillaries – epithelium complex representative of the ChP. Furthermore, the ChP is cultured in an engineered brain-specific ECM and is also subjected to *in vivo*-like CSF flow within the device. Finally, drug response and immune reaction can be modelled using the microfluidic chip by recreating breast cancer metastasis into the ChP system. All in all, these models to recapitulate the human brain microenvironment can be powerful tools through which the pathophysiology and drug response can be reliably predicted.

1.3 Thesis Outline

To achieve the primary objectives, the study is divided into the following aims:

Aim 1: Develop a microfluidic platform for brain modeling

- Design a microfluidic platform to reconstruct the human ChP
- Establish design rules for the microfluidic liquid patterning of the platform
- Validate and characterize the device as a co-culture system

Aim 2: Engineer physical features of the brain microenvironment

- Engineer a brain-specific ECM for an *in vivo*-like brain tumor microenvironment
- Recreate *in vivo*-like CSF flow in the brain microenvironment
- Validate the physiological relevance of the human ChP / brain tumor microenvironment

Aim 3: Recreate a brain tumor microenvironment for drug screening

- Recapitulate tumor metastasis in the ChP model
- Conduct anti-cancer drug testing using the microfluidic model
- Reconstruct tumor – immune interactions in the ChP model

CHAPTER 2. MICROVASCULARIZED PEDIATRIC BRAIN TUMOR-ON-A-CHIP FOR HIGH-THROUGHPUT DRUG SCREENING

2.1 Introduction

Pediatric brain tumors are the most common solid childhood tumors and the leading cause of childhood cancer-related death [3]. Advances in the field of pediatric neuro-oncology have contributed to unveiling previously unappreciated molecular characterizations and developing diverse therapeutic approaches to treat pediatric brain tumors [49-51]. Despite these advances, functional assessments of targets in preclinical and clinical studies are still limited. Specifically, though a number of brain tumor compositions including perivascular niche (PVN) and cancer stem cells (CSCs) have been considered to considerably contribute to the development of cancer and the key target to treat brain cancer, the mechanism has not been clearly unveiled [6, 52, 53]. Although the regimens to treat adult brain tumors are often applied to pediatric brain tumors treatment, the approach is ineffective due to the key biological differences between tumors in adults and children [54]. Furthermore, aggressive therapies for pediatric brain tumor treatment often lead to poor quality of life. The lack of preclinical models that can reliably investigate the mechanisms of pediatric brain tumors hinders the precise clinical translation of therapeutics [55]. Although animal preclinical models for pediatric brain tumors have been developed, there are many limitations due to the species differences [56, 57]. Diverse types of pediatric brain tumor *in vitro* models, such as cell lines [58] and tumorspheres [59], have been developed, but no models recapitulate three-dimensional human pediatric brain tumor

microenvironment consisting of the critical components: microvascular system, CSCs, and surrounding stromal cells [60]. To overcome these challenges, the development of clinically applicable pediatric brain tumor models is required, which reconstitute its complex physiology [61].

To date, organ-on-a-chip technology has contributed to reconstructing the complex physiology of the three-dimensional tumor microenvironment [27]. Previous studies employed the technique to recapitulate chemotaxis of medulloblastoma cells, a common type of childhood brain tumor [62, 63]. Nevertheless, physiologically related components in the pediatric brain tumor microenvironment including microvasculatures, other stromal cells, CSCs, and extracellular matrix (ECM) required for the recapitulation were absent in the platforms. The adjustment of ECM and nutrients for *in vitro* culture has been required to co-culture each essential component of the specific microenvironment with its physiological relevance. In previous studies, microvasculature cultured in a 3D microfluidic system was generally constructed in fibrin gel [64, 65]. Fibrin allows endothelial cells to proliferate and configure a microvascular network [66]. However, this hydrogel is inappropriate for tumor microenvironment culture due to the lack of ECM components such as laminin to support perivascular cells [12-14] and because of its quick degradation which makes long-term cell culture difficult [67]. Particularly, HBMECs contract during fibrin clotting and lysis, which leads to failure in the vascular organization [68]. To address this limitation of fibrin, ECM engineering utilizing fibrin with other hydrogels has been suggested [69, 70]. While the construction of 3D self-assembled microvascular networks in Matrigel is difficult, Matrigel incorporates factors including laminin that contribute to the physiological relevance of the brain tumor microenvironment

that allows for CSC differentiation [14] and stabilize the vascular architecture [71, 72]. To take advantage of both hydrogels, mixing of the different ECM compositions has been employed [73, 74]. Moreover, this strategy to mix fibrin with other factors has been known to stabilize vascularization by controlling scaffold degradation [67]. A previous study showed that a fibrin-Matrigel mixture induced promoted neurite extension, enhanced neuron proliferation, and elongated angiogenic sprouts of HBMECs [73]. However, this study did not demonstrate the physiological relevance of other brain stromal cells such as astrocytes or pathophysiological application like brain tumors in the adjusted ECM microenvironment. Moreover, this previous study employed polydimethylsiloxane (PDMS) to fabricate the platforms, which is inappropriate for drug testing due to small particle absorption and has a low throughput [75, 76].

Beyond engineering ECM for microvasculature construction, hydrogel was adjusted to accommodate the function and morphology of brain tumor composing cells such as astrocytes [77], stem cells [74], and brain cancer cells [78]. In the case of astrocytes, the brain microenvironment preserves *in vivo*-like physiological characteristics of astrocytes such as downregulated glial fibrillary acidic protein (GFAP) expression during a quiescent state, which requires supporting ECM components [79-81]. Matrigel has been applied to stem cell and organoid culture since it is known to contain ECM components including laminin to derive stem cells differentiation and maintain their function [82-86]. For instance, Shravanthi Rajasekar et al. constructed vascularized colorectal organoids by taking advantage of Matrigel for organoid culture and fibrin for vasculature culture [74]. Normally, cancer cells demonstrate increased invasiveness through their branched morphology with extended filopodial actin [87]. In particular, medulloblastoma cells, one

of the pediatric brain tumors derived from neuronal precursor cells, demonstrate morphological and functional similarity to the origin, showing ramified structure during their differentiation [87-89]. Furthermore, cancer cells remodel those ECM factors during tumor progression, enabling them for invasion by allowing navigational extension of filopodial actin [90]. Likewise, it is critical to enhance physiological relevance by engineering ECM compositions to recapitulate pediatric brain tumors *in vitro*.

Here we present a recapitulated microvascularized pediatric brain tumor system in a microfluidic chip with engineered ECM and patient pediatric brain tumor tissues. The adjustment of ECM using fibrin and Matrigel, whose components support stem cell differentiation and brain stromal cells growth [84], allow for the improvement of physiological relevance: astrocytes with a low level of GFAP expression, CSCs in patient tumor tissues with frequent cystic expansion, and pediatric cancer cells in more *in vivo*-like ramified morphology. When patient pediatric brain tumor tissues were microvascularized in the engineered culture environment, they demonstrated their features, respectively, where the characteristics of each microvasculature considerably affect the therapeutic approach [91, 92]. For instance, it has been known that the human meningioma patient tissue demonstrates higher microvascular density than the density of low-grade astrocytoma tissue [93]. As one of the common properties, blood vessels in brain tumors are known to demonstrate more downregulated junction protein expression including VE-cadherin than normal vasculature [94-96]. The microvasculature co-cultured with childhood meningioma and low-grade astrocytoma patient tissues showed decreased transmembrane junction proteins compared to normal brain microvasculature, while a higher microvascular network density in meningioma compared to that in astrocytoma was

observed in the adjusted microenvironment. Microvascularization in this pediatric brain tumor-friendly microenvironment using primary human brain microvascular endothelial cells (pHBMEC) enabled *ex vivo* on-chip patient tissue microvascularization with the expression of the *in vivo*-like characteristics.

CSCs are tumor-originating cells with self-renewing and differentiating abilities in brain tumor tissues, which contribute to chemoresistance and recurrence [38, 39]. CD133, one of the most reliable and typical CSCs markers as a transmembrane glycoprotein, has been known to inhibit apoptosis leading to chemoresistance [97, 98]. For instance, evasion of cytotoxicity in CD133-positive CSCs was investigated during a typical brain tumor chemotherapy treatment, TMZ. [99, 100]. TMZ-resistance may be induced by highly upregulated methylguanine-DNA methyltransferase (MGMT) levels derived by CD133-positive CSCs, which neutralizes genotoxicity by TMZ in a suicidal process restoring DNA integrity by direct repair [100]. The CSCs are preferentially distributed in the PVN and closely interact with the vascular area, where the CD133-positive cells are localized at the niche, and the CD133 expression can be acquired from tight interaction between cancer cells and the vascular region [101, 102]. The localization of the marker has been known to be induced by factors secreted by the endothelial cells in the PVN that preserve the brain CSC reservoir [101]. We demonstrated the upregulated chemoresistance marker CD133 and the resistance to the typical chemotherapeutics TMZ in the reconstituted PVN of patient astrocytoma tissues in our platform.

Our model reconstructs microvascularized pediatric brain solid tumors with physiological relevance and may contribute to efficient drug screening and a better understanding of the pathology and physiology of pediatric brain tumors.

2.2 Results and Discussions

2.2.1 Adjustment of ECM to reconstruct brain microvasculature

Our human microvascularized brain pediatric brain tumor-on-a-chip recapitulates childhood brain tumor microenvironments in the adjusted ECM, allowing physiological relevance in the engineered microfluidic culture condition (Figure 5). In this study, we employed a microfluidic chip previously designed for high-throughput drug screening to develop the *in vitro* pediatric brain tumor model (Supporting information, Figure S1) [103]. This model incorporates microvasculature, which is critical in pediatric neuro-oncology due to its relationship with the perivascular niche (PVN) [104]. To reconstruct human brain microvasculature, which can orchestrate with functional stromal cells in pediatric brain tumors, we adjusted the culture condition of the microenvironment: media and ECM. We utilized the media cocktail previously modulated for the key brain cellular culture including brain microvascular endothelial cells, pericytes, and astrocytes to build the microvasculature [105]. To validate the culture of pediatric brain cancer cells in a media cocktail for the co-culture system, we conducted viability tests for typical medulloblastoma cell lines: DAOY and D556 (Supporting information, Figure S2). We demonstrated that both medulloblastoma cell lines are viable in the media cocktail. The viability assay for the medium selection showed significantly lower viability of D556 than DAOY in the serum-deficient culture, astrocyte medium, and pericyte medium (Supporting information, Figure S2). This can present the physiological feature that a mutant p53 contributes to the suppression of apoptosis in serum-starved medium while p53-wild type tumor has no

suppression of cell death in the serum-deficient condition, where DAOY is a p53-mutant cell line, and D556 is a p53-wild type cell line [61, 106].

Beyond adjusting the medium components, ECM was engineered using fibrin conventionally utilized for vasculature culture and Matrigel containing the essential ECM components required for constructing the brain microvasculature, where the approach to mix fibrin with other components can increase stability in vascularization by controlling scaffold degradation [16, 67].

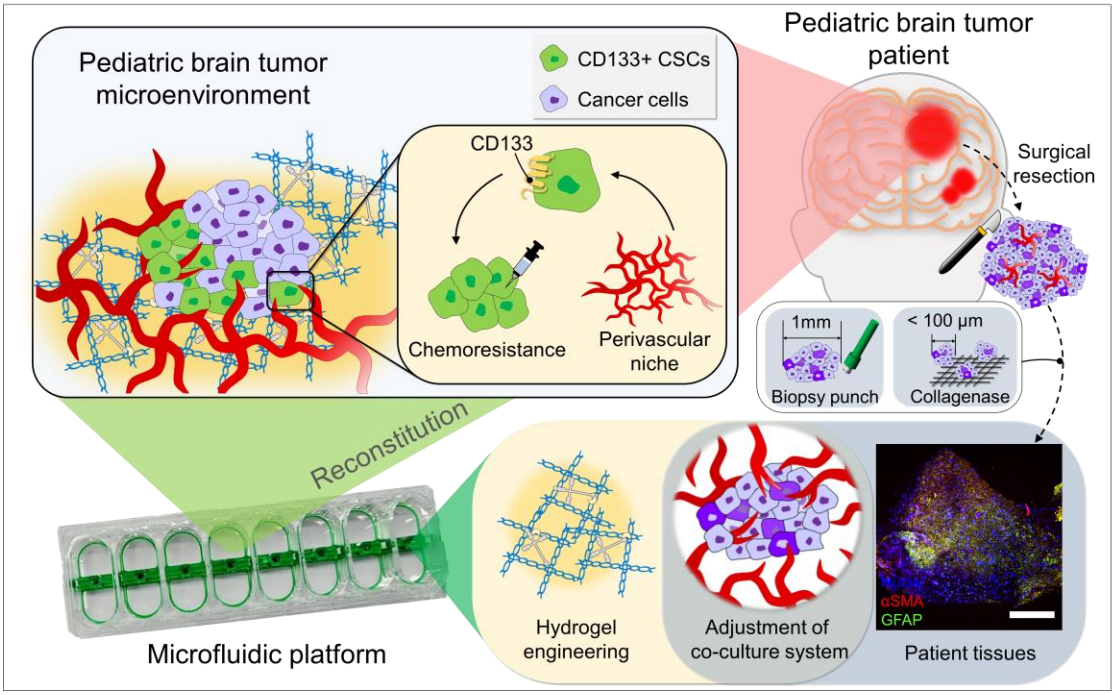

Figure 5. Engineered microenvironment to construct microvascularized pediatric brain tumor environment. Schematic description of reconstructed pediatric brain tumor microenvironment in the microfluidic platform consisting of patient pediatric brain tumor tissues by adjusting microenvironmental components. Representative confocal images of DAPI (blue), αSMA (red), and GFAP (green) of 1 mm JPA (juvenile pilocytic astrocytoma) patient tissue extracted through tissue biopsy (Scale bar: 400μm) (right-bottom). Photograph of the microfluidic device to culture pediatric tumor microenvironment (left-bottom).

We investigated the engineered ECM for the co-culture system, F+M (fibrin : Matrigel = 2 mg/ml : 2 mg/ml), comparing with each gel component. The architecture of each ECM condition presented that F+M incorporates each structural feature of both hydrogels: fibrillar fibrin and sponge-like Matrigel (Supporting information, Figure S3). In addition, the F+M was most stiff compared to each fibrin (2 mg/ml) and Matrigel (2 mg/ml) by showing the highest storage modulus, which might provide the stable matrix to embed the cells (Supporting information, Figure S4). We cultured pHBMECs in the microfluidic chip to construct brain microvasculature in each culture condition for four days (Supporting information, Figure S5). We cultured the brain microvasculature in each ECM condition: fibrin, F+M, and Matrigel. In addition, the microvasculature was cultured in endothelial cell medium and the adjusted co-culture medium, respectively.

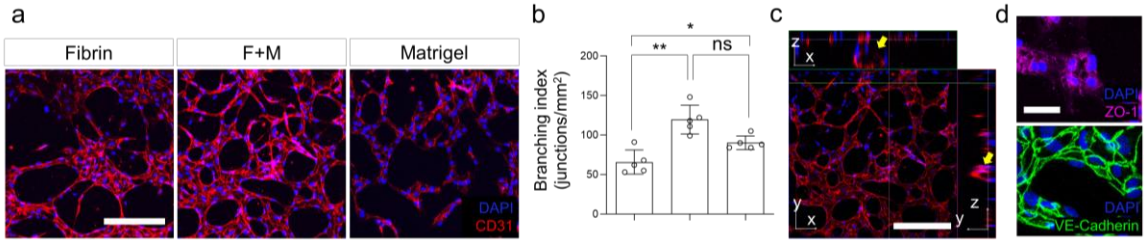

Figure 6. Hydrogel engineering to enhance the physiological relevance of brain microvasculature. (a) Immunostaining of CD31 expression of microvasculature cultured in fibrin, F+M (1:1 mixture of fibrin and Matrigel), and Matrigel respectively, when the media cocktail was supplied to the microvasculature (CD31, red; DAPI, blue) (Scale bar: 200 μm). (b) Branching index extracted by quantifying the number of junctions of CD31 expressing microvascular network, when cultured in each engineered condition (n = 5 for each condition). (c) A microvascular structure cultured in F+M mixture and E+G cocktail (CD31, red; DAPI, blue (Scale bar: 200μm). Yellow arrows indicate the lumen structure of the microvasculature. d Confocal microscopy images of adherens junction VE-Cadherin (green) and tight junction ZO-1 (magenta) when cultured in F+M mixture and E+G media cocktail (Scale bar: 50 μm).

The microvascular network built in F+M showed a significantly increased branching index than those cultured in other ECM conditions (Figure 6a, b, Supporting information, Figure S6, 7). The confocal images of the microvascular network constructed in F+M using the media mixture showed the presence of lumen structure as well as the expression of junction proteins such as VE-cadherin and ZO-1 (Figure 6c, d). These results suggest that the brain microvasculature with the highly interconnected network can be built in the adjusted culture condition, F+M with the media cocktail. Here we have shown that the engineered microenvironment utilizing fibrin-Matrigel mixture and co-culture media cocktail allowed for the highly branched brain microvasculature with junction proteins expression.

2.2.2 ECM engineering for in vivo-like culture of pediatric brain tumor tissues and its stromal cells

Not only is the microvasculature critical to recapitulating the childhood brain tumor microenvironment, perivascular components such as astrocytes, CSCs, and tumor cells are also crucial for the reconstruction. Specifically, pediatric brain tumor tissue incorporates CSCs that contribute to anti-cancer drug resistance by driving tumor growth and recurrence, which is essential to investigate pediatric brain tumor progression [107]. Nevertheless, it has been challenging to construct microfluidic culture conditions to preserve the physiological and morphological properties of the perivascular composition as well as microvasculature in developing *in vitro* pediatric brain tumor models [60, 108]. To overcome the limitations, we investigated the physiological relevance of astrocytes, CSCs in patient pediatric brain tumor tissues, and pediatric brain cancer cells by analyzing their morphology or specific protein expression.

When the astrocytes were cultured in each ECM condition in the microfluidic platform, they demonstrated significantly downregulated GFAP expression in F+M and Matrigel culture condition compared to fibrin culture condition (Figure 7a, b). To validate the CSCs growth, we quantified the rounded cystic expansion in the pediatric brain tumor tissues, which can be the morphological response of the stem cell differentiation by presenting the colony formation [86]. Juvenile pilocytic astrocytoma (JPA) patient tissues were applied to the *ex vivo* culture in the microfluidic platform. The samples for the chip loading were prepared by biopsy punching or collagenase dissociating the extracted tissues from surgical resection, as shown in Supporting information, Figure S8. The expression of nestin, the neuronal stem cell marker, indicates that the patient tissue consists of stem cells (Supporting information, Figure S9). Other cellular components were observed via immunostaining of the several proteins expressed in biopsy punched JPA patient tissues: CD31, a platelet-endothelial cell adhesion molecule, α-Smooth muscle actin (α-SMA), a marker for an activated fibrogenic cellular subset, and GFAP (Figure 5). We quantified the frequency of cyst construction derived from stem cell differentiation in the dissociated patient tissues when cultured in each ECM (Figure 8a, b). Colony formation efficiency was significantly higher when the ECM consisted of Matrigel than fibrin in the absence of Matrigel (Figure 8b).

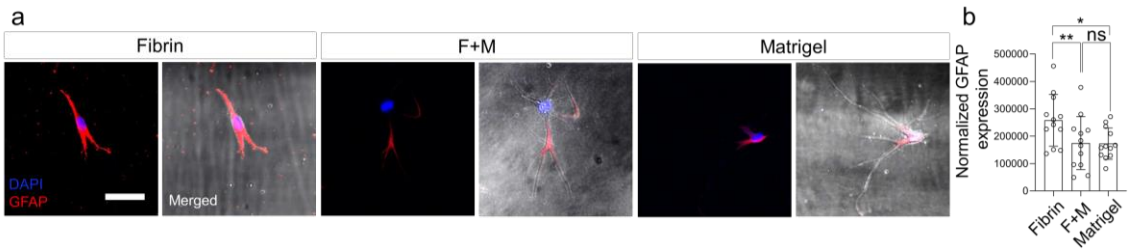

Figure 7. GFAP expression of astrocytes cultured in fibrin, fibrin and Matrigel mixture, and Matrigel. (e) Representative confocal images of DAPI (blue) and GFAP (red) of astrocytes (Scale bar: 50μm). (f) Normalized GFAP expression of astrocytes, which is the ratio of the average fluorescence per pixel in the cell (cell body and processes) to the average intensity of the gel background (n = 13 for each condition).

In the case of pediatric brain tumor cell culture, D556 and DAOY, the medulloblastoma cell lines, exhibited remarkably branched morphology when cultured in F+M and Matrigel relative to fibrin by showing significantly decreased cell body size and increased process length and degree of branching (Figure 8c-e). Furthermore, when the structure of D556 was compared to that of DAOY in the F+M culture condition, D556 demonstrated a significantly lower degree of branching and process length than DAOY (Supporting information, Figure S10). These findings suggest that the ECM components in Matrigel might contribute to the stabilization of astrocytes and stem cell differentiation in pediatric brain tumor tissues, which can be related to the physiological relevance in anti-cancer drug resistance induced by stem cell behavior. Moreover, these results suggest pediatric brain tumor cells express their morphological features by showing ramified structure close to neuronal cellular shape when cultured in the ECM consisting of Matrigel, which also can present their metastatic features.

Here we have shown that the engineered microenvironment utilizing fibrin-Matrigel mixture and co-culture media cocktail allowed for the downregulated the GFAP expression of astrocytes, cystic expansion of CSCs in patient pediatric brain tumor tissues,

and the ramification of pediatric brain tumor cells. In detail, the downregulated GFAP expression in astrocytes indicates their *in vivo*-like stable state in the culture condition [79-81]. In addition, cystic expansion in the patient pediatric brain tumor tissues characterized the CSCs differentiation in the microenvironment [86]. Furthermore, the ramified morphology of medulloblastoma cells, DAOY and D556, presents physiological relevant characteristics when cultured in the adjusted microenvironment [87-89]. More filopodial extension presented from D556 than the one shown in DAOY indicates that D556, group3 subtype medulloblastoma cell line, is more metastatic than DAOY, SHH subtype medulloblastoma, which is one of the behavioral properties of each medulloblastoma subtype [58, 87, 90]. We suggested that the *in vivo*-like features of astrocytes, pediatric brain cancer cells, and pediatric brain tumor tissues were shown in the engineered ECM.

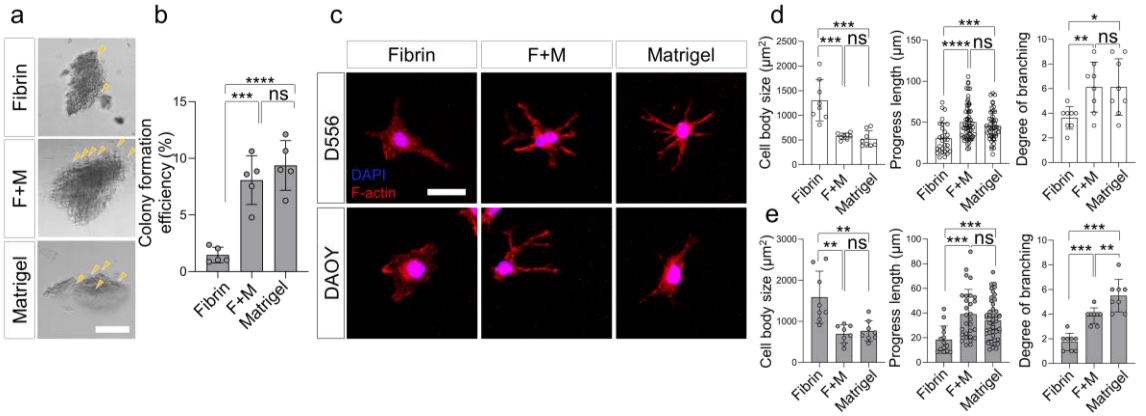

Figure 8. Hydrogel engineering to enhance the physiological relevance of microvascularized pediatric brain tumors. (a) Representative brightfield images of JPA patient tissue aggregates extracted through collagenase IV digestion cultured in fibrin, fibrin and Matrigel mixture, and Matrigel. (Scale bar: 100μm). (b) Quantification of the colony formation efficiency of the patient tissue aggregates cultured in fibrin, fibrin and Matrigel mixture, and Matrigel (n = 5 for each condition). (c) Representative confocal images of DAPI (blue) and CellMask membrane stain (red) of D556 and DAOY cell line, respectively. d, e Quantification of cell body size (n = 8 for each condition), process length (n = 14-63 for each condition), degree of branching (n = 8 for each condition) of (d) D556 and (e) DAOY cell line. (*p < 0.05 , **p<0.01 ***p<0.001 and ****p<0.0001 by student t-test. Data represent mean ± s.d.)

2.2.3 Microvascularized Patient Pediatric Brain Tumor Tissues in the Microfluidic Chip

The validation conducted in the previous sections in the microengineered platform enabled the reconstruction of microvascularized pediatric brain solid tumors. By employing the approach, we demonstrated that our microvascularized patient pediatric brain tumor tissue-on-a-chip represents the typical pathophysiological characteristics in each type of brain tumor vasculature. To recapitulate the microvascularized pediatric brain tumor, 1 mm biopsy punched pediatric brain tissues were cultured with the HBMECs in the engineered culture condition as shown in Supporting information, Figure S11. The microvessel density was significantly higher when the microvasculature was cultured with the meningioma patient tissue than when the microvessels were cultured with the grade I astrocytoma sample (Figure 9a-d, Supporting information, Figure S12). Furthermore, we performed a quantitative analysis of the VE-cadherin expression on the microvasculature that was significantly downregulated on the microvasculature cultured with the pediatric brain tumor tissues of both types compared to the normal brain microvasculature cultured without tumor tissues (Figure 10a, b, Supporting information, Figure S13). These results suggest that childhood brain tumors might induce the phenotypic change of the brain vasculature such as the structure and junction protein expression, which was reconstituted in our engineered microenvironment.

In this platform, the microvasculature co-cultured with patient pediatric brain tumor tissues demonstrated downregulated VE-cadherin expression and lower microvascular density in astrocytoma microvasculature than the medulloblastoma one. Interestingly, the astrocytoma tissues in PVN showed increased CD133 and decreased viability when exposed to a typical chemotherapeutics called TMZ, compared to the one absent with the

PVN. The validation of physiological relevance for each constituent contributed to the well-constructed microvascularization with the patient pediatric brain tumor tissues in our platform. Specifically, human microvasculature in the meningioma patient brain presented higher microvascular density than the low-grade astrocytoma patient, which is also recapitulated in our model [93]. Also, the decreased VE-cadherin expression in the co-culture microvasculature with patient pediatric brain tumor tissues indicated the *in vivo*-like feature in the tumor vasculature [94-96].

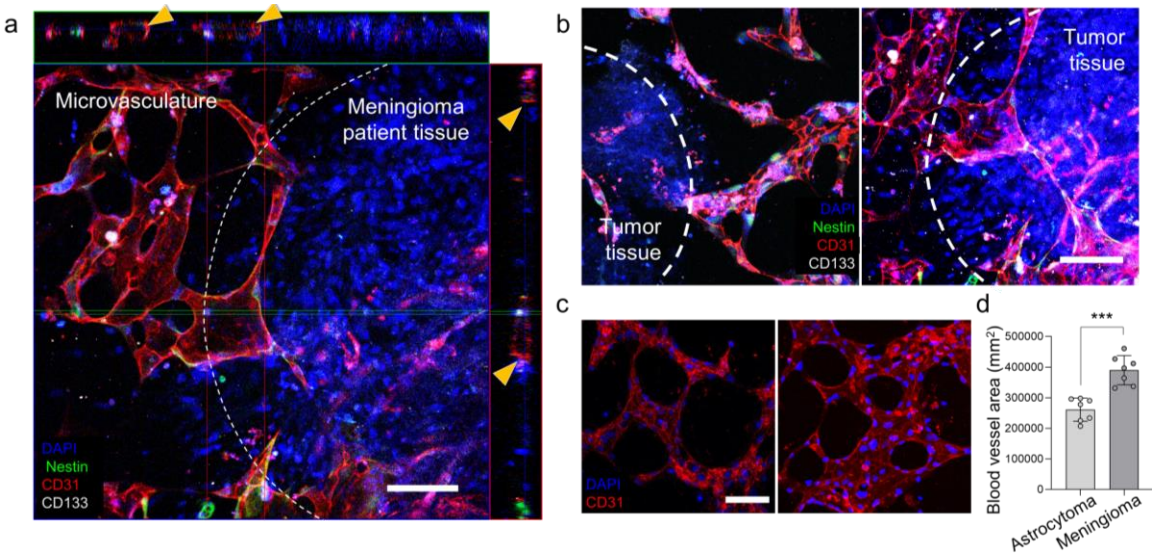

Figure 9. Microvascularized patient pediatric brain tumor tissues in the engineered microenvironment using the microfluidic chip. (a) Representative confocal images of microvascularized meningioma tissues, respectively (Scale bar: 100 μm). DAPI on patient tumor tissues (blue), nestin (green), CD31 (red), and CD133 (gray) of microvasculature-tumor tissues contact region. b, c Representative confocal images of microvascularized astrocytoma and meningioma tissues, respectively (Scale bar: 100 μm). (b) DAPI on patient tumor tissues (blue), nestin (green), CD31 (red), and CD133 (gray) of microvasculature-tumor tissues contact region and (c) DAPI (blue) and CD31 (red) of microvasculature region. (d) Blood vessel area in ROI of microvasculature cultured with each pediatric brain tumor tissue (n = 7 for each condition, ***$p<0.001$ by student t-test. Data represent mean ± s.d.).

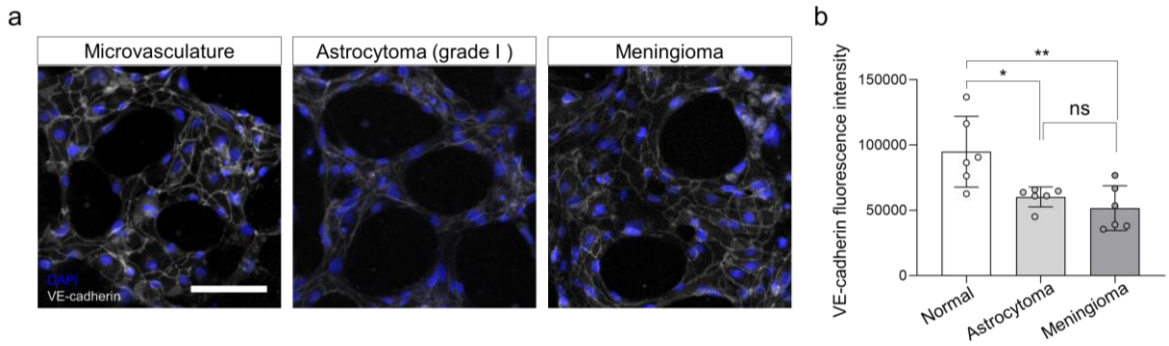

Figure 10. VE-cadherin expression on brain microvasculature cultured without tumor tissues, with astrocytoma, and with meningioma tissues. (a) Representative confocal images of DAPI (blue) and VE-cadherin (gray) expressed on each brain microvasculature (Scale bar: 100 μm). Yellow lines on the images represent the region used for the plot profile analysis. (b) Quantification of mean fluorescence intensity of VE-cadherin expression (n = 6 for each condition, *p < 0.05 , **p<0.01 by student t-test. Data represent mean ± s.d.).

2.2.4 Expression of a Prognostic Marker and Chemoresistance of Pediatric Brain Tumor Tissues in PVN

We co-cultured the patient astrocytoma tissues dissociated using collagenase IV with the endothelial cells in our developed culture system to investigate the regional CD133 expression on the brain tumor aggregated in the PVN (Supporting information, Figure S14). In the platform, the patient astrocytoma tissue aggregates highly expressed CD133 when surrounded by the microvasculature, while the dissociated tissues without the endothelial cover showed significantly lower CD133 expression (Figure 11a-c). Beyond investigating the upregulated CD133 expression on the perivascular region in the platform, we compared the chemotherapeutic response in the microvascularized astrocytoma tissue to avascular one. We conducted the viability assay after applying 250 μM TMZ to the co-culture system of the biopsy-punched patient astrocytoma tissue and the endothelial cells and only astrocytoma tissue-embedded platform, respectively, for the comparison

(Supporting information, Figure S15). The concentration of TMZ was determined by referring to the therapeutic window indicated in the previous *in vitro* studies [32, 109-111]. When TMZ was applied to the co-culture microenvironment of the microvascularized astrocytoma tissue, there was no significant change in the viability of the astrocytoma-loaded section compared to the one in the absence of TMZ application (Figure 11d). On the other hand, the viability was significantly decreased when TMZ was treated on the avascular culture condition of the astrocytoma tissue compared to the one without TMZ treatment (Figure 11d). These results revealed that our microfluidic model allowed for the recapitulation of the chemoresistant perivascular pediatric brain tumor with its chemoresistance marker expression, which indicates the physiological relevance in the pediatric brain tumor microenvironment.

Beyond reconstituting the properties in the microvasculature of pediatric brain tumors, we also recapitulated the features expressed on the tumor tissue in PVN. It has been known that CSCs with CD133 expression are distributed on the brain tumor tissues in PVN [97, 98, 101, 102], and are closely involved with chemoresistance [99, 100], where our model reconstituted the essential characteristics. Overall, our findings have highlighted that our microfluidic model can recapitulate the physiological relevance in the pediatric brain tumor microenvironment, which can provide drug screening results of human pediatric brain tumor therapeutic.

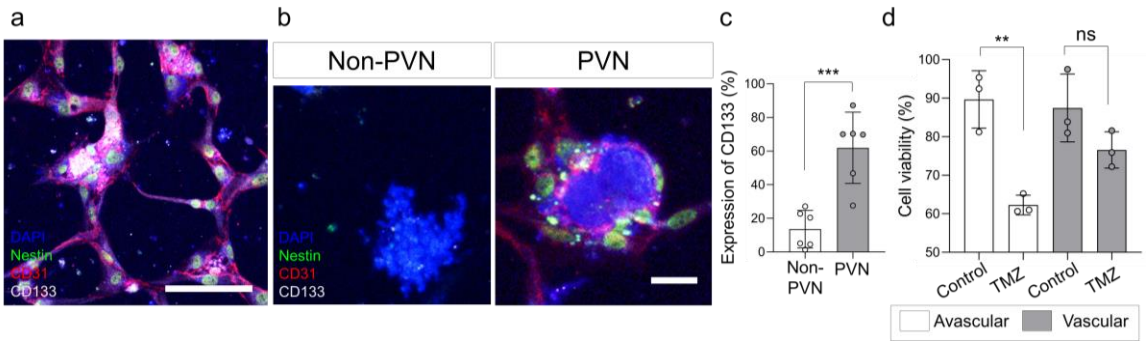

Figure 11. CD133 expression and chemoresistance in microvascularized astrocytoma tissues in the engineered microenvironment using the microfluidic chip. a, b Representative confocal images of DAPI (blue), nestin (green), CD31 (red), and CD133 (gray). (a) microvascularized astrocytoma tissues. (b) astrocytoma tissue in the non-PVN and PVN (perivascular niche) region, respectively. (c) CD133 expression on astrocytoma tissues in the non-PVN and PVN regions, respectively. (n = 6 for each condition, ***$p<0.001$ by student t-test. Data represent mean ± s.d.) (d) Quantification of the viability assay for tumor tissue cultured in TMZ-treated and non-treated condition, respectively (n = 3 for each condition, **$p<0.01$ by student t-test. Data represent mean ± s.d.)

2.3 Conclusions

In this work, we developed an *in vitro* model of microvascularized pediatric brain tumors, which recapitulates the key physiological relevant features of pediatric brain tumors. Our model also allows for *ex vivo* culture of patient pediatric brain tumor tissues with their microvascularization for increasing physiological relevance including the anti-cancer drug resistance marker and the drug response. We believe that our human pediatric brain tumor model could contribute to the development of childhood brain tumor therapeutics as well as pediatric neuro-oncology in particular for the physiology related to the microvasculature.

2.4 Materials and Methods

Fabrication of the microfluidic plastic chip. Polystyrene (PS) injection molding was pe rformed at an R&D Factory (Korea). The aluminum alloy mold core was processed by ma chining and polishing. At the time of injection, the clamping force was set at 130 tons wit h a maximum injection pressure of 55 bar, 15 seconds of cycle time, and a 220 °C nozzle temperature. The substrate was bonded to the injection-molded PS part to complete the de vice.

Hydrogel preparation and patterning. To convert the hydrophobic PS surface to hydro philic, the surface of the chips was irradiated with oxygen plasma using a plasma treatme nt system (Harrick Plasma, Ithaca, NY, USA) for 5 min. The microchannel was patterned with hydrogel. Before filling the microchannel, 40 μL mixture of cells and bovine fibrino gen solution (Sigma, USA; 2 mg mL^{-1}) with 0.8 μL of bovine thrombin (Sigma, USA; 0.5 U mL^{-1}), bovine fibrinogen solution (Sigma, USA; 2 mg mL^{-1}) and Matrigel (Corning, U SA; 2 mg mL^{-1}) with 0.8 μL of bovine thrombin (Sigma, USA; 0.5 U mL^{-1}), and Matrige l (Corning, USA; 2 mg mL^{-1}), respectively, was prepared. The mixture was introduced int o the microchannel by injecting it through the central hole. The cocktail media supplemen ted with vascular endothelial growth factor (VEGF; Peprotech; 50 ng mL^{-1}), fibroblast gr owth factor (FGF; Gibco; 20 ng mL^{-1}), epidermal growth factor (EGF; Peprotech; 20 ng mL^{-1}) was prepared. After allowing 20 min for the patterned mixture to cross-link in an in cubator at 37 °C in 5% CO_2, likewise, 200 μL of the medium was loaded in each reservoir after 3 min for cross-linking. The medium was daily changed.

Pediatric brain tumor tissue extraction. Tumor tissues were collected according to Chil dren's Healthcare of Atlanta-approved protocols. Informed consent was obtained from all

patients.

Cell culture. Primary human brain microvascular endothelial cells (HBMEC; Sciencell; # 1000) at passage 4–5 were maintained in endothelial cell medium (Sciencell, San Diego, CA, USA) on flasks coated with 50 μgmL−1 fibronectin (Sigma-Aldrich). Human brain v ascular pericytes (HBVP; Sciencell; #1200) and human astrocytes (HA; Sciencell; #1800) were cultured on 1mg mL−1 poly-L-lysine (PLL, Sigma-Aldrich) coated flasks and main tained in astrocyte and pericyte medium, respectively (Sciencell). Both primary cells betw een passages 3 and 5 were used for all experiments. Fibronectin and PLL coating procedu res were achieved following the manufacturer's instruction. The cells were maintained in an incubator at 37 °C in 5% CO_2 for 3 days. D556 and DAOY cells were obtained from th e ATCC and cultured in Dulbecco's Modified Eagle's Medium (DMEM) including 10% f etal bovine serum (HyClone, USA) and 1% penicillin–streptomycin (Gibco, USA).

Rheological property measurement. The mechanical properties of gels were measured by rotational rheometer (TA instrument Ltd., DHR-1, Delaware, USA) equipped with par allel plate (25 mm diameter) at a gap height of 1 mm. Fibrin (2 mg/mL), F+M, and Matrig el (2 mg/mL), respectively was placed on the plate of the rheometer. The storage modulus (G') and loss modulus (G") were measured using strain sweeping mode with frequency fi xed at 1 rad/s at 25 °C.

Preparation for Gels for Scanning Electron Microscopy. To prepare for the fibrin gels, 2 mg/ ml bovine fibrinogen (Sigma) was dissolved in PBS (Gibco) and aprotinin (0.15 U /ml, Sigma) supplemented in the solution. Fibrin and Matrigel mixture was prepared by di ssolving 2 mg/ml fibrinogen and 2 mg/ml Matrigel (Corning) in PBS and aprotinin supple mented in the solution. Matrigel was diluted to 2 mg/ml in PBS.

Fixation and Dehydration of Gels for Scanning Electron Microscopy. The field emiss ion scanning electron microscopy (FE-SEM) was used to observe the microstructure of fi brin gels. SEM investigation of the microstructure was conducted through critical point dr ying and platinum coating of samples. The constructs were washed in PBS, then fixed in a 2% glutaraldehyde solution for 2h. And the constructs were washed in 0.05 M sodium c acodylate buffer for 10 min, and the washing step was repeated washing step is repeated t wice. Fixation was followed with 1% osmium tetroxide for 1 h at 4 °C. Then, fixed sampl es were dehydrated through a series in 30, 50, 70, 80, 90, 100 (× 3) ethanol solutions for 1 0 min each. Subsequently, dehydrated samples were placed in a critical point dryer (Leica EM CP300, Germany), and ethanol was replaced with CO_2 and removed. The dried samp les were mounted on aluminum stubs, sputter-coated with platinum, and examined by FE-SEM (S-5000, Hitachi).

Immunocytochemistry. The immunofluorescence imaging was performed to visualize ce ll-specific marker expression. The cell membrane was stained with CellMask deep red (In vitrogen) and the samples for the cell membrane staining were fixed with 4% (w/v) parafo rmaldehyde (PFA; Santa Cruz Biotechnology, San Diego, CA, USA) in PBS (Gibco, US A) for 10 min. The samples except for the cell membrane staining were fixed with 4% (w/ v) PFA (Santa Cruz Biotechnology, San Diego, CA, USA) in PBS (Gibco, USA) for 15 m in at RT, followed by permeabilization in 0.1% Triton X-100 (Sigma-Aldrich) for 15 min. The samples were then treated with 3% bovine serum albumin (BSA; Sigma-Aldrich) for 1 h. The following antibodies were used for immunocytochemistry: AlexaFluor 594 conj ugated mouse anti-CD31 (1:200; BioLegend), Alexa Fluor 647 conjugated anti-mouse VE -cadherin (1:200; BioLegend), goat anti-ZO-1 (1:200; Abcam, Cambirdge, MA, USA), m

ouse anti-GFAP (1:200; Invitrogen, Carlsbad, CA, USA), AlexaFluor 488 conjugated rab bit anti-α-SMA (1:200; Abcam), AlexaFluor 488 conjugated mouse anti-Nestin (1:200; In vitrogen), rabbit anti-CD133 (1:200; Invitrogen), 4,6-diamino-2-phenylindole (DAPI; 1:1 000; Invitrogen). hen samples were incubated with fluorescence conjugated secondary ant ibodies: donkey anti-goat AlexaFluor 633 (1:200; Invitrogen), chicken anti-mouse AlexaF luor 594 (1:200; Invitrogen), and donkey anti-rabbit AlexaFluor 647 (1:200; Abcam)) for overnight at 4 °C for the target visualization. Fluorescently visualized samples were exam ined using a confocal microscope (LSM 700, Carl Zeiss, Oberkochen, Germany).

Viability testing. The live/dead viability test was conducted using a kit with calcein AM (0.5:1000) and ethidium homodimer-1 (0.5:1000) for media composition testing and TMZ response testing, respectively. In the media composition testing, D556 and DAOY cells were seeded at 8×10^3 cell/ well in 96-well plate for 48 hours in 200 μL of each media co mposition: DMEM including 10% fetal bovine serum and 1% penicillin–streptomycin (D), Endothelial cell medium (E), Astrocyte medium (A), Pericyte medium (P), Microglia m edium (M; Sciencell), E + G (E:A:M = 1:1:1:1), and E + P + G (E:P:A:M = 1:1:1:1). Flu orescently visualized live/dead signals were examined using a confocal microscope (LSM 700, Carl Zeiss, Oberkochen, Germany). The viability of the astrocytoma tissue was qua ntified by imaging the signals through the hole where the 1 mm tissue was loaded.

Statistical image analysis. Fiji (http://fiji.sc.), open access software, was used to analyze confocal images of each target visualization. Confocal 3D images were converted to 2D i mage by z-projection, then cropped to defined region of interest. To analyze the morpholo gy of D556 and DAOY cells, the boundaries of cells were obtained automatically using m agic wand tool on the maximal intensity projection image. In the case of measuring VE-c

adherin intensity, the mean intensity values were corrected for background differences by dividing the measured intensities with the average intensity of a cell-free region in each section, while the plot profile analysis was applied to measure the cross-sectional intensity of VE-cadherin expression. The images for the area measurement are then converted to binary masked images by applying same condition of threshold. Finally, the area of the visualized targets including microvascular density, CD133 and GFAP expression was measured using Fiji directly and branching index was measured using Angiotool [112] (National Cancer Institute). All statistical analyses performed unpaired Student's t-test to obtain statistical comparisons of analyzed values. The p value thresholds for statistical significance were set and represented in the graph as *$p < 0.05$; **$p < 0.01$; ***$p < 0.005$; ****$p < 0.001$.

2.5 Supplementary Information

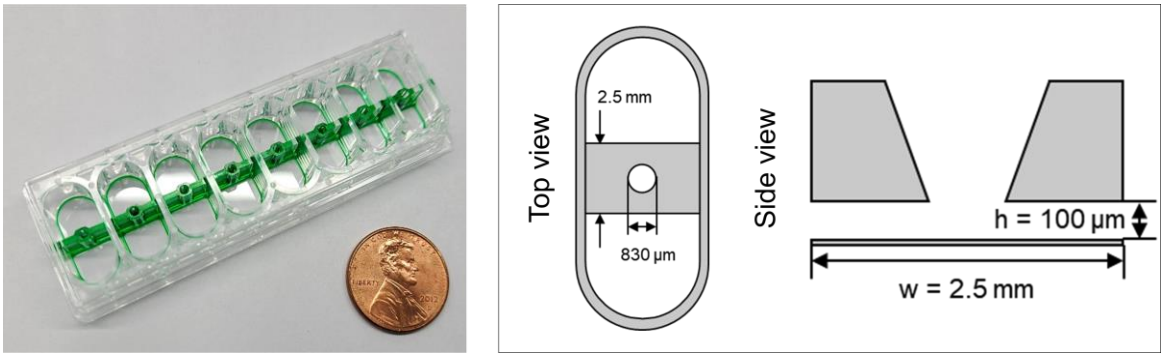

Figure S 1. Photograph and schematic description of the microfluidic device to culture pediatric tumor microenvironment.

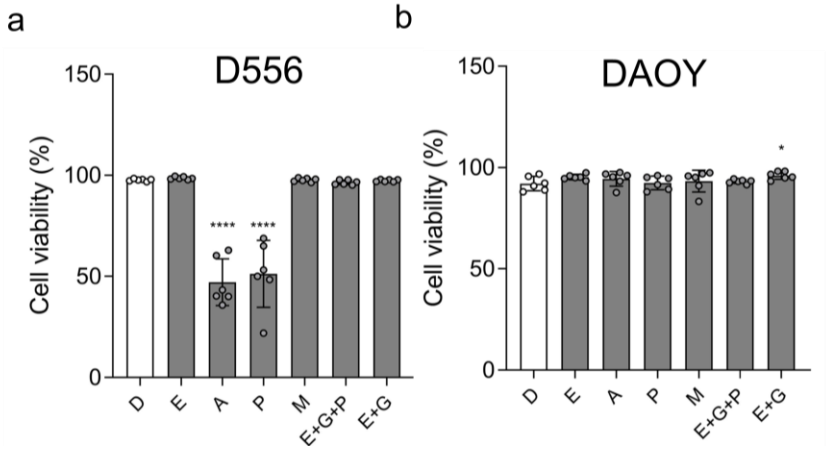

Figure S 2. A live/dead assay using calcein-AM/ethidium homodimer labeling of (a) D556 and (b) DAOY cells (D: DMEM added with 10% fetal bovine serum (FBS) and penicillin and streptomycin (PS), E: endothelial medium, A: astrocyte medium, P: pericyte medium, M: microglial medium, E + G: 1:1:1 mixture of endothelial medium, astrocyte medium, and microglia medium, E+ G + P: 1:1:1:1 mixture of endothelial medium, astrocyte medium, microglia medium, and pericyte medium) (Data represent mean ± s.d. of n = 5 for each condition, *p < 0.05 and ****p < 0.001 versus each cell culture medium by student t-test).

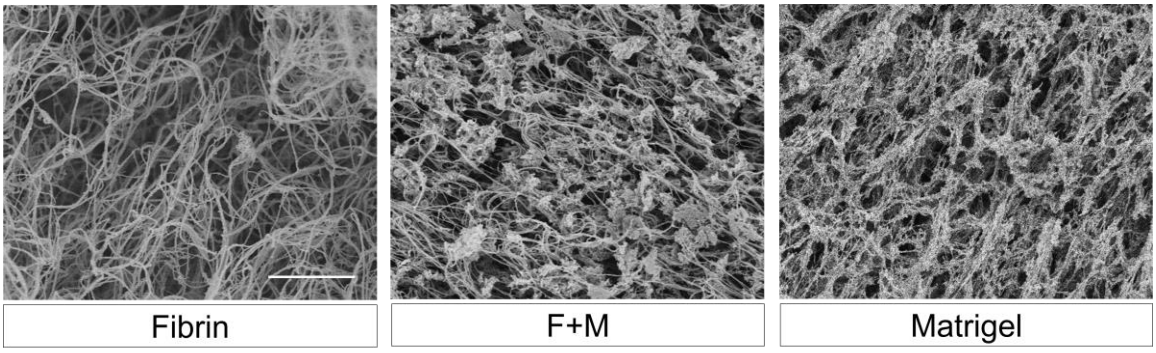

Figure S 3. SEM images of fibrin, F+M (1:1 mixture of fibrin and Matrigel), and Matrigel (Scale bar: 5 μm).

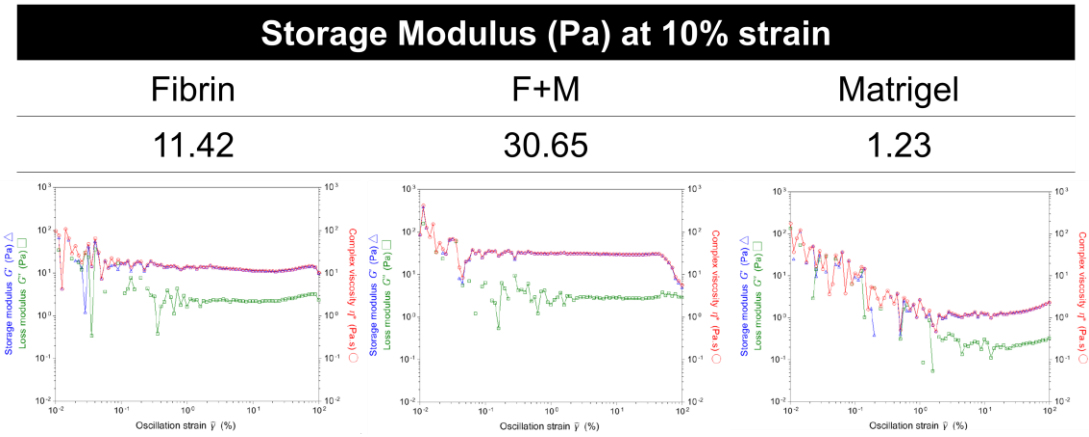

Figure S 4. The storage and loss modulus of fibrin, F+M (1:1 mixture of fibrin and Matrigel), and Matrigel respectively as a function of strain at the same temperature and oscillation frequency in gel rheology analysis, indicating critical strain for each plot.

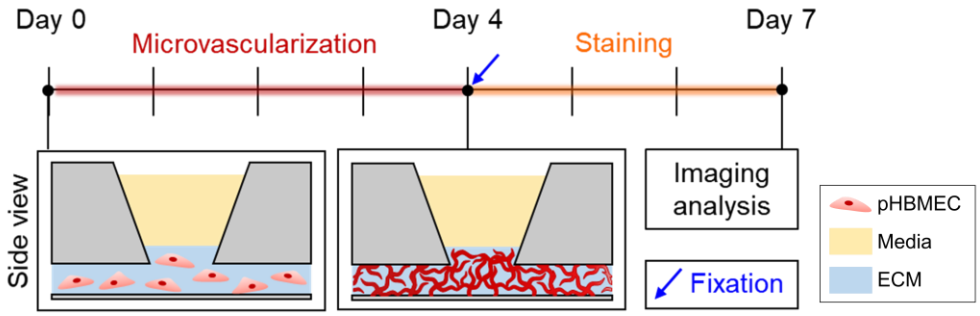

Figure S 5. Illustration of the experimental process to culture brain microvasculature

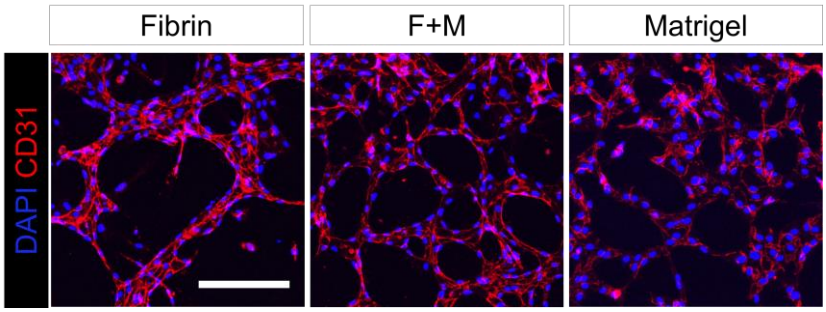

Figure S 6. Immunostaining of CD31 expression of microvasculature cultured in fibrin, F+M (1:1 mixture of fibrin and Matrigel), and Matrigel respectively, when endothelial medium was supplied to the microvasculature (CD31, red; DAPI, blue) (Scale bar: 200 μm).

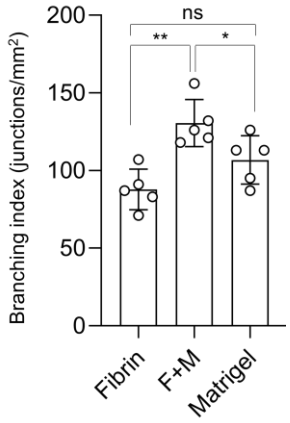

Figure S 7. Branching index extracted by quantifying the number of junctions of CD31 expressing microvascular network, when cultured in the endothelial medium (n = 5 for each condition, *p < 0.05, **p<0.01, and ***p<0.001 by student t-test. Data represent mean ± s.d.).

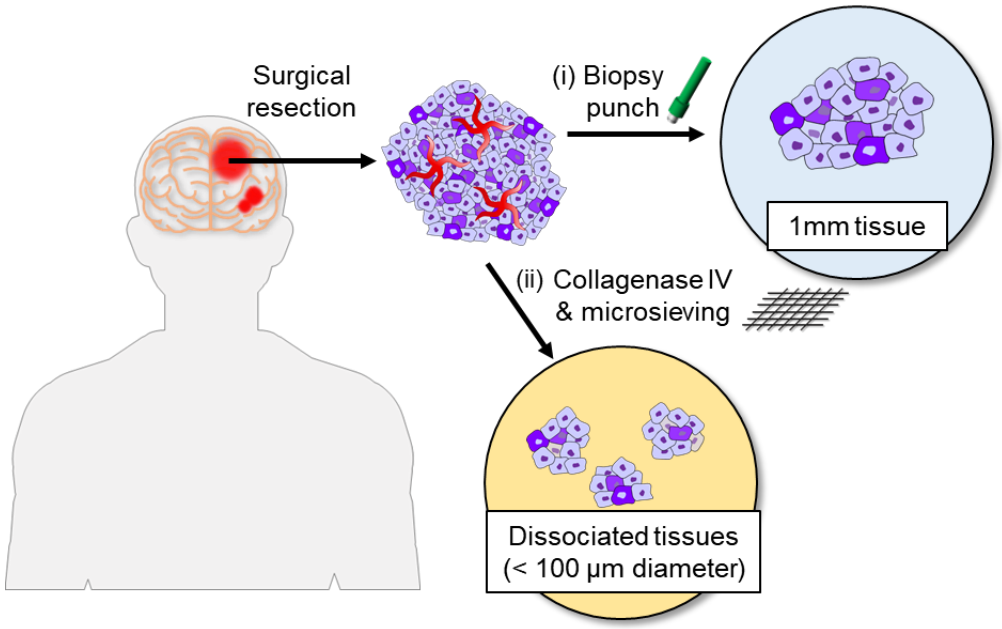

Figure S 8. Schematic description of the process to prepare for fresh patient samples retrieved through surgical resection. (i) Biopsy punch and (ii) collagenase IV digestion.

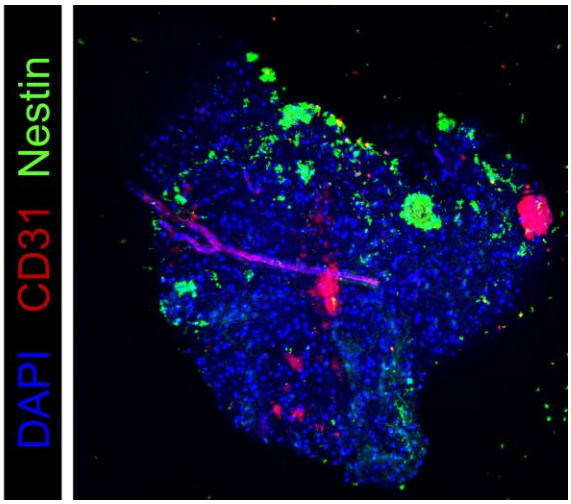

Figure S 9. Representative confocal images of DAPI (blue), CD31 (red), and nestin (green) of 1 mm JPA (juvenile pilocytic astrocytoma) patient tissue extracted through tissue biopsy (Scale bar: 400μm).

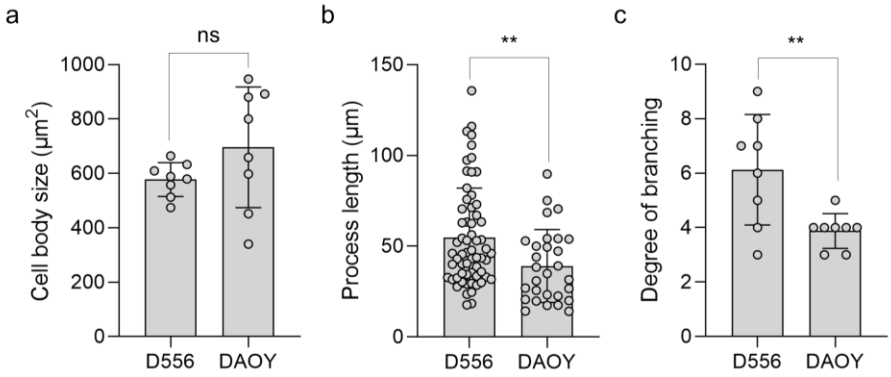

Figure S 10. Quantification of cell body size, process length, and degree of branching of D556 and DAOY cell line. (a) Cell body size of D556 and DAOY cell line cultured in F+M. (n = 8 for each condition, **p<0.01 and ***p<0.001 by student t-test. Data represent mean ± s.d.) (b) Process length of D556 and DAOY cell line cultured in F+M. (n = 14-63 for each condition, ***p<0.001 and ****p<0.0001 by student t-test. Data represent mean ± s.d.) (c) Degree of branching of D556 and DAOY cell line cultured in F+M. (n = 8 for each condition, *p < 0.05 , **p<0.01 ***p<0.001 and ****p<0.0001 by student t-test. Data represent mean ± s.d.)

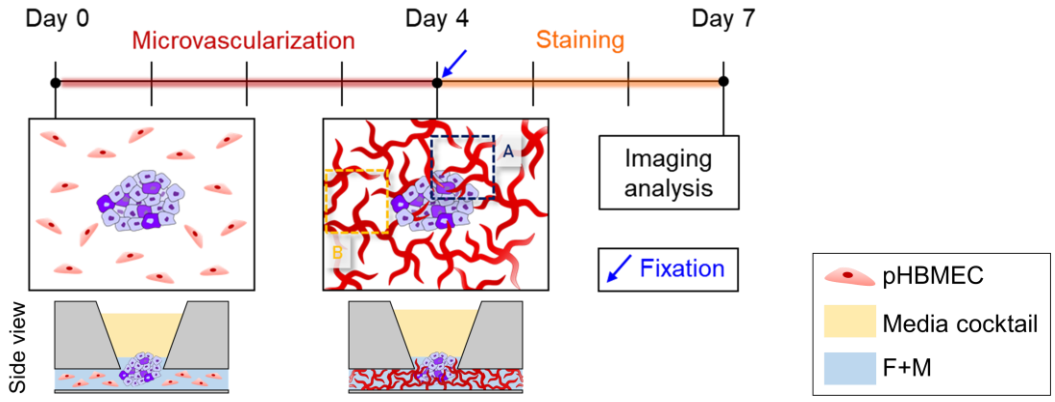

Figure S 11. Illustration of the experimental process to culture microvascularized pediatric brain tumor tissues (1 mm) in fibrin and Matrigel mixture with the adjusted media cocktail.

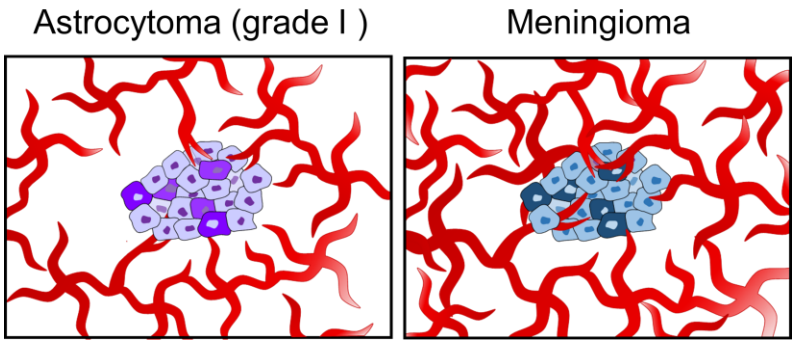

Figure S 12. Schematic description of microvascular density of the microvasculature cultured with astrocytoma and meningioma tissue, respectively.

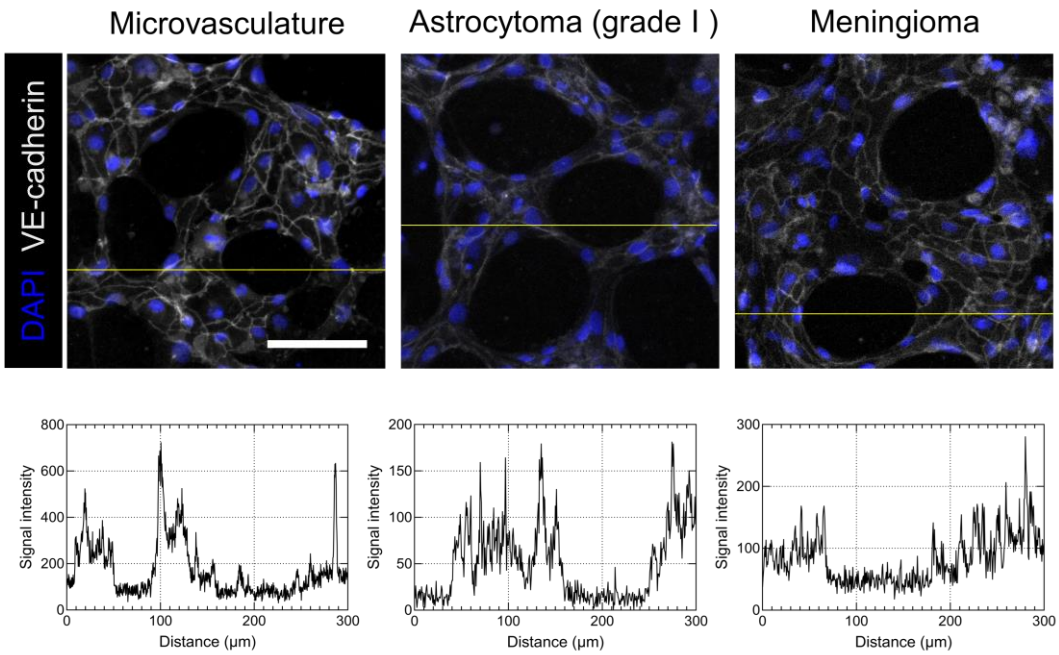

Figure S 13. Plot profile of signal intensity of VE-cadherin expression of each brain microvasculature on the yellow line in the representative confocal images of DAPI (blue) and VE-cadherin (gray) expressed on each brain microvasculature (Scale bar: 100 μm).

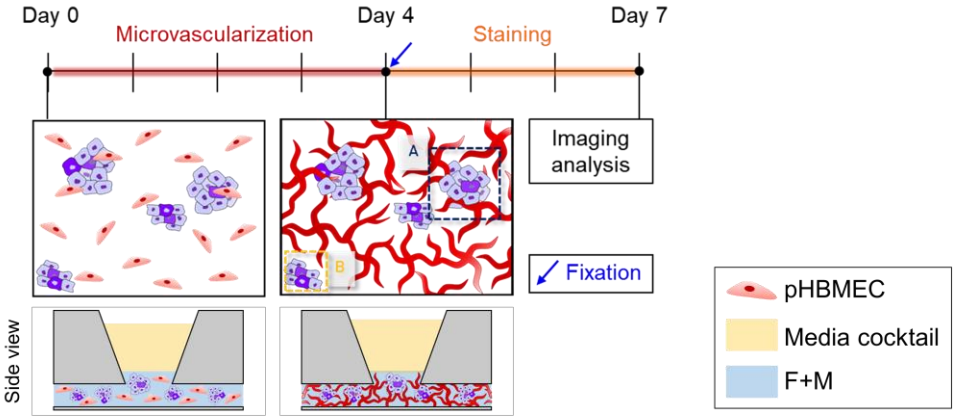

Figure S 14. Illustration of the experimental process to culture microvascularized patient astrocytoma tissues (<100 μm) in fibrin and Matrigel mixture with the adjusted media cocktail.

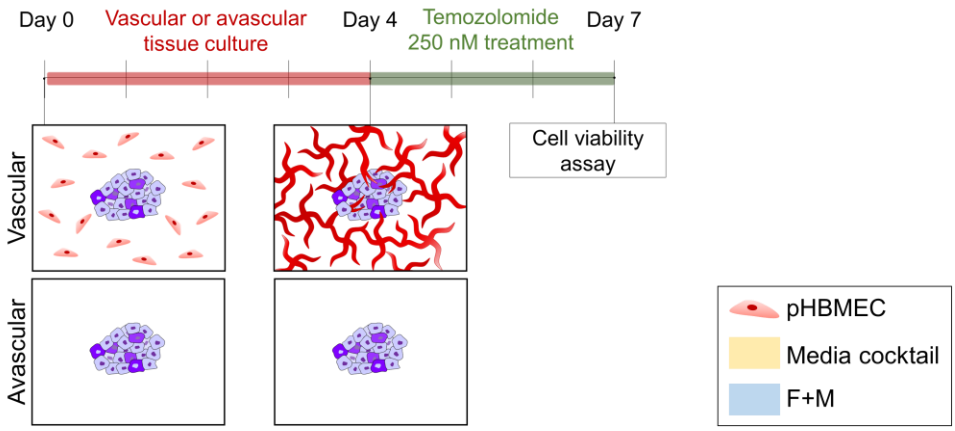

Figure S 15. Schematic description of experimental process to culture microvascularized patient astrocytoma tissues (1 mm) in fibrin and Matrigel mixture with the adjusted media cocktail, and investigate the response of the microvascularized tissues after temozolomide 250 nM treatment.

CHAPTER 3. BRAIN METASTASIS MODELLED IN A HUMAN CHOROID PLEXUS-ON-A-CHIP WITH *IN VIVO*-LIKE CEREBROSPINAL FLUID DYNAMICS AND FUNCTIONAL CAPILLARIES – EPITHELIUM COMPLEX

3.1 Introduction

The human brain choroid plexus (ChP) is a highly organized secretory tissue with a complex vascular system and epithelial layers in the ventricles of the brain [113, 114]. The ChP is the body's principal source of cerebrospinal fluid (CSF) and also functions as a barrier separating the blood from CSF, called the blood-CSF barrier (B-CSF-B) [115]. CSF plays a key role in providing buoyant physical protection for the brain as well as facilitating the development of the epithelia-endothelial convolute by circulating through the cerebral aqueduct [116, 117]. The movement of CSF through the body is pulsatile in nature which is driven primarily by the cardiac cycle [118-120]. Under this unique dynamic stimulation, the ChP exhibits a specialized structure wherein epithelial cells joined by tight junctions form an outer epithelial layer that surrounds fenestrated capillaries with low tight junction protein expression [113, 121]. Another feature of the ChP is that its vasculature is unlike that of the blood-brain barrier (BBB), where critical factors such as basement membrane laminins and other stromal cells including pericytes contribute to upregulated tight junctions [122-124]. A lack of disease models for this structure has made drug testing for the ChP very difficult. Drugs targeting human meningeal diseases have failed in animal models due to disparities between human and animal [45, 125, 126]. 2D cell culture of ChP demonstrates limited translation due to a lack of complexity and 3D tissue structure [48].

The location of the ChP, deep within the brain, as well as its specialized features have made studies of its physiology difficult. A further understanding of the central nervous system (CNS) barriers including the BBB and ChP system is essential for therapeutic development [127].

To address the limitations of conventional preclinical models, several *in vitro* models to recapitulate the complexity and specialized structure of the ChP have been developed. Recently, Pellegrini et al. developed a ChP organoid that recapitulated the B-CSF-B properties and functioned to successfully produce CSF [46]. Furthermore, they were able to reproduce an *in vivo*-like drug response in the ChP organoids similar to those from clinical trials. However, though the organoid model was able to recreate the critical characteristics of the ChP barrier, it lacked a vascular system and immune microenvironment which are crucial in its physiology. Moreover, the group did not recreate the *in vivo*-like CSF dynamic stimulation, which is a main component of ChP physiology. Another group reconstructed a neurovascular unit under the CSF effect using organ-on-a-chip technology, through which the group was able to successfully reconstruct the complex 3D structure [47]. This neurovascular-unit-on-a-chip represented BBB contact with brain parenchyma and CSF channels and was applied to stroke modeling and stem cell therapies testing. However, although this microfluidic model included a CSF channel, it was able to fully represent the ChP and CSF dynamics. Few *in vitro* models have been developed that can investigate the ChP physiology while under CSF flow dynamics, which is required for a better understanding of ChP physiology [48].

In this study, we developed a human ChP-on-a-chip as a model for leptomeningeal metastasis. This platform utilizes open microfluidic patterning to enable the simple

construction of a complex multilayer consisting of a ChP vascular network – epithelial layer. The extracellular matrix (ECM) was engineered using laminin to reconstitute the brain ECM, which exhibits enhanced tight junction expressions such as occludin and interactions with brain stromal cells including pericytes [15-17]. Also, the ChP reconstructed in this platform was subjected to dynamic flow physiologically reminiscent of *in vivo* CSF flow. The pulsatile CSF flow was reproduced using a rocking system, and the fluid dynamics was analyzed via image processing and computer simulation to recreate a flow as close as possible to human CSF dynamics. The analysis confirmed the unique oscillatory to and fro motion similar to that of the CSF with an *in vivo*-like flow rate and frequency. In our platform, we demonstrated high neurovasculature tight junction expression when the vessels co-cultured with pericytes in the engineered ECM, as expected of brain ECM. However, once dynamic CSF fluid flow was introduced to the system, the tight junction expression of the neurovasculature was significantly downregulated. Even though the vascular system was engineered to induce high tight junction expression, the addition of dynamic flow resulted in low tight junction expression of the neurovasculature which is characteristic of ChP capillaries. Moreover, epithelial cells lining the vasculature exhibited ciliogenesis as well as an increased cellular coverage area with an increased tight junction expression when subjected to recapitulated CSF flow. Enzymatic analysis of the established co-culture system exposed to dynamic flow was conducted, through which calcium and glucose levels were obtained that are indicative of CSF-like levels. To verify the capabilities of our human ChP-on-a-chip as a drug screening platform, we tested a typical intrathecal therapy used to treat metastasized breast cancer cells in the brain using this model [128-130]. Breast cancer cells are one of the most common tumors to

metastasize to the central nervous system, and the incidence of leptomeningeal metastasis (LM) occurring in breast cancer is reported to be approximately 5% [131]. Since tumor cells require an adequate blood supply to grow and develop a lesion after brain metastasis, they can often spread into ChP capillaries [132, 133]. This process and mechanism is still poorly understood due to a lack of valid *in vitro* ChP -mimetic models. Trastuzumab, an anti- human epidermal growth factor receptor 2 (HER2) targeting drug, is typically used to treat the disseminated breast cancer cells as a form of an intrathecal therapy [133, 134]. With our microfluidic chip with a reconstituted ChP under *in vivo*-like CSF flow, we presented physiologically relevant drug responses from breast cancer cells when affected by trastuzumab. Within our platform, we also recapitulated the motility and cytotoxic effects of macrophages, which are the most prevalent ChP immune cells. Our human ChP-on-a-chip with recapitulated CSF dynamics can serve as a powerful tool for better understanding of human ChP pathophysiology including the immune system and therapeutics development to treat cancers related to LM.

3.2 Results and Discussions

3.2.1 Human ChP model with in vivo-like physical traits

Our microengineered human ChP model reconstitutes a complex multilayer structure with ChP capillaries and epithelium, which enables drug testing and immune reaction analysis of breast cancer cells spread into the ChP system (Figure 12). An *in vivo*-like CSF dynamic flow and engineered brain-specific ECM was integrated to recapitulate ChP physiology (Figure 12).

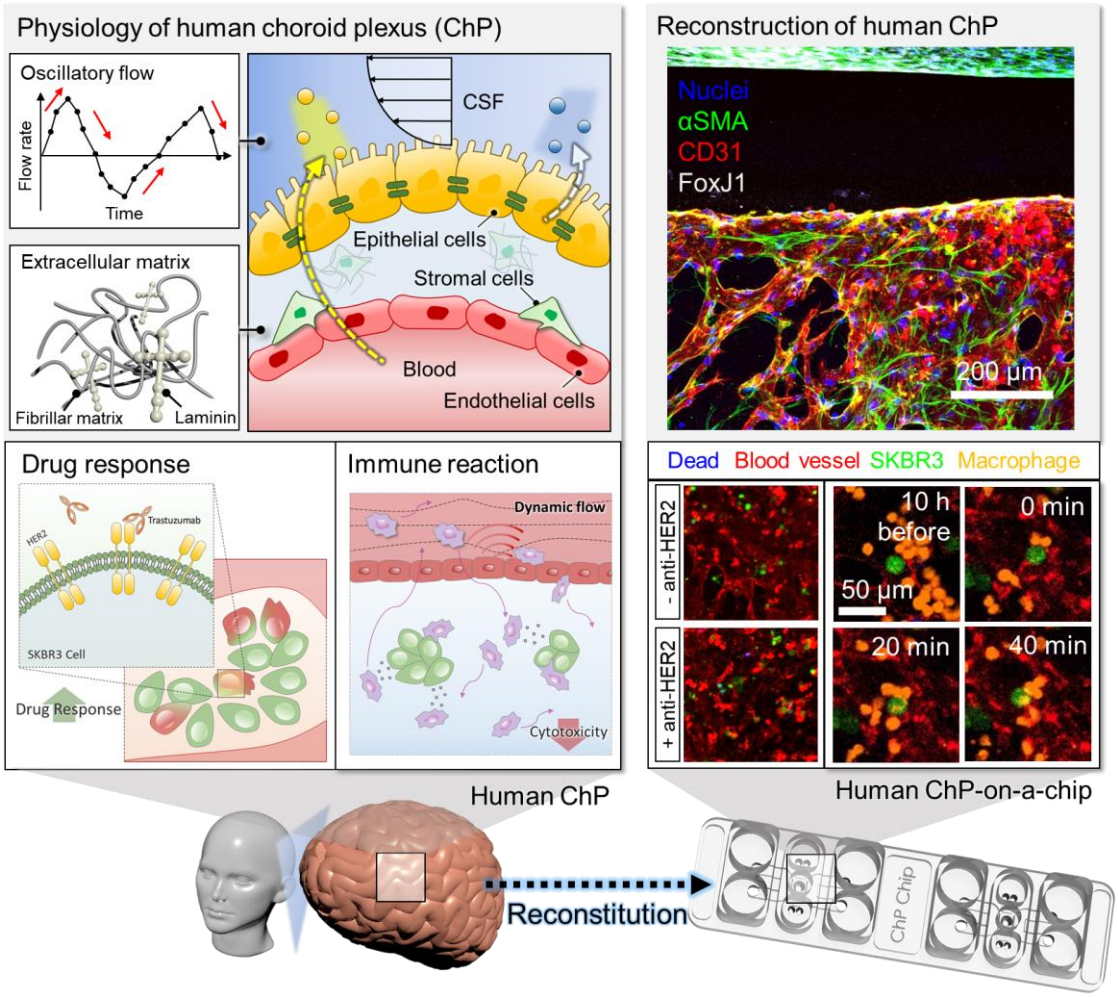

Figure 12. Engineered human choroid plexus (ChP)-on-a-chip to reconstitute ChP physiology under CSF flow. Schematic description of the 3D microfluidic chip to recapitulate the human ChP in the brain and tumor microenvironment in the ChP by engineering *in vivo*-like cerebrospinal fluid (CSF) flow dynamics and extracellular matrix (ECM).

The microfluidic platform consists of one central channel, two microchannels for gel loading, two side channels, and four media reservoirs (Figure 13a, b, Supporting information, Figure S16). The central channel of the platform mimics the ChP vascular system, and the microchannels for gel loading function as an ECM barrier to separate the capillaries and epithelial cell layer. Two flow channels provide routes to inject ChP epithelial cells for the formation of an epithelium layer, and the channels also function as

the pathway for *in vivo*-like CSF flow. The side channels serve as a lane for patterning cells such as endothelial cells to create a perfusable vascular network or macrophages for other assays. The sequence of microchannel patterning is indicated in Figure 13c.

The dimensions of the central channel and the geometry of the microposts were established by design rules meant to avoid hydrogel constriction, which can lead to bubble formation on the sides of the central channel (Supporting information, Figure S17). These design rules allowed successful micropatterning of multi-microchannels without any bubble traps. We confirm that our device with ChP-relevant architecture allowed the successful recapitulation of human *in vivo* ChP and its physiological features.

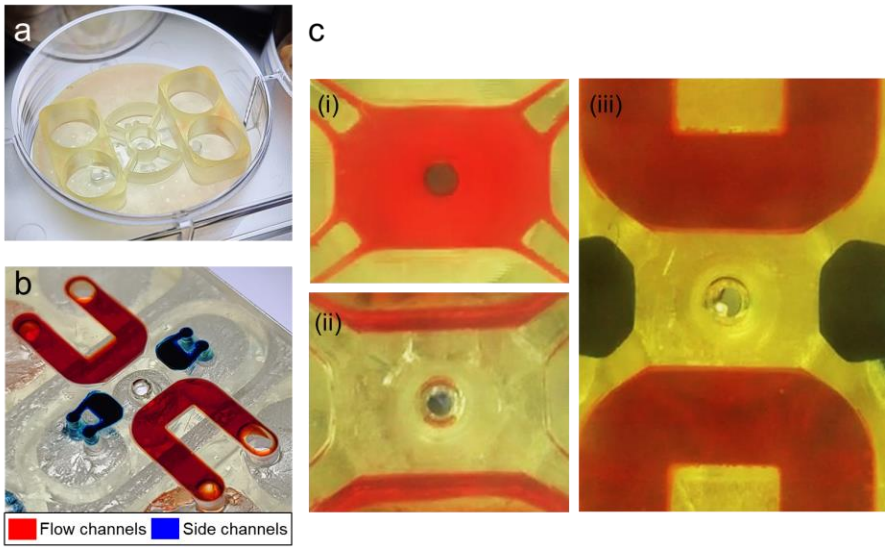

Figure 13. Engineered human choroid plexus (ChP)-on-a-chip. (a) Photograph of the 6-well plate formatted microfluidic platform to recreate the human ChP. (b) Photograph of the bottom of the human ChP-on-a-chip, where the flow channels and the side channels are patterned with red dye and blue dye, respectively. (c) Sequential steps for the microfluidic patterning; (i) Fill the central channel with a hydrogel mixed with the cell suspension by capillary-guided fluid patterning and wait for polymerization. (ii) Fill and withdraw a blank hydrogel through an injection hole of the flow channel to make the hydrogel remain only underneath the sides of the central channel as a blank ECM zone to separate the flow channels and central channels. And wait for polymerization. (iii) Fill the flow channels and the side channels with cell suspension or media.

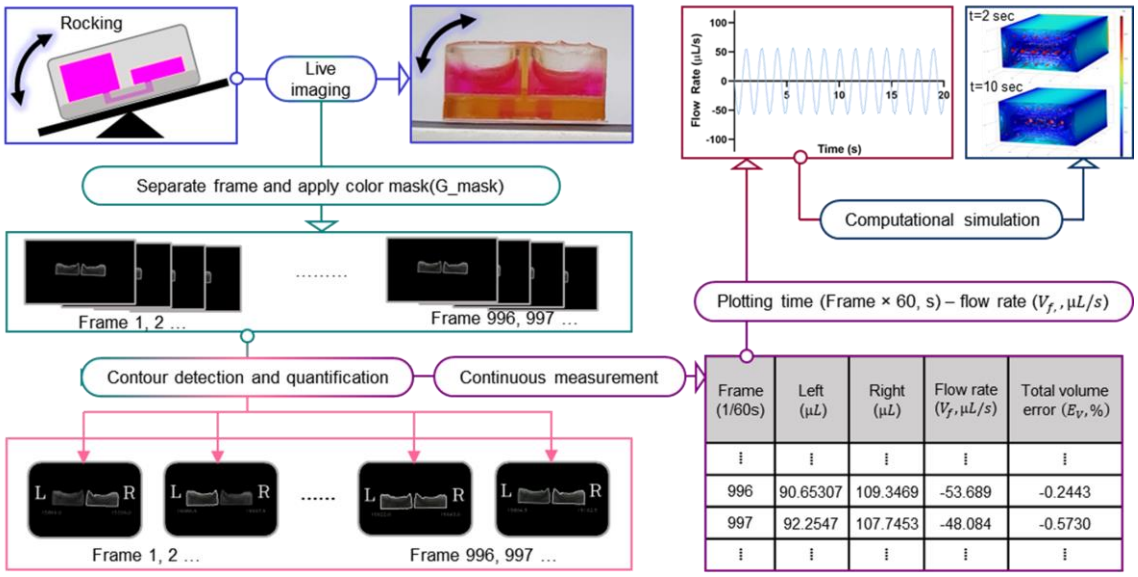

Figure 14. Fluid dynamics analysis via image processing to recapitulate CSF circulation in the microfluidic platform. Each reservoir of flow channels of in the human ChP-on-a-chip CSF flow area was filled with 150 μL media. The device was loaded on the rocking system and the rocking motion of the chip was recorded as a video clip. The video clip was separated into frames and the color masking was applied to each frame. The contour detecting process enabled the quantification of the altering volume of the media in each well. The quantification allowed for the continuous measurement of flow rates as time flows. The measured values are plotted into the time-flow rate graphs. The plots provide the values to conduct the computational simulation to investigate shear stress applied to the channels during the flow. The *in vivo*-like CSF dynamic can be selected by comparing the calculated values with the *in vivo* CSF flow parameters.

3.2.2 CSF fluid flow analysis

The pulsatile flow of the CSF in the ventricles of the brain is predominantly induced by cardiac motion [118-120]. The stroke volume of this distinctive CSF movement in the cerebral aqueduct ranged from 30 – 50 μL [135-138], where the volumetric value serves as a measure for flow since the net volume of fluid pulsating back and forth [139, 140]. Peak flow rate, frequency. Peak flow rate, another typical MRI-derived amplitude measure, ranged from 50 – 150 μL s^{-1} [141]. Another key value measured in CSF circulation is frequency, where the range varied from 0.008 Hz to the respiration rate which can be high

as 0.7 Hz [142, 143]. To measure the parameters of CSF flow, we developed a real-time flow measuring system where the dynamic flow within a microfluidic platform was analyzed using image processing technology (Figure 14). Our image processing system utilized color masking and contour detecting steps for real-time volume tracking while calculating total volume error for reliable data extraction. We extracted 30 time-flow rate plots where the frequency and tilting angle of the rocking system was varied (frequency: 0.1 – 0.85 Hz, angle: 5 – 15˚) (Figure 15). Among the flow rate graphs, the flow conditions of 0.7 Hz frequency and 5˚ tilting angle recreated dynamic flow values most similar to those of *in vivo* CSF flow. Using this rocking setup, the flow in the microfluidic device showed 26.4 μL of stroke volume, 57 μL s^{-1} of peak flow rate, and 0.67 Hz of frequency, which were within the range of normal human CSF flow information. Computational simulations of fluid dynamics within the microfluidic channel revealed how the shear stress was applied to the center channel (Supporting information, Figure S18). Our image processing system for analyzing dynamic fluid flow served as a strong tool to recapitulate *in vivo* CSF dynamics in the microfluidic platform.

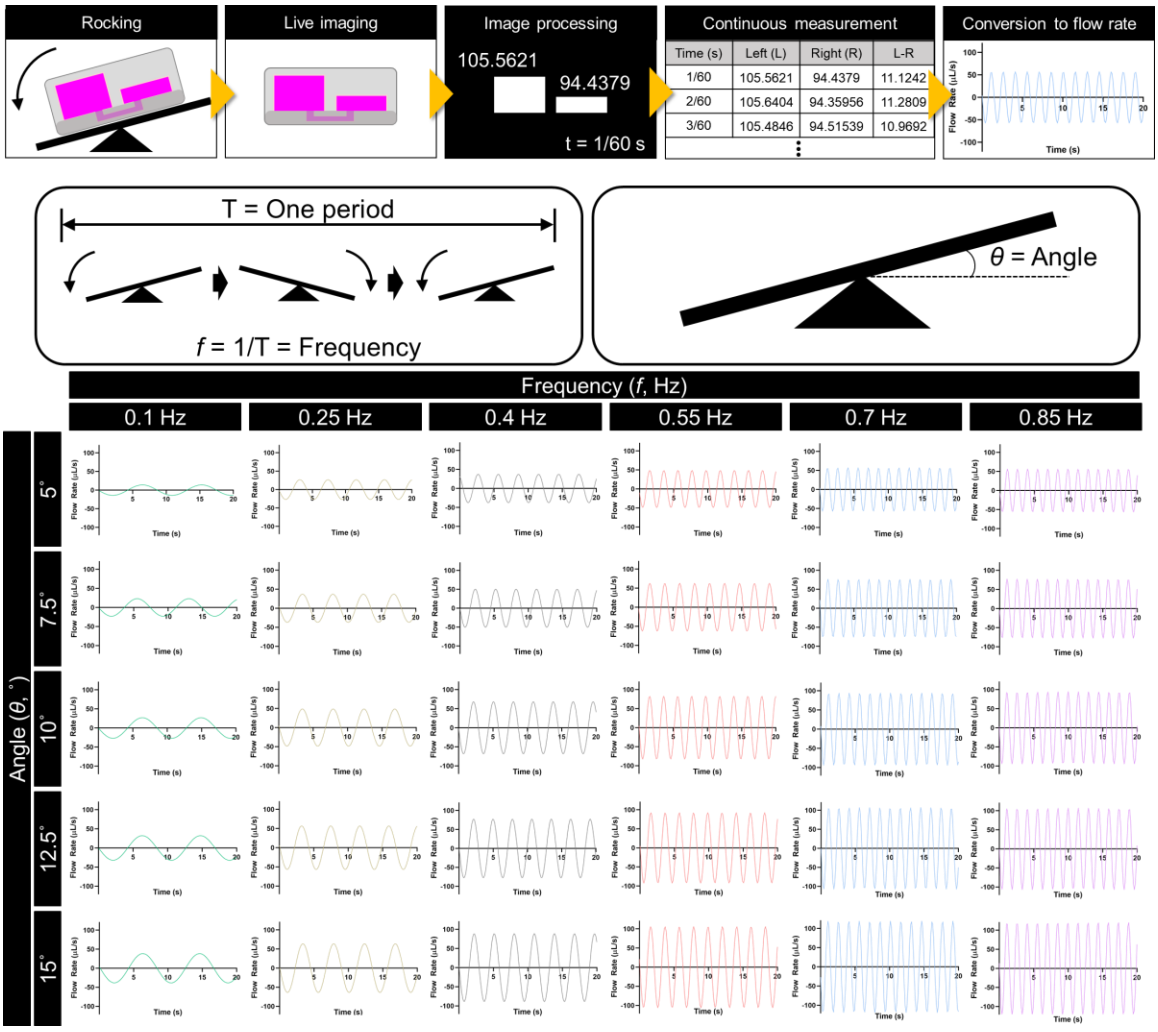

Figure 15. Flow rate analysis through image processing and time-flow rate plots of each flow condition.

3.2.3 Recapitulation of the ChP capillary system

ChP capillaries are highly vascularized and fenestrated in nature with low tight junction expression [113, 121, 144]. Other neurovascular units show high tight junction expression, which results from brain-specific ECM components including laminin and interaction with surrounding stromal cells such as pericytes. On the other hand, ChP capillaries exhibit low

tight junction expression even though they reside in a similar ECM and cellular microenvironment. Due to these factors, we hypothesized that the CSF's dynamic flow was the source of the unique characteristics of the ChP capillaries. Occludin, one of the typical tight junction proteins, was used to verify the different levels of tight junction expression when the microvascular network was modified with laminin and when it was subjected to dynamic *in vivo*-like flow (Figure 16a, b). RT-qPCR data of occludin quantification showed significantly upregulated occludin expression in vasculature cultured in the modified ECM without *in vivo*-like CSF flow, while the expression of occludin was significantly decreased in the adjusted ECM with *in vivo*-like CSF flow. Additionally, the microvascular density of the vascular network cultured in each condition was quantified.

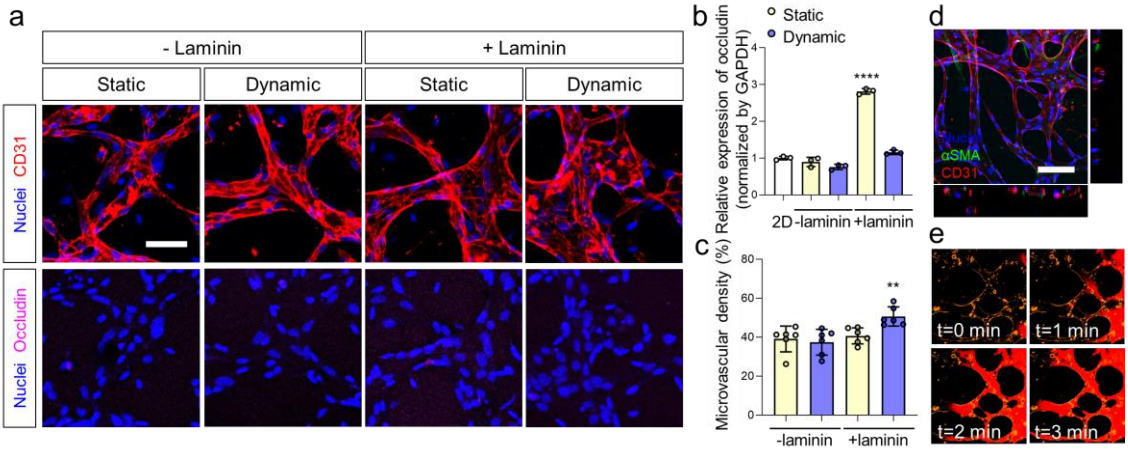

Figure 16. *In vivo*-like choroid plexus capillaries in the engineered microenvironment to reconstruct the human ChP. (a) Confocal images of immunostained nuclei (blue), CD31 (red), and occludin (magenta) expressed on the microvessels cultured in each condition. (scale bar: 50 μm) (b) RT-qPCR results of occludin expressed in 2D cultured HBMECs and HBVPs, and 3D cell cultured HBMECs and HBVPs in each cell culture condition (-laminin, +laminin, static, and dynamic). (c) Microvascular density of microvessels cultured in each culture condition. (d) Representative confocal image of nuclei (blue), αSMA (green), CD31 (red) expressed on the *in vivo*-like ChP capillaries. (scale bar: 100 μm) (e) Beads flow in the perfusable microvessels cultured in the engineered microenvironment (blood vessels, yellow; 0.2 μm microbeads, red).

The microvasculature cultured in the engineered ECM with dynamic flow exhibited the greatest microvascular density compared to microvessels cultured in other conditions. (Figure 16c) In addition, the microvasculature created in the engineered ECM showed a lumenized structure and perfusable network (Figure 16d, e). These results suggest that our microvasculature cultured in the brain-specific ECM with *in vivo*-like CSF dynamic flow is physiologically relevant to the ChP capillaries.

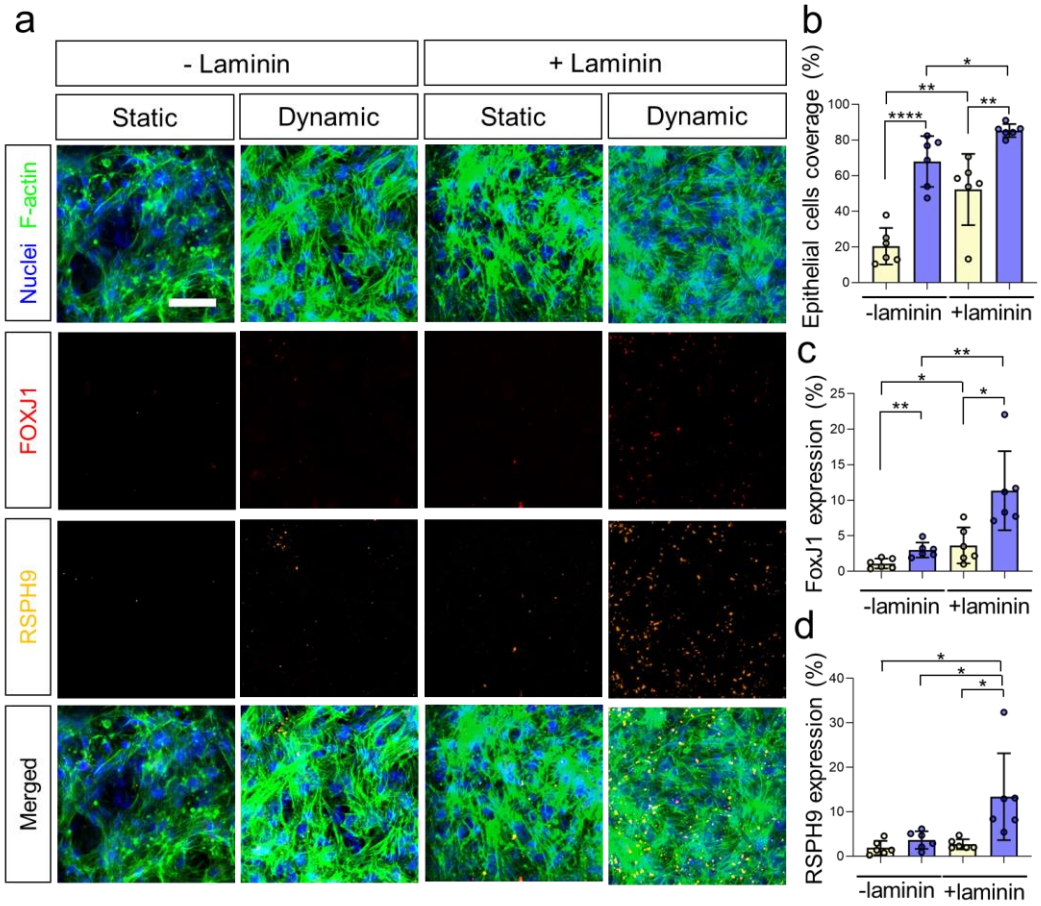

Figure 17. *In vivo*-like choroid plexus epithelium as a blood-CSF barrier (B-CSF-B) (a) Immunostaining of f-actin (green), FoxJ1 (red), RSPH9 (yellow) expressed on human choroid plexus epithelial cells (HCPEpiC) cultured in the ChP epithelium-on-a-chip in each culture condition. (scale bar: 50 μm) b-d Quantification of (b) the coverage of the HCPEpiC, (c) FoxJ1 expression density, and (d) RSPH9 expression density among the total epithelium area.

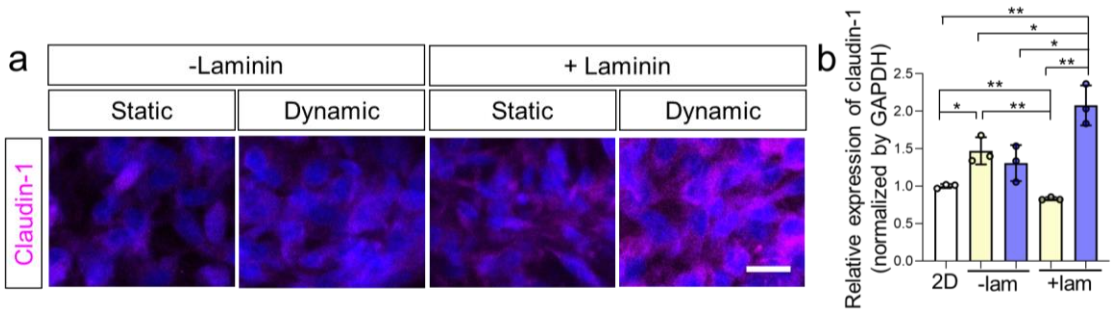

Figure 18. *In vivo*-like choroid plexus epithelium tight junction expression. (a) Confocal images and (b) qRT-PCR results of nuclei (blue) and claudin-1 (magenta) expressed on the epithelium by varying ECM and flow conditions. (lam: laminin) (scale bar: 20 μm)

3.2.4 Reconstruction of the ChP epithelium and its function

The ChP consists of a lining of epithelial tissue known as the B-CSF-B, which separates the CSF from the vascular system and regulates molecular exchange by complex architectural features including high tight junction expression [41, 145]. In particular, claudin-1 is one of the typical tight junction proteins that is highly expressed in the B-CSF-B [146-148]. This specialized epithelial barrier plays a critical role in the secretion of CSF, where the cilia built on the epithelium layer helps regulate CSF production [149, 150]. Cilia formation can be affected by the CSF dynamic flow and is indicated by several markers including FoxJ1 and RSPH9 [116, 151]. This fluidic production is related to the epithelial regulation of transporting ions and water between the blood and the ventricles, which indicates the process is associated with capillaries-epithelium complex [152]. Through this procedure, CSF is generated with distinctive molecular components such as lower calcium and glucose levels relative to the plasma is generated[153]. We presented the characteristics of the ChP epithelial layers and recreated their function in our microengineered ChP culture condition. To determine the response of the epithelial layers

in each culture condition, we developed the ChP epithelium-on-a-chip, which reconstructs the flow channels and reservoirs of the human ChP-on-a-chip while allowing culture of the ChP epithelium in a horizontal direction (Supporting information, Figure S19). The epithelial cells in the ChP epithelium-on-a-chip were subjected to the same fluid dynamic conditions as the ones in the human ChP epithelium-on-a-chip according to the computational simulation (Supporting information, Figure S18). The ChP epithelium-on-a-chip allowed for the horizontal patterning of the epithelial cells through gel patterning below the flow channels, which was enabled by the local plasma treatment method established for this chip development. When the HCPEpiCs patterned on the gel layers were cultured in the device for 48h in each condition, the condition with adjusted ECM under *in vivo*-like CSF flow exhibited the highest coverage and ciliogenesis markers, FoxJ1 and RSPH9 (Figure 17). Moreover, this same condition showed the highest claudin-1 expression compared to others in different microenvironments (Figure 18a, b). To examine whether the ChP capillaries-epithelium complex functioned as the CSF source under dynamic flow, we conducted enzymatic assays to measure the concentration of calcium and glucose released to the serum-free media extracted from the microfluidic chip when exposed to each flow condition. When the tissue was cultured in dynamic conditions, the calcium and glucose levels were significantly lower than the ones from the static condition, which had a lower concentration of calcium and glucose in CSF than the other biofluid, plasma (Figure 19). We concluded that the ChP epithelium as well as the ChP capillaries were recapitulated in the engineered ECM under *in vivo*-like CSF dynamic flow, where the released molecules in the ChP capillaries-epithelium complex cultured in the microengineered condition presented physiologically relevant levels with CSF.

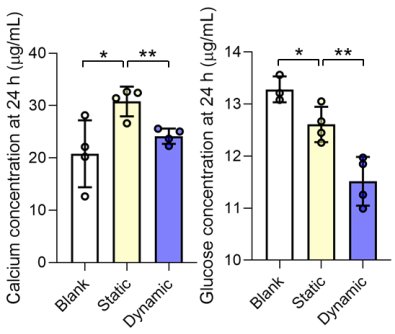

Figure 19. Quantification of calcium (left) and glucose (right) concentrations in the serum-free media extracted in static and dynamic culture conditions, respectively.

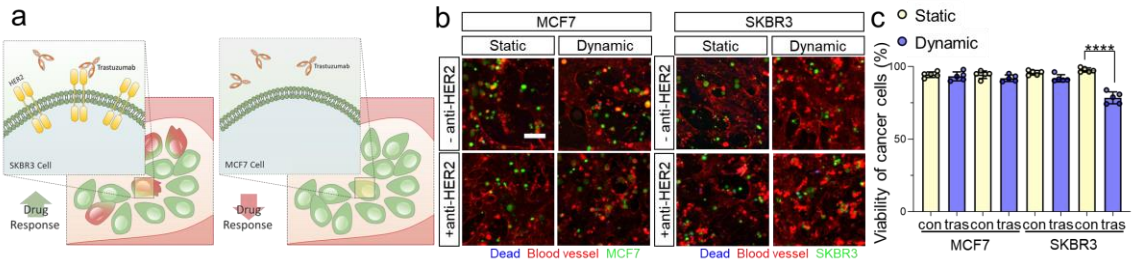

Figure 20. Drug responses to the intrathecal therapy in the human ChP-on-a-chip. (a) Illustration of physiologically relevant drug response of each breast cancer cell line, SKBR3 and MCF7, when applied to an anti-HER2 drug, trastuzumab. b, c (b) Confocal images and (c) quantification of the viability of MCF7 and SKBR3 cells (green), respectively, when applied to trastuzumab in each flow condition. (con: control, tras: trastuzumab) (blood vessels, red; dead signals, blue) (scale bar: 50 μm)

3.2.5 Drug response and immune reaction in ChP tumor microenvironment

Breast cancer, lung cancer, and melanoma are the most common cancers to spread to the leptomeninges, where 12 – 35% of breast cancer causes the solid tumor-related LM [154, 155]. In particular, human epidermal growth factor receptor 2 (HER2)-positive breast cancer cells are more likely to progress brain metastasis [156, 157]. This process is linked to the cancer cells spread in the ChP, since cancer cells pass through the ChP to infiltrate

the CSF where the metastatic cells may circulate freely and lead to LM [7]. One of the typical therapeutic methods to treat breast cancer cells metastasized to the brain is an anti-HER2 drug called trastuzumab, which is intrathecally administered to target HER2-positive breast cancer cells disseminated in the brain [128, 158, 159]. Though this type of tumor metastasis into the ChP is relatively rare compared to other methods of brain metastases, a better understanding of the pathophysiology is required for its treatment. To obtain a better understanding of oncology, anti-cancer drug response as well as tumor-immune reaction should be unveiled. To verify the utility of the human ChP-on-a-chip as a drug testing and immuno-oncology screening platform, we reconstructed a breast cancer invasion into the ChP, where intrathecal therapy was tested on the brain metastasis treatment and macrophages in the ChP were applied to investigate the tumor-immune reaction.

Two groups of the ChP model for the dispersed breast cancer were constructed to compare the responses to trastuzumab treatment: the HER2-negative cell line, MCF7, and the HER2-overexpressing cell line, SKBR3. We expected that the cytotoxic effect would be higher in SKBR3 than MCF7 when the ChP with breast cancer cells were treated with trastuzumab (Figure 20a). The trastuzumab was delivered through the flow channels, which mimicked the intrathecal therapeutic method to inject the drug via the CSF. When the anti-HER2 drug was applied to each breast cancer-spread ChP model under *in vivo*-like CSF flow, the cell death rate was significantly upregulated when SKBR3 cells were exposed to the anti-HER2 drug whereas MCF7 cells showed no significant change in viability under the drug treatment (Figure 20b, c). On the other hand, no significant change in cytotoxic

effect in both MCF7 and SKBR3 cells was shown when trastuzumab was applied to the models under static conditions (Figure 20c).

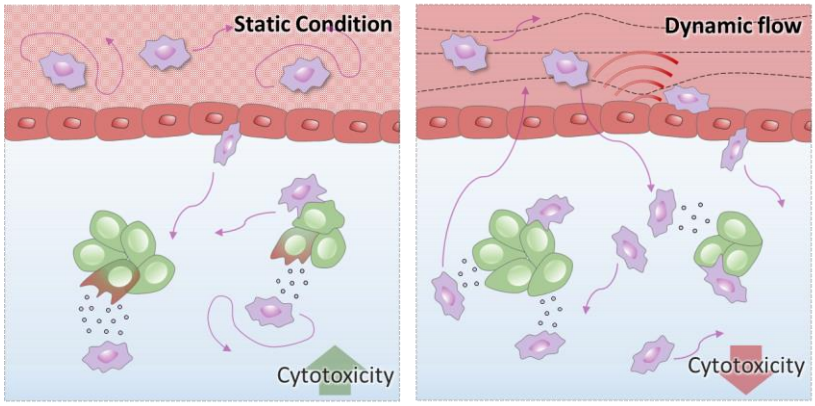

Figure 21. Schematic description of tumor-immune reaction and motility of macrophages under each flow condition.

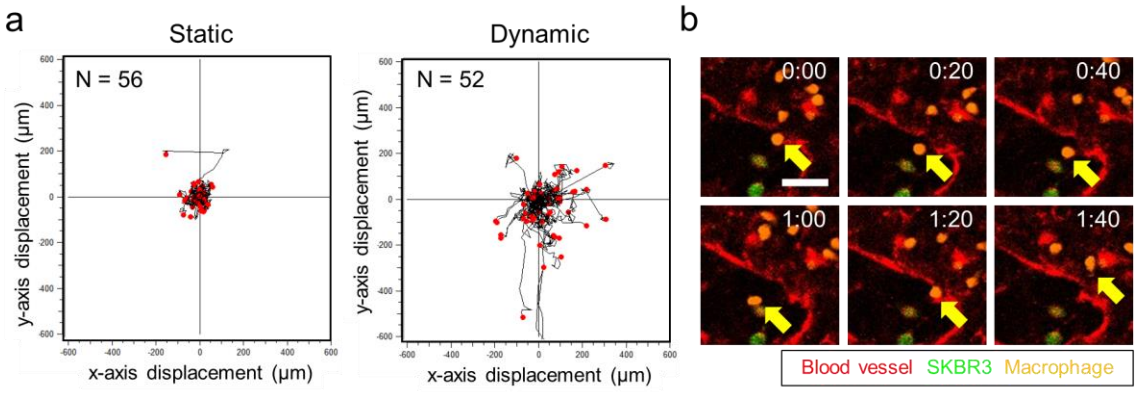

Figure 22. Motility of macrophages by the immune reaction with breast cancer cells in the human ChP-on-a-chip. (a) Trajectory plot of the macrophage migration under static and dynamic conditions, respectively. (b) Confocal images of intra and extravasating macrophages under dynamic flow in the human ChP-on-a-chip. The yellow arrow indicates the intra and extravasating macrophage. (scale bar: 50 μm)

Immunosuppressive molecules are highly expressed on the surface of circulating tumor cells (CTCs) [160]. In particular, CD47, sometimes referred to as a “don’t eat me” signal, allows tumor cells to escape immune surveillance and avoid phagocytosis by macrophages [161]. In our ChP model, CD47 expression levels were possibly upregulated in tumor cells due to fluid shear stress, which could explain why the percentage of macrophage-mediated killing of tumor cells was much less when dynamic CSF flow was applied (Figure 21, 23a, b). Adhesion molecules in human endothelial cells that are involved in transmigration could also be selectively regulated by a physiologically relevant range of biomechanical forces [162, 163], and this could lead to higher chances of monocyte/macrophage transendothelial migration and infiltration in our model (Figure 21, 22).

Tumor-associated macrophages (TAMs) are generally described as M2-like macrophages and play a significant role in tumor progression and invasion. The molecular profile of breast cancer cell lines shows that TAMs with high levels of CD163 are mostly observed in HER2-positive and basal-like breast cancer [164]. Although the relationship between HER2-enriched status in breast cancer and macrophage polarization remains unclear, SKBR3 cells produce major cytokines such as colony-stimulating factor-1 (CSF-1) that promote macrophage polarization toward the M2 phenotype [165, 166]. M2-like TAMs are highly correlated with poor prognosis of breast cancer because they can induce tumor cell growth, invasion, and metastasis [167]. In this model, we observed the distinctive antitumor activity of polarized macrophages under the dynamic flow condition, where macrophages often failed to eliminate tumor cells in close contact (Figure 23). Whether those macrophages that interacted with tumor cells resembled TAMs needs further discussion with subsequent analysis of protein expression levels. As an emerging

therapeutic strategy for breast cancer, a HER2-targeted monoclonal antibody in combination with a blockade of CD47 enhances antibody-mediated phagocytosis, and inhibits M2 macrophage recruitment with a CSF-1R targeting agent [168]. This implies that there is a close relationship between HER2-enriched cells or breast cancer stages and TAMs, but this has not been fully elucidated yet.

In summary, we recapitulated the physiological relevance of the unique immune system of the ChP, in which macrophages are the largest population during infection and cancer progression. The ChP model with dynamic CSF flow closely mimics macrophage-mediated antitumor activity against HER2-enriched breast cancer cells and the possible conversion of resident macrophages into TAMs. This platform offers a more *in vivo*-like environment to understand immune-tumor cell interactions in the TME and represent human drug responses.

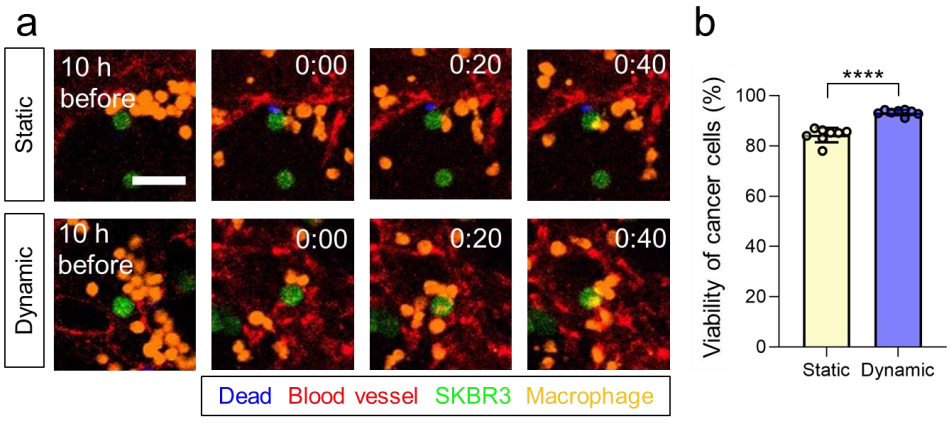

Figure 23. Cytotoxic effects of macrophages derived by immune reaction with breast cancer cells in the human ChP-on-a-chip. (a) Confocal images and (b) quantification of macrophage – breast cancer cytotoxic response in static and dynamic condition, respectively. (scale bar: 50 μm)

3.3 Conclusions

In this research, we developed a human ChP-on-a-chip, which recapitulates the human capillaries-epithelium complex in the ChP system through the following processes. The physical design of the microfluidic device allowed for the construction of a multi-layered capillaries – epithelium complex of the ChP, and the engineered ECM with brain-specific components recreated a more accurate brain microenvironment. Furthermore, *in vivo*-like CSF flow was recreated using dynamic fluid flow and was applied to the microfluidic platform to recapitulate the ChP dynamic microenvironment. After successfully recapitulating the human ChP, breast cancer cells were spread in the ChP and drug targeting the cancer cells were tested. Moreover, the immune reaction between macrophages and the breast cancer cells in the ChP was reconstituted and investigated using the platform. In conclusion, this human ChP model to recapitulate the human brain microenvironment can provide a powerful tool in which the pathophysiology and drug response can be reliably studied.

3.4 Materials and Methods

Device design and fabrication. In this study, we designed our prototype using SolidWorks (Dassault Systèmes), a solid modeling computer-aided design (CAD) software. The device was then fabricated using a commercially available high-resolution DLP 3D printer (Figure 4, 3D Systems). The resin used MED-AMB 10 (3D Systems), a rigid bio-compatible resin capable of meeting ISO 10993-5 and -10 standards for biocompatibility (cytotoxicity, sensitization and irritation. The fabricated device was

rinsed with isopropanol for 10 min and cured in a UV chamber for 60 min. Single-sided PSA (Pressure Sensitive Adhesive) film (IS-00820, IS Solution, Korea) was bonded to the bottom of the device as PSA film is biocompatible and transparent similar to glass.

Cell preparation Primary human brain microvascular endothelial cells (HBMEC; Cell systems; # ACBRI 376) at passage 4–5 were maintained in endothelial cell medium (Sciencell; #1001) on flasks coated with 50 $\mu g mL^{-1}$ fibronectin (Sigma-Aldrich). Human brain vascular pericytes (HBVP; Sciencell; #1200) were cultured on 1 mg mL^{-1} poly-L-lysine (PLL, Sigma-Aldrich) coated flasks and maintained in pericyte medium (Sciencell; #1201) and the cells between passages 3 and 4 were used for all expreiments. Human choroid plexus epithelial cells (HCPEpiC; Sciencell; #1310) at passage 3 were maintained in epithelial cell medium (Sciencell; #4101) on flasks coated with 1 mg mL^{-1} poly-L-lysine (PLL, Sigma-Aldrich). Fibronectin and PLL coating procedures were achieved following the manufacturer's instruction. The cells were maintained in an incubator at 37 °C in 5% CO_2 for 3 days. SKBR3 and MCF7 cells were obtained from Korean cell line bank (KCLB, Korea). and cultured in Dulbecco's Modified Eagle's Medium (DMEM) including 10% fetal bovine serum (HyClone, USA) and 1% penicillin–streptomycin (Gibco, USA). A human leukemia monocytic cell line, THP-1 cells were cultured in Roswell Park Memorial Institute Medium-1640 (RPMI-1640) supplemented with 10% fetal bovine serum, 1% penicillin-streptomycin, and 0.05 nM 2-Mercaptoethanol. The culture medium was changed every 2-3 days, and the cells were resuspended at a density of 0.3×10^6 cells mL^{-1} for every media change. THP-1 cells were then seeded in 6-well plates at a density of 1×10^6 cells/well and treated with 100 nM phorbol 12-myristate 13-acetate (PMA). After 48 h, only adherent cells were collected using 0.25% Trypsin-EDTA to be used for the tumor

cell killing assay.

Construction of the human ChP chip system. Prior to filling the microchannels, the 3D printed chips were irradiated with oxygen plasma using a plasma treatment system (Femto Science, Korea) at 70 W for 1 min to convert the hydrophobic surface to hydrophilic. 50 μL mixture of suspension with 8×10^6 cells mL^{-1} of HBMECs and HBVPs (HBMECs : HBVPs = 4:1, volume ratio), bovine fibrinogen solution (Sigma, USA; 2.5 mg mL^{-1}), and laminin from human placenta (Sigma, USA; 0.1 mg mL^{-1}) with 1 μL of bovine thrombin (Sigma, USA; 1 U mL^{-1}) was prepared. The 1.8 μL of mixture was introduced into each central microchannel by injecting it through the central hole. After allowing 10 min for the patterned mixture to cross-link at room temperature, the ECM with high concentration bovine fibrinogen solution (10 mg mL^{-1}) was introduced in the flow channels through the holes and aspirated to make the solution remain in the lower channels right next to the central channel, where the fibrin gel serves as a barrier between capillaries and epithelium. The endothelial cell medium supplemented with vascular endothelial growth factor (VEGF; Peprotech; 50 ng mL^{-1}), fibroblast growth factor (FGF; Gibco; 20 ng mL^{-1}), epidermal growth factor (EGF; Peprotech; 20 ng mL^{-1}) was prepared, and 200 μL of the medium was loaded in reservoirs after 10 min for cross-linking at room temperature. The endothelial cells were patterned to form perfusable blood vessels by injecting 10 μL suspension with 5×10^6 cells mL^{-1} HBMECs and HBVPs (HBMECs:HBVPs = 4:1, volume ratio) in the side channels and tilting the device by 90 degrees for 30 min in an incubator at 37 °C in 5% CO_2 to allow the cells to adhere on the gel surface in the central channels. After 6 days culturing the HBMECs and HBVPs in an incubator at 37 °C in 5% CO_2, 20 μL suspension with 5×10^6 cells mL^{-1} HCPEpiCs was loaded in each flow channel

and the chip was tilted by 90 degrees for 30min in an incubator at 37 °C in 5% CO_2 to allow the cells to adhere on the gel surface in the lower channels of the flow channels to construct the ChP epithelium. The cocktail medium was daily changed. After 24 h to stabilize the epithelium, each reservoir of the flow channels was filled with 150 μL of the serum-free medium and the *in vivo*-like CSF flow was applied to the microfluidic chip by loading the platform on the rocker and culturing the system for 24 h in the incubator.

Construction of the ChP epithelium-on-a-chip system. Prior to filling the microchannels, the adhesive films were irradiated with oxygen plasma using a plasma treatment system (Femto Science, Korea) at 70 W for 20 s to convert the hydrophobic surface to hydrophilic, and were adhered to the 3D printed chips. 50 μL mixture of bovine fibrinogen solution (Sigma, USA; 2.5 mg mL^{-1}), and laminin from human placenta (Sigma, USA; 0.1 mg mL^{-1}) with 1 μL of bovine thrombin (Sigma, USA; 1 U mL^{-1}) was prepared. The 15 μL of mixture was introduced into the bottom microchannels through the injection holes. After allowing 10 min for the patterned mixture to cross-link at room temperature, 20 μL suspension with 5×10^6 cells mL^{-1} HCPEpiCs was loaded in each top channel and the chip was filled with the media after 30min in an incubator at 37 °C in 5% CO_2 to allow the cells to adhere on the gel surface in the bottom channels to construct the ChP epithelium. The medium was daily changed. After 24 h to stabilize the epithelium, each reservoir was filled with 150 μL of the serum-free medium and the *in vivo*-like CSF flow was applied to the microfluidic chip by loading the platform on the rocker and culturing the system for 24 h in an incubator at 37 °C in 5% CO_2.

Construction of the tumor microenvironment in human ChP chip system. Prior to filling the microchannels, the 3D printed chips were irradiated with oxygen plasma using

a plasma treatment system (Femto Science, Korea) at 70 W for 1 min to convert the hydrophobic surface to hydrophilic. Prior to loading cells in the microfluidic chip, SKBR3 and MCF7 cells were labeled with CellTraceTM CFSE (1:1000; Invitrogen, USA). 50 μL mixture of suspension with 8×10^6 cells mL^{-1} of HBMECs, HBVPs, cancer cells (HBMECs:HBVPs:cancer cells = 8:2:1 volume ratio), bovine fibrinogen solution (Sigma, USA; 2.5 mg mL^{-1}), and laminin from human placenta (Sigma, USA; 0.1 mg mL^{-1}) with 1 μL of bovine thrombin (Sigma, USA; 1 U mL^{-1}) was prepared. The 1.8 μL of mixture was introduced into each central microchannel by injecting it through the central hole. After allowing 10 min for the patterned mixture to cross-link at room temperature, the ECM with high concentration bovine fibrinogen solution (10 mg mL^{-1}) was introduced in the flow channels through the holes and aspirated to make the solution remain in the lower channels right next to the central channel, where the fibrin gel serves as a barrier between capillaries and epithelium. 200 μL of the medium was loaded in reservoirs after 10 min for cross-linking at room temperature. The endothelial cells were patterned to form perfusable blood vessels by injecting 10 μL suspension with 5×10^6 cells mL^{-1} HBMECs and HBVPs (HBMECs:HBVPs = 4:1, volume ratio) in the side channels and tilting the device by 90 degrees for 30 min in an incubator at 37 °C in 5% CO_2 to allow the cells to adhere on the gel surface in the central channels. After 4 days culturing the cells in an incubator at 37 °C in 5% CO_2, 20 μL suspension with 5×10^6 cells mL^{-1} HCPEpiCs was loaded in each flow channel and the chip was tilted by 90 degrees for 30min in an incubator at 37 °C in 5% CO_2 to allow the cells to adhere on the gel surface in the lower channels of the flow channels to construct the ChP epithelium. After 24 h to stabilize the epithelium, each reservoir of the flow channels was filled with 150 μL of the serum-free medium and the *in*

vivo-like CSF flow was applied to the microfluidic chip by loading the platform on the rocker and culturing the system for 24 h in an incubator at 37 °C in 5% CO_2.

Image processing. An image pre-processing and an analyzing algorithm was developed by Python (3.7.0) and the OpenCV library. The live video taking the rocking motion of the microfluidic platform was captured in 60 frame rate camera and each video was taken for 20 – 25 secs. Around 1200 – 1500 images were obtained from the video. The platform was filled with magenta-colored media (DMEM) for enabling the identification and segregation of media in the images to create the mask. A color mask (HSV threshold (56,52,0)) was implemented as image pre-processing filter for all frames. Only the area of media filled in the two media reservoirs filtered by the mask was isolated from images. To distinguish and measure the media area, we developed the image analysis algorithm for real-time volume tracking and OpenCV-based contour detecting. The integrative system developed by Python was conjugated to detect and quantify media area. Continuous measurements from whole frames were converted into flow rate by calculating the difference in area between two reservoirs and total volume error for verifying that the measurements were reliable. Finally, we plotted a time-flow rate graph for each condition.

Computational fluid dynamics. COMSOL software (COMSOL Multiphysics 5.5) was used to evaluate the channel wall and interior shear stress under a varying flowrate condition. A rectangular channel was modeled with dimension of 2.3 mm length × 1 mm width × 2 mm height and a fluid using the properties of water was flowed inside the inlet. The simulation estimated the velocity fields U inside the mesh solving the Navier-Stokes equation with continuity assuming no-slip boundary conditions in stationary mode. Finally, the shear stress was obtained considering the shear rate calculated as dU/dz multiplied by

the dynamic viscosity of the fluid μ.The flowrate data was imported in COMSOL from a spreadsheet using a piecewise cubic interpolation. The varying flowrate condition was fixed at the inlet and the other port was set as an open boundary without any normal stress. We used the laminar flow considering the Reynolds number calculated to be inferior to 100 as a reasonable assumption. Other assumptions considered are a Newtonian behavior of the fluid in this case water dynamic viscosity and the presence of gravity.

Real-time qRT-PCR. The samples were treated with TRIzol reagent (Invitrogen, USA) to extract total RNA. The isolated RNA, after quantification in Epoch Microplate Spectrometer (Agilent Technologies, USA), was reverse transcribed with TOPscript™ cDNA Synthesis Kit (Enzynomics, Republic of Korea). Later, qPCR was conducted using primers obtained from prior publications (Table 1) and SYBR Green TOPreal™ qPCR 2X PreMIX (Enzynomics, Republic of Korea) in Quantstudio 3 Real-Time PCR instrument (Applied Biosystems, USA). Both cDNA synthesis and qPCR were conducted according to the manufacturer's instructions. The relative expression level of each target gene was calculated using the comparative $2^{-\Delta\Delta}$CT method. GAPDH was taken as the reference gene.

Table 1. Primers used for qRT-PCR

Genes	Forward sequence	Reverse sequence
GAPDH	CGCTGAGTACGTCGTGGAGT	AGAGGGGGCAGAGATGATG
Occludin	CGGCAATGAAACAAAAGGCAG	GGCTATGGTTATGGCTATGGCTAC
Claudin-1	GTCTTTGACTCCTTGCTGAATCTG	CACCTCATCGTCTTCCAAGCAC

Media glucose and calcium quantification. The supernatants were collected and frozen at -80°C until used. Glucose, and calcium concentrations in the medium were measured using enzymatic assay kits (EIAGLUC from ThermoFisher Scientific for glucose, and MAK022 from Sigma for calcium detection. The assays were conducted following the manufacturer's instructions.

Preparation for drug treatment. Trastuzumab (Selleckchem, USA) was diluted into 10 μg mL^{-1} with the serum-free endothelial cell medium and applied to the flow channel reservoirs. The concentration was determined by referring to the reported *in vitro* inhibitory concentration of trastuzumab.[169]

Live imaging and live/dead assay. Macrophages were labeled with Far Red (1:1000; Invitrogen, USA), prior to live-cell imaging. Blood vessels were stained with fluorescein-conjugated Ulex Europaeus Agglutinin 1 (1:2000; Vector, USA), and SYTOXTM Blue (1:1000; Invitrogen, USA) was added to the culture medium immediately before imaging to label dead cells. Macrophages at a density of 4×10^6 cells mL^{-1} were attached to both sides of the central channel by tilting the device and incubated for at least 30 min. The motility and cytotoxic activities of macrophages were then monitored for 16 h with a Nikon Eclipse Ti2-E inverted microscope under 5% CO_2 at 37 °C.

Immunocytochemistry. The immunofluorescence imaging was performed to visualize cell-specific marker expression. The samples were fixed with 4% (w/v) PFA (Santa Cruz Biotechnology, San Diego, CA, USA) in PBS (Gibco, USA) for 15 min at RT, followed by permeabilization in 0.1% Triton X-100 (Sigma-Aldrich) for 15 min. The samples were then treated with 3% bovine serum albumin (BSA; Sigma-Aldrich) for 40 min. The following antibodies were used for immunocytochemistry and were incubated : AlexaFluor

594 conjugated mouse anti-CD31 (1:200; BioLegend), : AlexaFluor 647 conjugated mouse anti-CD31 (1:200; BioLegend), AlexaFluor 488 conjugated mouse anti-α-SMA (1:200; R&D systems), AlexaFluor 594 conjugated mouse anti-occludin (1:200; Invitrogen), mouse anti-FoxJ1 (1:200, Invitrogen), rabbit anti-RSPH9 (1:200, Sigma), and Hoechst 33342 (1:1,000; Invitrogen). Also, Alexa Fluor 488 Phalloidin was used to stain f-actin. They were all treated for 2 days at 4°C. Then samples were incubated with fluorescence conjugated secondary antibodies: goat anti-rabbit AlexaFluor 647 (1:200; Invitrogen) and goat anti-mouse AlexaFluor 594 (1:200; Invitrogen) for overnight at 4 °C for the target visualization. Fluorescently visualized samples were examined using a Ti2-Eclipse inverted microscope with NIS elements software (Nikon, Japan).

Statistical image analysis. Fiji (http://fiji.sc.), open access software, was used to analyze confocal images of each target visualization. Confocal 3D images were converted to 2D image by z-projection. The images for the area measurement are then converted to binary masked images by applying same condition of threshold. Finally, the area of the visualized targets including microvascular density, epithelial cells coverage, and cilia formation was measured using Fiji directly. To quantify cell viability based on the z-projection confocal images, the number of cancer cells and dead cells were counted by using the Fiji Cell Counter plugin. The macrophage movement was tracked using Chemotaxis and Migration Tool (https://ibidi.com/). All statistical analyses performed unpaired Student's t-test to obtain statistical comparisons of analyzed values. The p value thresholds for statistical significance were set and represented in the graph as *$p < 0.05$; **$p < 0.01$; ***$p < 0.005$; ****$p < 0.001$.

3.5 Supplementary Information

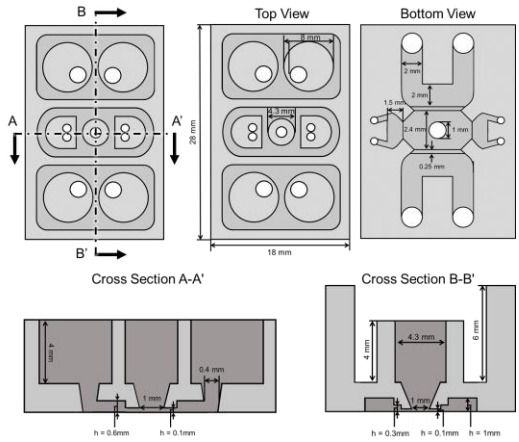

Figure S 16. Design of the human ChP-on-a-chip.

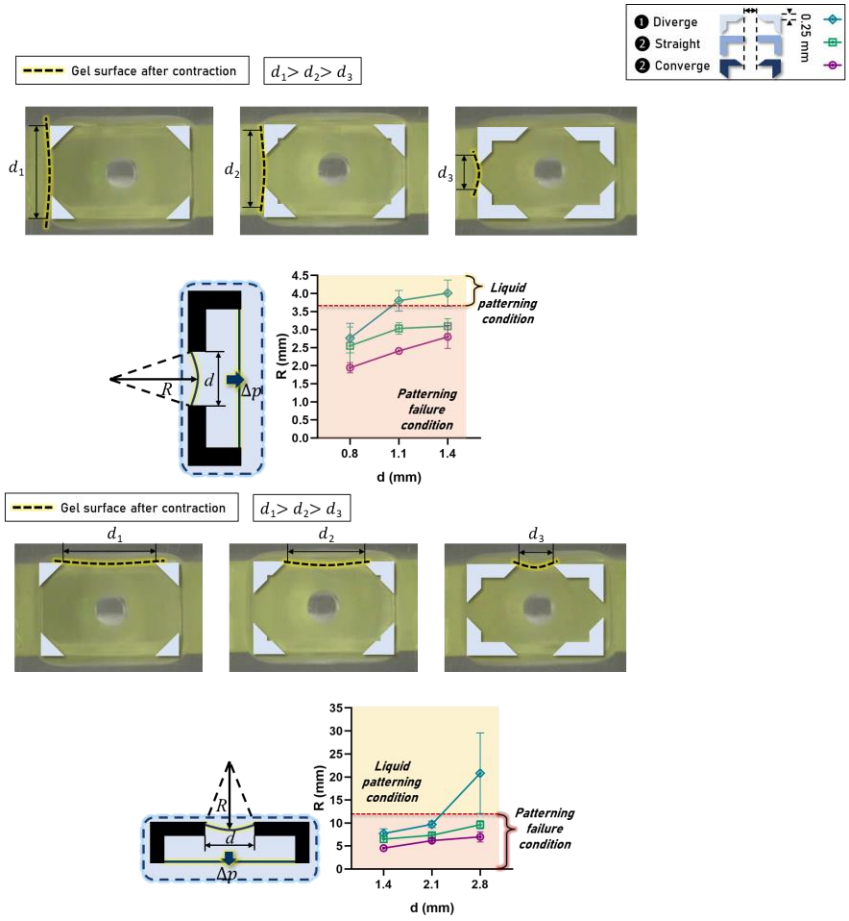

Figure S 17. Design rule of the microfluidic patterning in the human ChP-on-a-chip

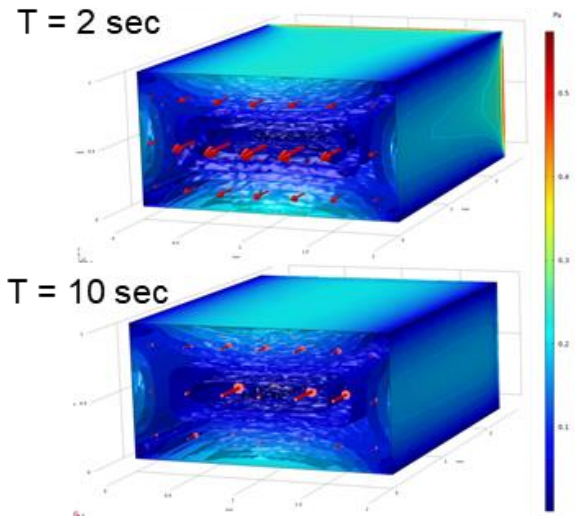

Figure S 18. Computer simulation for shear stress distribution in the microfluidic flow channel.

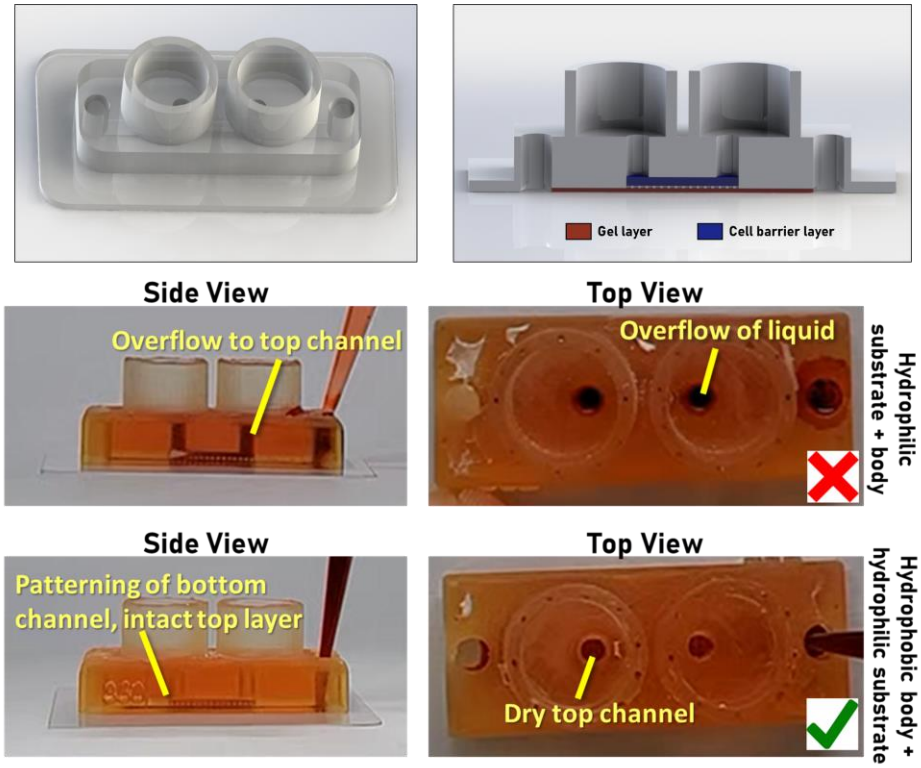

Figure S 19. Human ChP epithelium-on-a-chip

CHAPTER 4. CONCLUSIONS

4.1 Concluding Remarks

In this thesis, I have demonstrated two microfluidic platforms to recapitulate brain tumor microenvironments including primary brain tumors as well as brain metastasis. Microengineering technologies were used to recreate dynamic fluid flow, brain-specific ECM, and complex cellular architecture which played a key role in creating these devices. A microvascularized pediatric brain tumor-on-a-chip was developed by reconstituting a brain-specific ECM and co-culturing patient-derived pediatric brain tumor tissues with a microvascular network to improve its physiological relevance. This model presented the physiological relevance of microvasculature-brain tumor interaction and drug resistance. Next, using advanced engineering technologies, a human ChP-on-a-chip was developed. The device was designed to enable the construction of a complex capillaries – epithelium ChP system by establishing several design rules for microfluidic patterning. ECM engineering was applied to further recapitulate brain-specific ECM in this model. Furthermore, *in vivo*-like CSF flow was recreated by inducing dynamic flow using a rocker system. This physiologically relevant human ChP model allowed for the recapitulation of brain metastasis of breast cancer cells and investigating anti-cancer drug response and immune reaction in the brain tumor microenvironment of the ChP.

In summary, these microfluidic models to recapitulate the brain tumor microenvironment including various physical features can serve as a reliable tool for translational research in neuro-oncology.

4.2 Challenges and Future Work

4.2.1 Disease modelling by adjusting the dynamic flow

Our human ChP-on-a-chip recapitulated normal CSF flow dynamics based on data from healthy groups. Many neurological disorders such as hydrocephalus, idiopathic intracranial hypertension, traumatic brain injury, and ischaemic stroke are known to disrupt CSF circulation, and a significant disruption in the dynamic condition can provide life-threatening causes [170]. Since our human ChP-on-a-chip enables varying the parameters of flow dynamics, disrupted CSF flow can be recreated in our platform. The recapitulated pathophysiological CSF flow through these flow adjustments can contribute to disease modelling of various neurological diseases.

4.2.2 Hydrogel engineering

In our microvascularized pediatric brain tumor-on-a-chip, Matrigel was used to engineer ECM since the gel contains many brain-specific ECM components. However, Matrigel consists of undefined molecules where the uncertainty might cause imprecise results in the experiment. Thus, to overcome this limitation, laminin, one of the essential components of brain-specific ECM, was utilized to engineer ECM in the development of our human ChP-on-a-chip. Though the inclusion of laminin as a defined component to modify the ECM reduced the uncertainty of the results, there are more critical brain ECM components to be included to improve the physiological relevance of the brain microenvironment [18]. Engineering ECM for more characterization to reconstruct the brain-specific matrix may overcome these challenges.

4.2.3 Investigation of cellular behaviors on the epithelium

The current human ChP model recapitulated breast cancer cells spread in the capillaries of the ChP. For the further investigation of the disseminated cancer cells, the movement of the cells from the capillaries to the CSF through the epithelium can be observed using this model. This examination will contribute to a better understanding of the brain metastasis mechanism by circulating tumor cells in the CSF flow.

4.2.4 High-throughput drug screening

The microfluidic devices are created in the standardized well plate format which can allow for high-throughput drug screening. Also, though the current human ChP-on-a-chip is fabricated using 3D printing method, injection molding can be done to facilitate mass production of the device, which can allow for high-throughput testing.

APPENDIX A. FABRICATION OF THE HUMAN CHP-ON-A-CHIP

A.1 Experimental procedure to develop the human ChP-on-a-chip

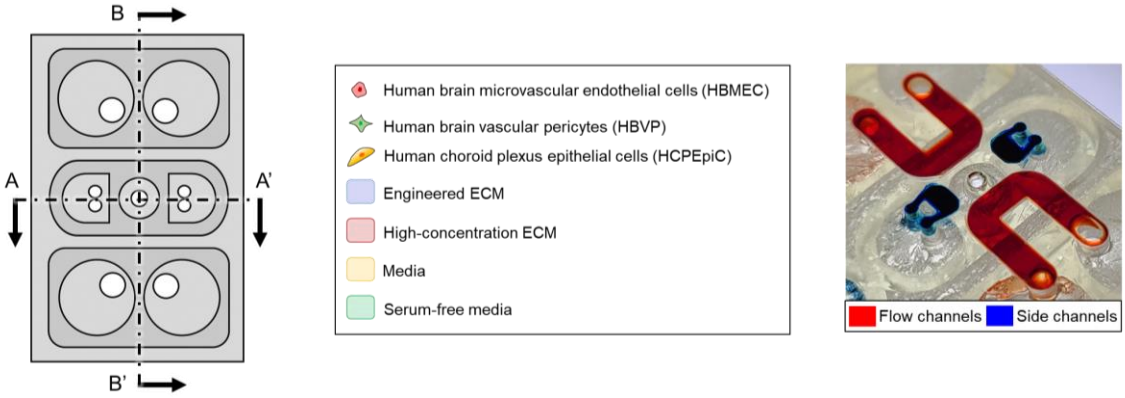

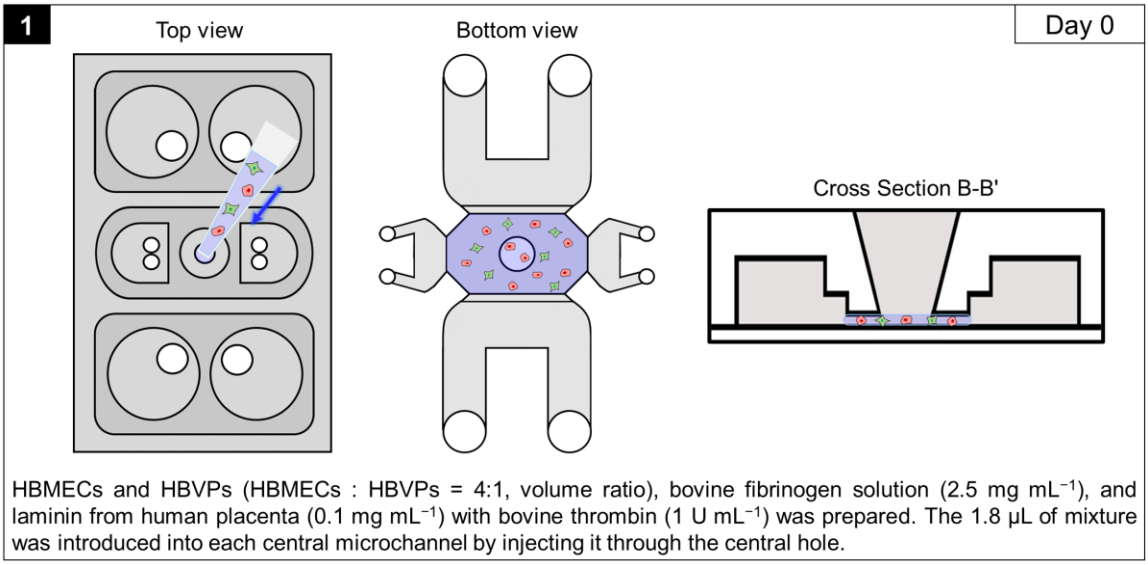

HBMECs and HBVPs (HBMECs : HBVPs = 4:1, volume ratio), bovine fibrinogen solution (2.5 mg mL^{-1}), and laminin from human placenta (0.1 mg mL^{-1}) with bovine thrombin (1 U mL^{-1}) was prepared. The 1.8 μL of mixture was introduced into each central microchannel by injecting it through the central hole.

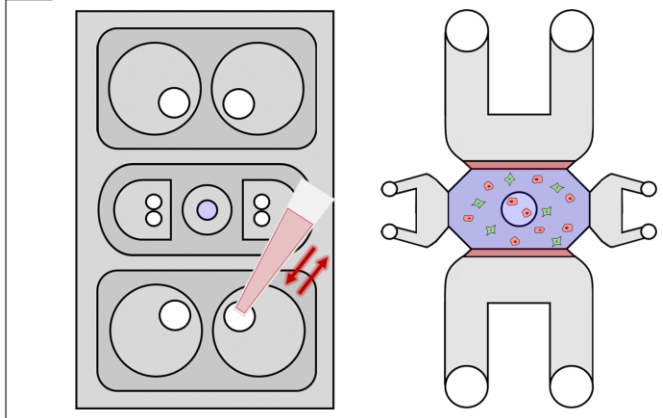

After allowing 10 min for the patterned mixture to cross-link at room temperature, the ECM with high concentration bovine fibrinogen solution (10 mg mL^{-1}) was introduced in the flow channels through the holes and aspirated to make the solution remain in the lower channels right next to the central channel, where the gel serves as a barrier between capillaries and epithelium.

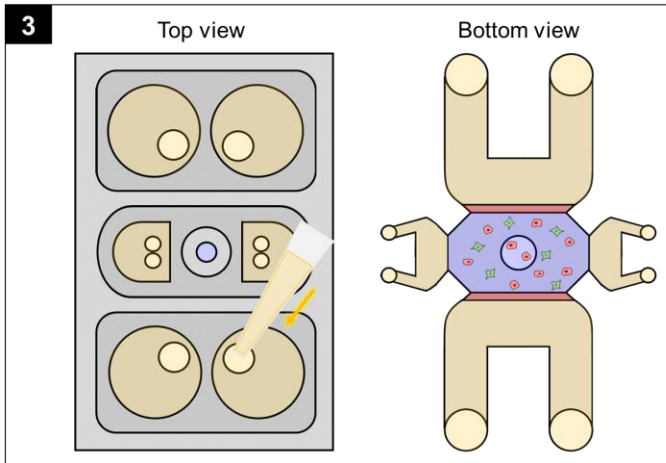

The endothelial cell medium supplemented with VEGF (50 ng mL^{-1}), FGF (20 ng mL^{-1}), EGF (20 ng mL^{1}) was prepared, and 200 µL of the medium was loaded in reservoirs after 10 min for cross-linking at room temperature

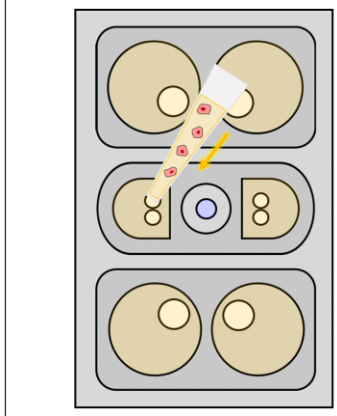

The endothelial cells were patterned to form perfusable blood vessels by injecting 10 µL suspension with HBMECs and HBVPs (HBMECs:HBVPs = 4:1, volume ratio) in the side channels and tilting the device by 90 degrees for 30 min in an incubator at 37 °C in 5% CO_2 to allow the cells to adhere on the gel surface in the central channels.

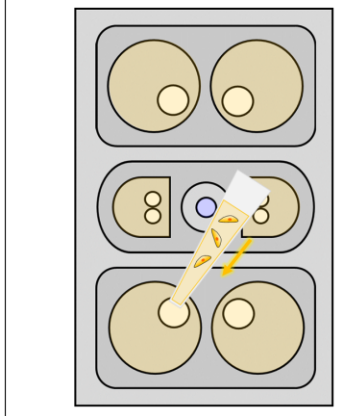

After 6 days culturing the HBMECs and HBVPs in an incubator at 37 °C in 5% CO_2, 20 µL suspension with HCPEpiCs was loaded in each flow channel and the chip was tilted by 90 degrees for 30 min in an incubator at 37 °C in 5% CO_2 to allow the cells to adhere on the gel surface to construct the ChP epithelium.

6

Day 8

Top view

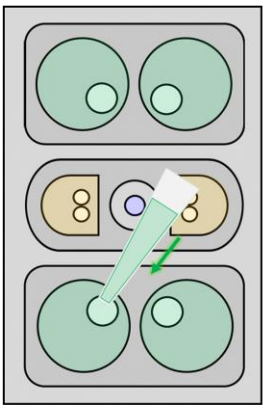

Bottom view

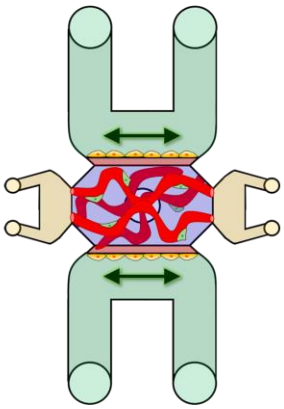

Cross Section B-B'

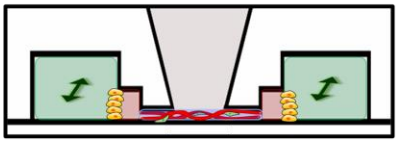

After 24 h to stabilize the epithelium, each reservoir of the flow channels was filled with 150 µL of the serum-free medium and the *in vivo*-like CSF flow was applied to the microfluidic chip by loading the platform on the rocker and culturing the system for 24 h in an incubator at 37 °C in 5% CO_2.

Day 9 culture completed

A.2 Experimental procedure to construct the tumor microenvironment in the human ChP-on-a-chip

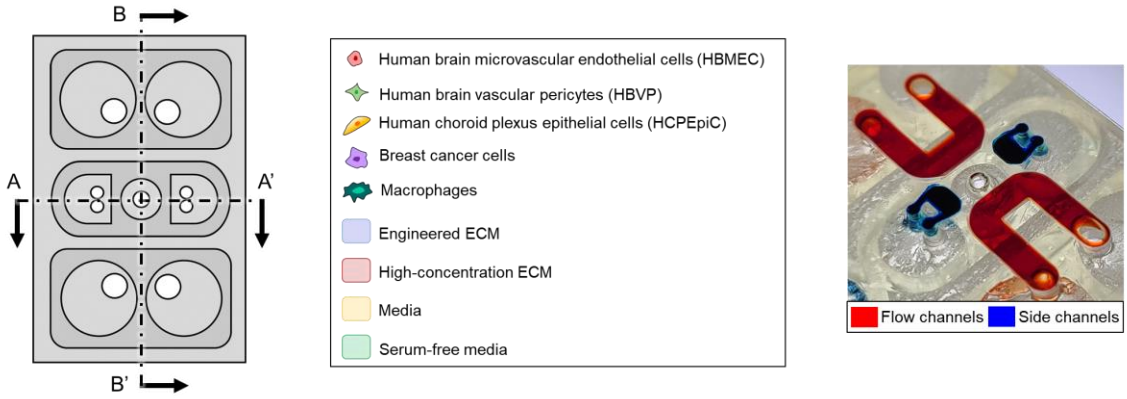

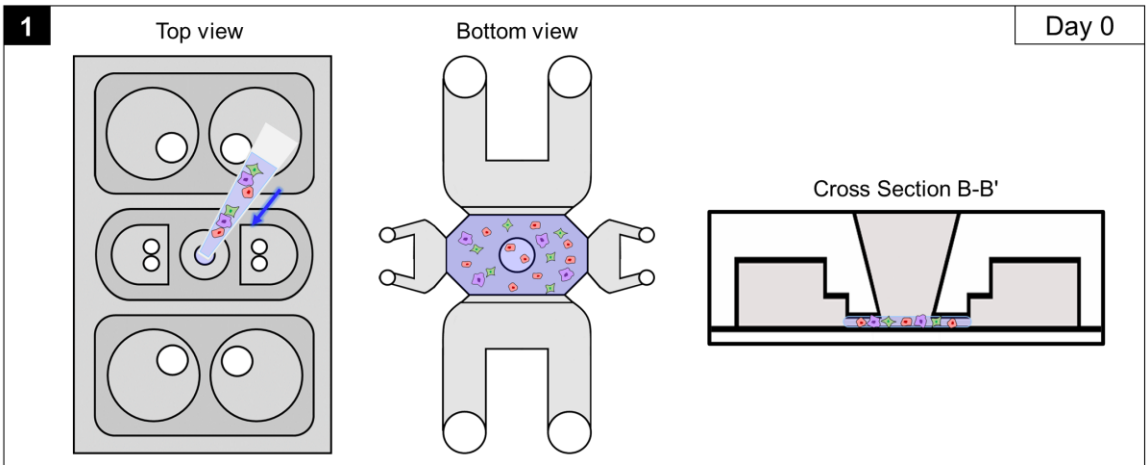

HBMECs, HBVPs, cancer cells (HBMECs : HBVPs:cancer cells = 8:2:1, volume ratio), bovine fibrinogen solution (2.5 mg mL^{-1}), and laminin from human placenta (0.1 mg mL^{-1}) with bovine thrombin (1 U mL^{-1}) was prepared. The 1.8 μL of mixture was introduced into each central microchannel by injecting it through the central hole.

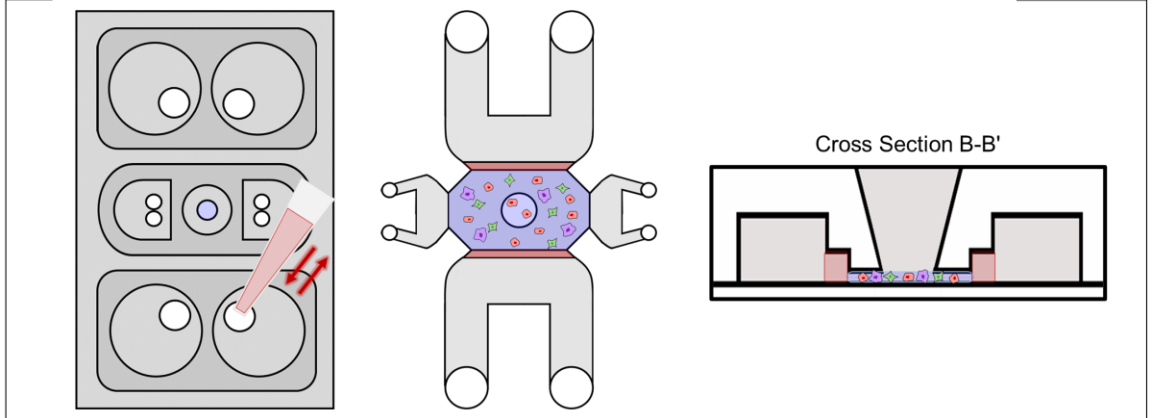

After allowing 10 min for the patterned mixture to cross-link at room temperature, the ECM with high concentration bovine fibrinogen solution (10 mg mL^{-1}) was introduced in the flow channels through the holes and aspirated to make the solution remain in the lower channels right next to the central channel, where the gel serves as a barrier between capillaries and epithelium.

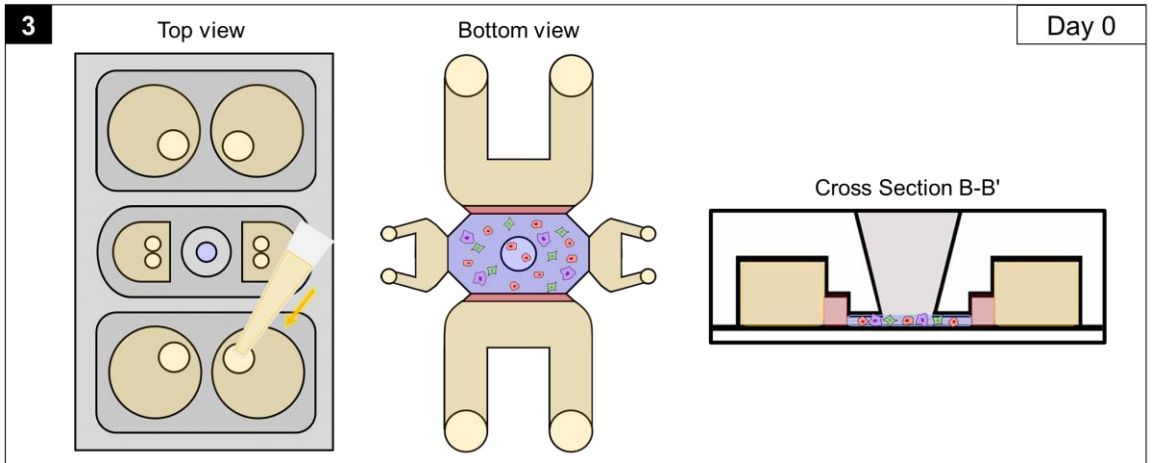

The endothelial cell medium supplemented with VEGF (50 ng mL^{-1}), FGF (20 ng mL^{-1}), EGF (20 ng mL^{1}) was prepared, and 200 µL of the medium was loaded in reservoirs after 10 min for cross-linking at room temperature

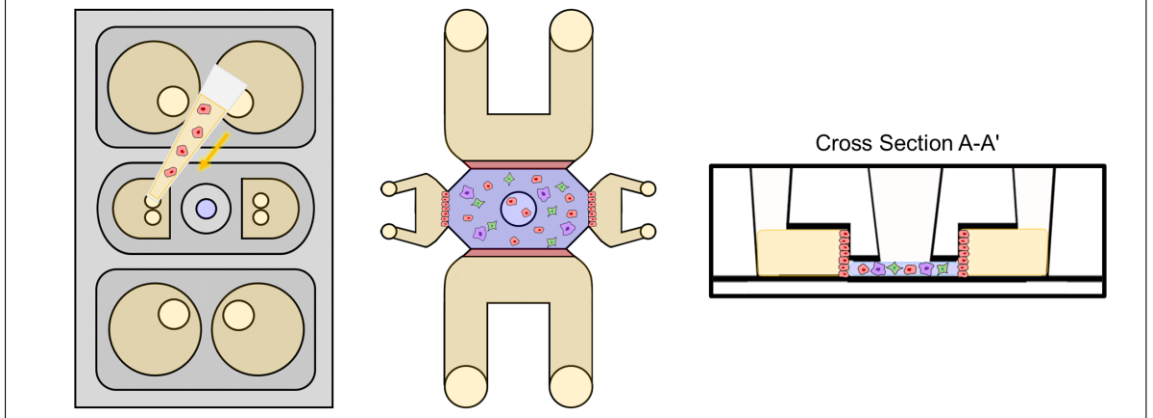

The endothelial cells were patterned to form perfusable blood vessels by injecting 10 µL suspension with HBMECs and HBVPs (HBMECs:HBVPs = 4:1, volume ratio) in the side channels and tilting the device by 90 degrees for 30 min in an incubator at 37 °C in 5% CO_2 to allow the cells to adhere on the gel surface in the central channels.

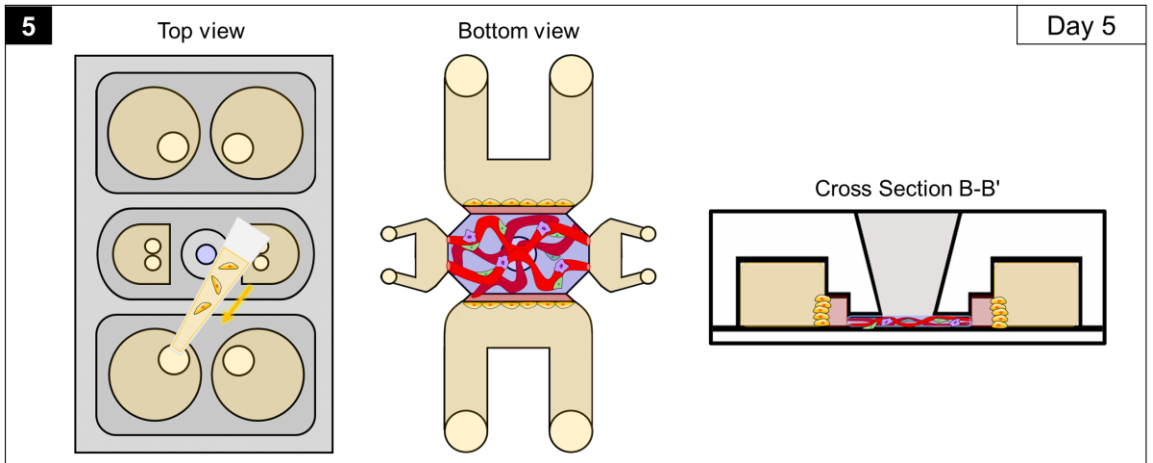

After 4 days culturing the HBMECs and HBVPs in an incubator at 37 °C in 5% CO_2, 20 µL suspension with HCPEpiCs was loaded in each flow channel and the chip was tilted by 90 degrees for 30 min in an incubator at 37 °C in 5% CO_2 to allow the cells to adhere on the gel surface to construct the ChP epithelium.

6 Day 6

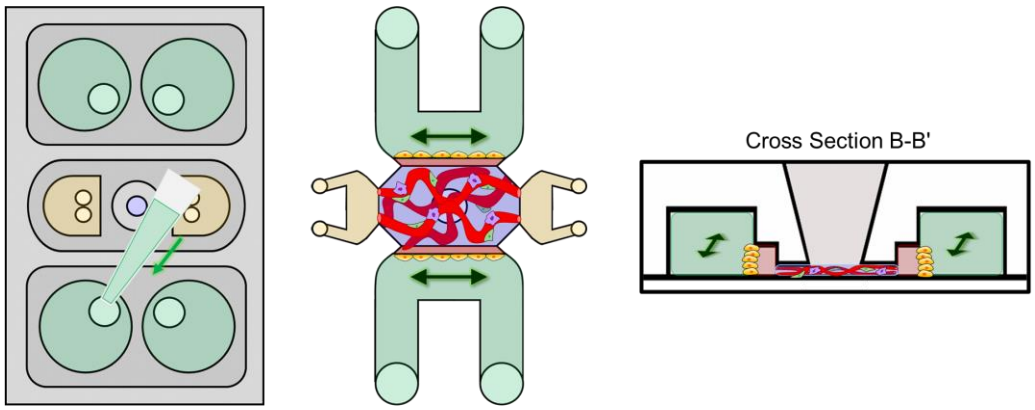

After 24 h to stabilize the epithelium, each reservoir of the flow channels was filled with 150 µL of the serum-free medium and the *in vivo*-like CSF flow was applied to the microfluidic chip by loading the platform on the rocker and culturing the system for 24 h in an incubator at 37 °C in 5% CO_2.

Day 7 culture completed

In the tumor-immune assay

7 Day 7

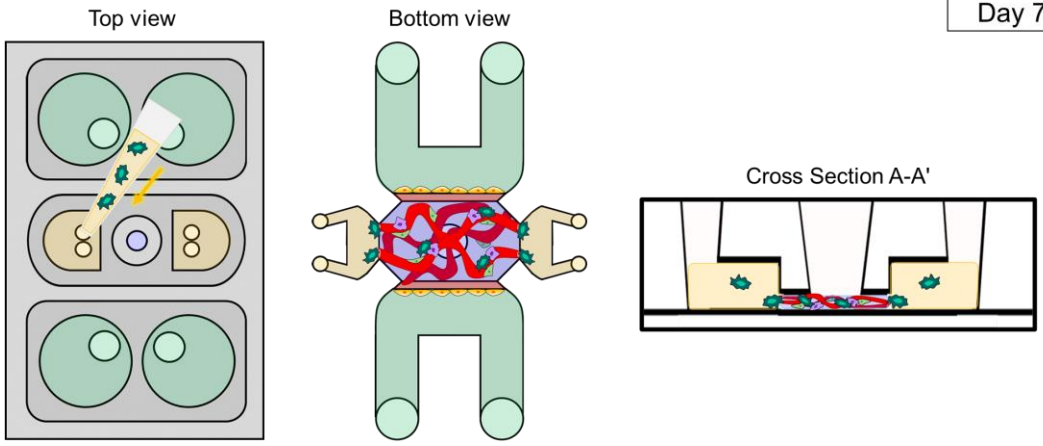

Macrophages at a density of 4×10^6 cells mL^{-1} were attached to both side channels by tilting the device and incubated for at least 30 min.

Day 8 culture completed

REFERENCES

1. Patel, A.P., et al., *Global, regional, and national burden of brain and other CNS cancer, 1990–2016: a systematic analysis for the Global Burden of Disease Study 2016.* The Lancet Neurology, 2019. **18**(4): p. 376-393.

2. Miller, K.D., et al., *Brain and other central nervous system tumor statistics, 2021*. CA: A Cancer Journal for Clinicians, 2021. **71**(5): p. 381-406.

3. Curtin, S.C., A.M. Minino, and R.N. Anderson, *Declines in Cancer Death Rates Among Children and Adolescents in the United States, 1999-2014.* NCHS Data Brief, 2016(257): p. 1-8.

4. Chaffer, C.L. and R.A. Weinberg, *A Perspective on Cancer Cell Metastasis.* Science, 2011. **331**(6024): p. 1559-1564.

5. Singh, R., et al., *Epidemiology of synchronous brain metastases.* Neuro-Oncology Advances, 2020. **2**(1).

6. Quail, D.F. and J.A. Joyce, *The Microenvironmental Landscape of Brain Tumors.* Cancer Cell, 2017. **31**(3): p. 326-341.

7. Kokkoris, C.P., *Leptomeningeal carcinomatosis: How does cancer reach the pia-arachnoid?* Cancer, 1983. **51**(1): p. 154-160.

8. Nia, H.T., L.L. Munn, and R.K. Jain, *Physical traits of cancer.* Science, 2020. **370**(6516): p. eaaz0868.

9. Helmlinger, G., et al., *Solid stress inhibits the growth of multicellular tumor spheroids.* Nature Biotechnology, 1997. **15**(8): p. 778-783.

10. Storm, C., et al., *Nonlinear elasticity in biological gels.* Nature, 2005. **435**(7039): p. 191-194.

11. Stylianopoulos, T., et al., *Diffusion Anisotropy in Collagen Gels and Tumors: The Effect of Fiber Network Orientation.* Biophysical Journal, 2010. **99**(10): p. 3119-3128.

12. Liesi, P., *Laminin-immunoreactive glia distinguish regenerative adult CNS systems from non-regenerative ones.* The EMBO journal, 1985. **4**(10): p. 2505-2511.

13. Deister, C., S. Aljabari, and C.E. Schmidt, *Effects of collagen 1, fibronectin, laminin and hyaluronic acid concentration in multi-component gels on neurite*

extension. Journal of Biomaterials Science, Polymer Edition, 2007. **18**(8): p. 983-997.

14. Lathia, J.D., et al., *Laminin alpha 2 enables glioblastoma stem cell growth.* Annals of Neurology, 2012. **72**(5): p. 766-778.

15. Menezes, M.J., et al., *The Extracellular Matrix Protein Laminin α2 Regulates the Maturation and Function of the Blood–Brain Barrier.* The Journal of Neuroscience, 2014. **34**(46): p. 15260-15280.

16. Thomsen, M.S., L.J. Routhe, and T. Moos, *The vascular basement membrane in the healthy and pathological brain.* Journal of Cerebral Blood Flow & Metabolism, 2017. **37**(10): p. 3300-3317.

17. Hudson, N. and M. Campbell, *Tight Junctions of the Neurovascular Unit.* Frontiers in Molecular Neuroscience, 2021. **14**.

18. Belousov, A., et al., *The Extracellular Matrix and Biocompatible Materials in Glioblastoma Treatment.* Frontiers in Bioengineering and Biotechnology, 2019. **7**.

19. Bhargav, A.G., et al., *Mechanical Properties in the Glioma Microenvironment: Emerging Insights and Theranostic Opportunities.* Frontiers in Oncology, 2022. **11**.

20. Chang, S.-F., et al., *Tumor cell cycle arrest induced by shear stress: Roles of integrins and Smad.* Proceedings of the National Academy of Sciences, 2008. **105**(10): p. 3927-3932.

21. Swartz, M.A. and A.W. Lund, *Lymphatic and interstitial flow in the tumour microenvironment: linking mechanobiology with immunity.* Nature Reviews Cancer, 2012. **12**(3): p. 210-219.

22. Emon, B., et al., *Biophysics of Tumor Microenvironment and Cancer Metastasis - A Mini Review.* Computational and Structural Biotechnology Journal, 2018. **16**: p. 279-287.

23. Langhans, S.A., *Three-Dimensional in Vitro Cell Culture Models in Drug Discovery and Drug Repositioning.* Frontiers in Pharmacology, 2018. **9**.

24. Drost, J. and H. Clevers, *Organoids in cancer research.* Nature Reviews Cancer, 2018. **18**(7): p. 407-418.

25. Park, S.E., A. Georgescu, and D. Huh, *Organoids-on-a-chip.* Science, 2019. **364**(6444): p. 960-965.

26. Lim, J., et al., *Microvascularized tumor organoids-on-chips: advancing preclinical drug screening with pathophysiological relevance.* Nano Convergence, 2021. **8**(1): p. 12.

27. Ahn, J., et al., *Tumor Microenvironment on a Chip: The Progress and Future Perspective.* Bioengineering, 2017. **4**(3).

28. Ingber, D.E., *Human organs-on-chips for disease modelling, drug development and personalized medicine.* Nature Reviews Genetics, 2022.

29. Zhang, B., et al., *Advances in organ-on-a-chip engineering.* Nature Reviews Materials, 2018. **3**(8): p. 257-278.

30. Xu, H., et al., *A dynamic in vivo-like organotypic blood-brain barrier model to probe metastatic brain tumors.* Scientific Reports, 2016. **6**(1): p. 36670.

31. Oliver, C.R., et al., *A platform for artificial intelligence based identification of the extravasation potential of cancer cells into the brain metastatic niche.* Lab on a Chip, 2019. **19**(7): p. 1162-1173.

32. Yi, H.-G., et al., *A bioprinted human-glioblastoma-on-a-chip for the identification of patient-specific responses to chemoradiotherapy.* Nature Biomedical Engineering, 2019. **3**(7): p. 509-519.

33. Truong, D., et al., *A three-dimensional (3D) organotypic microfluidic model for glioma stem cells – Vascular interactions.* Biomaterials, 2019. **198**: p. 63-77.

34. Xiao, Y., et al., *Ex vivo Dynamics of Human Glioblastoma Cells in a Microvasculature-on-a-Chip System Correlates with Tumor Heterogeneity and Subtypes.* Advanced Science, 2019. **6**(8): p. 1801531.

35. Le Rhun, E., et al., *Molecular targeted therapy of glioblastoma.* Cancer Treatment Reviews, 2019. **80**: p. 101896.

36. Schulz, M., et al., *Microenvironmental Regulation of Tumor Progression and Therapeutic Response in Brain Metastasis.* Frontiers in Immunology, 2019. **10**.

37. Sampson, J.H., et al., *Brain immunology and immunotherapy in brain tumours.* Nature Reviews Cancer, 2020. **20**(1): p. 12-25.

38. Nakano, I. and H.I. Kornblum, *Brain Tumor Stem Cells.* Pediatric Research, 2006. **59**(4): p. 54-58.

39. Auffinger, B., et al., *The role of glioma stem cells in chemotherapy resistance and glioblastoma multiforme recurrence.* Expert Review of Neurotherapeutics, 2015. **15**(7): p. 741-752.

40. Boussommier-Calleja, A., et al., *Microfluidics: A New Tool for Modeling Cancer–Immune Interactions.* Trends in Cancer, 2016. **2**(1): p. 6-19.

41. Javed, K., V. Reddy, and F. Lui, *Neuroanatomy, Choroid Plexus*. 2021: StatPearls Publishing, Treasure Island (FL).

42. Wong, C.H., K.W. Siah, and A.W. Lo, *Estimation of clinical trial success rates and related parameters.* Biostatistics, 2018. **20**(2): p. 273-286.

43. Kaur, R., P. Sidhu, and S. Singh, *What failed BIA 10–2474 Phase I clinical trial? Global speculations and recommendations for future Phase I trials.* Journal of Pharmacology and Pharmacotherapeutics, 2016. **7**(3): p. 120-126.

44. Otrubova, K., C. Ezzili, and D.L. Boger, *The discovery and development of inhibitors of fatty acid amide hydrolase (FAAH).* Bioorganic & Medicinal Chemistry Letters, 2011. **21**(16): p. 4674-4685.

45. Callaway, E. and D. Butler, *Researchers question design of fatal French clinical trial.* Nature, 2016.

46. Pellegrini, L., et al., *Human CNS barrier-forming organoids with cerebrospinal fluid production.* Science, 2020. **369**(6500): p. eaaz5626.

47. Lyu, Z., et al., *A neurovascular-unit-on-a-chip for the evaluation of the restorative potential of stem cell therapies for ischaemic stroke.* Nature Biomedical Engineering, 2021. **5**(8): p. 847-863.

48. Pellegrini, L. and M.A. Lancaster, *Breaking the barrier: In vitro models to study choroid plexus development.* Current Opinion in Cell Biology, 2021. **73**: p. 41-49.

49. Houghton, P.J., et al., *The pediatric preclinical testing program: Description of models and early testing results.* 2007. **49**(7): p. 928-940.

50. Taylor, M.D., et al., *Molecular subgroups of medulloblastoma: the current consensus.* Acta Neuropathologica, 2012. **123**(4): p. 465-472.

51. Liu, K.-W., et al., *Molecular mechanisms and therapeutic targets in pediatric brain tumors.* 2017. **10**(470): p. eaaf7593.

52. Placone, A.L., A. Quiñones-Hinojosa, and P.C. Searson, *The role of astrocytes in the progression of brain cancer: complicating the picture of the tumor microenvironment.* Tumor Biology, 2016. **37**(1): p. 61-69.

53. Tamayo-Orrego, L. and F. Charron, *Recent advances in SHH medulloblastoma progression: tumor suppressor mechanisms and the tumor microenvironment.* F1000Research, 2019. **8**: p. F1000 Faculty Rev-1823.

54. Jones, C., et al., *Pediatric high-grade glioma: biologically and clinically in need of new thinking.* Neuro-Oncology, 2016. **19**(2): p. 153-161.

55. Hermans, E. and E. Hulleman, *Patient-Derived Orthotopic Xenograft Models of Pediatric Brain Tumors: In a Mature Phase or Still in Its Infancy?* 2020. **9**(1418).

56. Kramer, J.A., J.E. Sagartz, and D.L. Morris, *The application of discovery toxicology and pathology towards the design of safer pharmaceutical lead candidates.* Nature Reviews Drug Discovery, 2007. **6**(8): p. 636-649.

57. Brabetz, S., et al., *A biobank of patient-derived pediatric brain tumor models.* Nature Medicine, 2018. **24**(11): p. 1752-1761.

58. Xu, J., et al., *Pediatric Brain Tumor Cell Lines.* 2015. **116**(2): p. 218-224.

59. Wenger, A., et al., *Stem cell cultures derived from pediatric brain tumors accurately model the originating tumors.* 2017. **8**(12).

60. Dobson, T.H.W. and V. Gopalakrishnan, *Preclinical Models of Pediatric Brain Tumors—Forging Ahead.* 2018. **5**(4): p. 81.

61. Ivanov, D.P., et al., *In vitro models of medulloblastoma: Choosing the right tool for the job.* Journal of Biotechnology, 2016. **236**: p. 10-25.

62. Dudu, V., et al., *Role of Epidermal Growth Factor-Triggered PI3K/Akt Signaling in the Migration of Medulloblastoma-Derived Cells.* Cellular and Molecular Bioengineering, 2012. **5**(4): p. 402-413.

63. Rico-Varela, J., et al., *EGF as a New Therapeutic Target for Medulloblastoma Metastasis.* Cellular and Molecular Bioengineering, 2015. **8**(4): p. 553-565.

64. Kim, S., et al., *Engineering of functional, perfusable 3D microvascular networks on a chip.* Lab on a Chip, 2013. **13**(8): p. 1489-1500.

65. Lee, S., et al., *Engineering tumor vasculature on an injection-molded plastic array 3D culture (IMPACT) platform.* Lab on a Chip, 2019. **19**(12): p. 2071-2080.

66. Mosesson, M.W., *Fibrinogen and fibrin structure and functions.* Journal of Thrombosis and Haemostasis, 2005. **3**(8): p. 1894-1904.

67. Mühleder, S., et al., *The role of fibrinolysis inhibition in engineered vascular networks derived from endothelial cells and adipose-derived stem cells.* Stem Cell Research & Therapy, 2018. **9**(1): p. 35.

68. Nagy, Z., et al., *Contraction of human brain endothelial cells induced by thrombogenic and fibrinolytic factors. An in vitro cell culture model.* Stroke, 1995. **26**(2): p. 265-70.

69. Collen, A., et al., *Membrane-type matrix metalloproteinase-mediated angiogenesis in a fibrin-collagen matrix.* Blood, 2003. **101**(5): p. 1810-1817.

70. Lesman, A., et al., *Engineering vessel-like networks within multicellular fibrin-based constructs.* Biomaterials, 2011. **32**(31): p. 7856-7869.

71. Ito, K.-I., et al., *Expression of tissue-type plasminogen activator and its inhibitor couples with development of capillary network by human microvascular endothelial cells on matrigel.* Journal of Cellular Physiology, 1995. **162**(2): p. 213-224.

72. Song, J., et al., *Endothelial Basement Membrane Laminin 511 Contributes to Endothelial Junctional Tightness and Thereby Inhibits Leukocyte Transmigration.* Cell Reports, 2017. **18**(5): p. 1256-1269.

73. Uwamori, H., et al., *Integration of neurogenesis and angiogenesis models for constructing a neurovascular tissue.* Scientific Reports, 2017. **7**(1): p. 17349.

74. Rajasekar, S., et al., *IFlowPlate—A Customized 384-Well Plate for the Culture of Perfusable Vascularized Colon Organoids.* 2020. **32**(46): p. 2002974.

75. Toepke, M.W. and D.J. Beebe, *PDMS absorption of small molecules and consequences in microfluidic applications.* Lab on a Chip, 2006. **6**(12): p. 1484-1486.

76. Berthier, E., E.W.K. Young, and D. Beebe, *Engineers are from PDMS-land, Biologists are from Polystyrenia.* Lab on a Chip, 2012. **12**(7): p. 1224-1237.

77. Placone, A.L., et al., *Human astrocytes develop physiological morphology and remain quiescent in a novel 3D matrix.* Biomaterials, 2015. **42**: p. 134-143.

78. Sood, D., et al., *3D extracellular matrix microenvironment in bioengineered tissue models of primary pediatric and adult brain tumors.* Nature Communications, 2019. **10**(1): p. 4529.

79. Ridet, J.L., et al., *Reactive astrocytes: cellular and molecular cues to biological function.* Trends in Neurosciences, 1997. **20**(12): p. 570-577.

80. Sofroniew, M.V., *Molecular dissection of reactive astrogliosis and glial scar formation.* Trends in Neurosciences, 2009. **32**(12): p. 638-647.

81. Zamanian, J.L., et al., *Genomic Analysis of Reactive Astrogliosis.* The Journal of Neuroscience, 2012. **32**(18): p. 6391.

82. Kleinman, H.K., D. Philp, and M.P. Hoffman, *Role of the extracellular matrix in morphogenesis.* Current Opinion in Biotechnology, 2003. **14**(5): p. 526-532.

83. Philp, D., et al., *Complex Extracellular Matrices Promote Tissue-Specific Stem Cell Differentiation.* 2005. **23**(2): p. 288-296.

84. Kleinman, H.K. and G.R. Martin, *Matrigel: Basement membrane matrix with biological activity.* Seminars in Cancer Biology, 2005. **15**(5): p. 378-386.

85. Gjorevski, N., et al., *Designer matrices for intestinal stem cell and organoid culture.* Nature, 2016. **539**(7630): p. 560-564.

86. Broguiere, N., et al., *Growth of Epithelial Organoids in a Defined Hydrogel.* 2018. **30**(43): p. 1801621.

87. Heine, P., A. Ehrlicher, and J. Käs, *Neuronal and metastatic cancer cells: Unlike brothers.* Biochimica et Biophysica Acta (BBA) - Molecular Cell Research, 2015. **1853**(11, Part B): p. 3126-3131.

88. Zhu, Y. and L.F. Parada, *The Molecular and Genetic Basis of Neurological Tumours.* Nature Reviews Cancer, 2002. **2**(8): p. 616-626.

89. Gilbertson, R.J. and D.W. Ellison, *The Origins of Medulloblastoma Subtypes.* Annual Review of Pathology: Mechanisms of Disease, 2008. **3**(1): p. 341-365.

90. Walker, C., E. Mojares, and A. Del Río Hernández, *Role of Extracellular Matrix in Development and Cancer Progression.* 2018. **19**(10): p. 3028.

91. Roddy, E. and S. Mueller, *Late Effects of Treatment of Pediatric Central Nervous System Tumors.* Journal of Child Neurology, 2015. **31**(2): p. 237-254.

92. Wen, P.Y., et al., *Response Assessment in Neuro-Oncology Clinical Trials.* Journal of Clinical Oncology, 2017. **35**(21): p. 2439-2449.

93. Assimakopoulou, M., et al., *Microvessel density in brain tumors.* Anticancer research, 1997. **17**(6D): p. 4747-4753.

94. Charalambous, C., F.M. Hofman, and T.C. Chen, *Functional and phenotypic differences between glioblastoma multiforme—derived and normal human brain endothelial cells.* Journal of Neurosurgery, 2005. **102**(4): p. 699-705.

95. Guyon, J., et al., *The Normal and Brain Tumor Vasculature: Morphological and Functional Characteristics and Therapeutic Targeting.* 2021. **12**(125).

96. Onishi, M., et al., *Angiogenesis and invasion in glioma.* Brain Tumor Pathology, 2011. **28**(1): p. 13-24.

97. Singh, S.K., et al., *Identification of human brain tumour initiating cells.* Nature, 2004. **432**(7015): p. 396-401.

98. Barzegar Behrooz, A., A. Syahir, and S. Ahmad, *CD133: beyond a cancer stem cell biomarker.* Journal of Drug Targeting, 2019. **27**(3): p. 257-269.

99. Liu, G., et al., *Analysis of gene expression and chemoresistance of CD133+ cancer stem cells in glioblastoma.* Molecular Cancer, 2006. **5**(1): p. 67.

100. Woo, P., et al., *A multifaceted review of temozolomide resistance mechanisms in glioblastoma beyond O-6-methylguanine-DNA methyltransferase.* 2019. **2**(2): p. 68-82.

101. Calabrese, C., et al., *A Perivascular Niche for Brain Tumor Stem Cells.* Cancer Cell, 2007. **11**(1): p. 69-82.

102. Wang, J., et al., *CD133 negative glioma cells form tumors in nude rats and give rise to CD133 positive cells.* International Journal of Cancer, 2008. **122**(4): p. 761-768.

103. Ko, J., et al., *Tumor spheroid-on-a-chip: a standardized microfluidic culture platform for investigating tumor angiogenesis.* Lab on a Chip, 2019. **19**(17): p. 2822-2833.

104. Charles, N.A. and E.C. Holland, *The perivascular niche microenvironment in brain tumor progression.* Cell Cycle, 2010. **9**(15): p. 3084-3093.

105. Ahn, S.I., et al., *Microengineered human blood–brain barrier platform for understanding nanoparticle transport mechanisms.* Nature Communications, 2020. **11**(1): p. 175.

106. Hui, L., et al., *Mutant p53 in MDA-MB-231 breast cancer cells is stabilized by elevated phospholipase D activity and contributes to survival signals generated by phospholipase D.* Oncogene, 2006. **25**(55): p. 7305-7310.

107. Singh, S.K., et al., *Cancer stem cells in nervous system tumors.* Oncogene, 2004. **23**(43): p. 7267-7273.

108. Li, Z. and S.A. Langhans, *In Vivo and Ex Vivo Pediatric Brain Tumor Models: An Overview.* 2021. **11**(1051).

109. Burić, S.S., et al., *Modulation of Antioxidant Potential with Coenzyme Q10 Suppressed Invasion of Temozolomide-Resistant Rat Glioma In Vitro and In Vivo.* Oxidative Medicine and Cellular Longevity, 2019. **2019**: p. 3061607.

110. Samiei, E., et al., *Investigating Programmed Cell Death and Tumor Invasion in a Three-Dimensional (3D) Microfluidic Model of Glioblastoma.* 2020. **21**(9): p. 3162.

111. Herbener, V.J., et al., *Considering the Experimental Use of Temozolomide in Glioblastoma Research.* 2020. **8**(6): p. 151.

112. Zudaire, E., et al., *A Computational Tool for Quantitative Analysis of Vascular Networks.* PLOS ONE, 2011. **6**(11): p. e27385.

113. Lun, M.P., E.S. Monuki, and M.K. Lehtinen, *Development and functions of the choroid plexus–cerebrospinal fluid system.* Nature Reviews Neuroscience, 2015. **16**(8): p. 445-457.

114. Rua, R. and D.B. McGavern, *Advances in Meningeal Immunity.* Trends in Molecular Medicine, 2018. **24**(6): p. 542-559.

115. Javed, K., V. Reddy, and F. Lui, *Neuroanatomy, Choroid Plexus*, in *StatPearls [Internet]*. 2020, StatPearls Publishing.

116. Hagenlocher, C., et al., *Ciliogenesis and cerebrospinal fluid flow in the developing Xenopus brain are regulated by foxj1.* Cilia, 2013. **2**(1): p. 12.

117. Felten, D.L., M.K. O'Banion, and M.S. Maida, *6 - Ventricles and the Cerebrospinal Fluid*, in *Netter's Atlas of Neuroscience (Third Edition)*, D.L. Felten, M.K. O'Banion, and M.S. Maida, Editors. 2016, Elsevier: Philadelphia. p. 85-91.

118. Brinker, T., et al., *A new look at cerebrospinal fluid circulation.* Fluids and Barriers of the CNS, 2014. **11**(1): p. 10.

119. Bapuraj, J.R., et al., *Cerebrospinal fluid velocity amplitudes within the cerebral aqueduct in healthy children and patients with Chiari I malformation.* Journal of Magnetic Resonance Imaging, 2016. **44**(2): p. 463-470.

120. Bedussi, B., et al., *Paravascular spaces at the brain surface: Low resistance pathways for cerebrospinal fluid flow.* Journal of cerebral blood flow and metabolism : official journal of the International Society of Cerebral Blood Flow and Metabolism, 2018. **38**(4): p. 719-726.

121. De Bock, M., et al., *A new angle on blood–CNS interfaces: A role for connexins?* FEBS Letters, 2014. **588**(8): p. 1259-1270.

122. Wu, C., et al., *Endothelial basement membrane laminin α5 selectively inhibits T lymphocyte extravasation into the brain.* Nature Medicine, 2009. **15**(5): p. 519-527.

123. Luissint, A.-C., et al., *Tight junctions at the blood brain barrier: physiological architecture and disease-associated dysregulation.* Fluids and Barriers of the CNS, 2012. **9**(1): p. 23.

124. Gautam, J., X. Zhang, and Y. Yao, *The role of pericytic laminin in blood brain barrier integrity maintenance.* Scientific Reports, 2016. **6**(1): p. 36450.

125. Kaur, R., P. Sidhu, and S. Singh, *What failed BIA 10-2474 Phase I clinical trial? Global speculations and recommendations for future Phase I trials.* Journal of pharmacology & pharmacotherapeutics, 2016. **7**(3): p. 120-126.

126. Bird, S.M., et al., *Statistical issues in first-in-human studies on BIA 10-2474: Neglected comparison of protocol against practice.* Pharmaceutical Statistics, 2017. **16**(2): p. 100-106.

127. Mukhopadhyay, M., *Recreating the blood–CNS barrier in vitro.* Nature Methods, 2020. **17**(9): p. 875-875.

128. Zagouri, F., et al., *Intrathecal administration of trastuzumab for the treatment of meningeal carcinomatosis in HER2-positive metastatic breast cancer: a systematic review and pooled analysis.* Breast Cancer Research and Treatment, 2013. **139**(1): p. 13-22.

129. Maximiano, S., et al., *Trastuzumab in the Treatment of Breast Cancer.* BioDrugs, 2016. **30**(2): p. 75-86.

130. Mack, F., et al., *Therapy of leptomeningeal metastasis in solid tumors.* Cancer Treatment Reviews, 2016. **43**: p. 83-91.

131. Grossman, S.A. and M.J. Krabak, *Leptomeningeal carcinomatosis.* Cancer Treatment Reviews, 1999. **25**(2): p. 103-119.

132. Yano, S., et al., *Expression of Vascular Endothelial Growth Factor Is Necessary but not Sufficient for Production and Growth of Brain Metastasis1.* Cancer Research, 2000. **60**(17): p. 4959-4967.

133. TABOURET, E., et al., *Recent Trends in Epidemiology of Brain Metastases: An Overview.* Anticancer Research, 2012. **32**(11): p. 4655-4662.

134. Romond, E.H., et al., *Trastuzumab plus Adjuvant Chemotherapy for Operable HER2-Positive Breast Cancer.* New England Journal of Medicine, 2005. **353**(16): p. 1673-1684.

135. Greitz, D., *Cerebrospinal fluid circulation and associated intracranial dynamics. A radiologic investigation using MR imaging and radionuclide cisternography.* Acta radiologica. Supplementum, 1993. **386**: p. 1-23.

136. Bateman, G.A., et al., *The pathophysiology of the aqueduct stroke volume in normal pressure hydrocephalus: can co-morbidity with other forms of dementia be excluded?* Neuroradiology, 2005. **47**(10): p. 741-748.

137. Wagshul, M.E., et al., *Amplitude and phase of cerebrospinal fluid pulsations: experimental studies and review of the literature.* Journal of Neurosurgery JNS, 2006. **104**(5): p. 810-819.

138. Stoquart-ElSankari, S., et al., *Aging Effects on Cerebral Blood and Cerebrospinal Fluid Flows.* Journal of Cerebral Blood Flow & Metabolism, 2007. **27**(9): p. 1563-1572.

139. W G Bradley, J., et al., *Normal-pressure hydrocephalus: evaluation with cerebrospinal fluid flow measurements at MR imaging.* Radiology, 1996. **198**(2): p. 523-529.

140. BALÉDENT, O., et al., *Cerebrospinal Fluid Dynamics and Relation with Blood Flow: A Magnetic Resonance Study with Semiautomated Cerebrospinal Fluid Segmentation.* Investigative Radiology, 2001. **36**(7): p. 368-377.

141. Wagshul, M.E., P.K. Eide, and J.R. Madsen, *The pulsating brain: A review of experimental and clinical studies of intracranial pulsatility.* Fluids and Barriers of the CNS, 2011. **8**(1): p. 5.

142. Strik, C., et al., *Intracranial oscillations of cerebrospinal fluid and blood flows: Analysis with magnetic resonance imaging.* Journal of Magnetic Resonance Imaging, 2002. **15**(3): p. 251-258.

143. Bailon, R., et al. *Analysis of Heart Rate Variability Using Time-Varying Frequency Bands Based on Respiratory Frequency*. in *2007 29th Annual International Conference of the IEEE Engineering in Medicine and Biology Society*. 2007.

144. Anrather, J., *Chapter 28 - Pathophysiology of the Peripheral Immune Response in Acute Ischemic Stroke*, in *Primer on Cerebrovascular Diseases (Second Edition)*, L.R. Caplan, et al., Editors. 2017, Academic Press: San Diego. p. 139-145.

145. Redzic, Z., *Molecular biology of the blood-brain and the blood-cerebrospinal fluid barriers: similarities and differences.* Fluids and Barriers of the CNS, 2011. **8**(1): p. 3.

146. Szmydynger-Chodobska, J., et al., *Expression of junctional proteins in choroid plexus epithelial cell lines: a comparative study.* Cerebrospinal Fluid Research, 2007. **4**(1): p. 11.

147. Kratzer, I., et al., *Complexity and developmental changes in the expression pattern of claudins at the blood–CSF barrier*. Histochemistry and Cell Biology, 2012. **138**(6): p. 861-879.

148. Steinemann, A., et al., *Claudin-1, -2 and -3 Are Selectively Expressed in the Epithelia of the Choroid Plexus of the Mouse from Early Development and into Adulthood While Claudin-5 is Restricted to Endothelial Cells.* Frontiers in Neuroanatomy, 2016. **10**.

149. Narita, K. and S. Takeda, *Cilia in the choroid plexus: their roles in hydrocephalus and beyond.* Frontiers in Cellular Neuroscience, 2015. **9**.

150. Telano, L.N. and S. Baker, *Physiology, Cerebral Spinal Fluid*. 2021: StatPearls Publishing, Treasure Island (FL).

151. Narita, K., et al., *Proteomic analysis of multiple primary cilia reveals a novel mode of ciliary development in mammals.* Biology Open, 2012. **1**(8): p. 815-825.

152. Brown, P.D., et al., *Molecular mechanisms of cerebrospinal fluid production.* Neuroscience, 2004. **129**(4): p. 955-968.

153. Artru, A.A., *Chapter 3 - CEREBROSPINAL FLUID*, in *Cottrell and Young's Neuroanesthesia (Fifth Edition)*, J.E. Cottrell and W.L. Young, Editors. 2010, Mosby: Philadelphia. p. 60-74.

154. Clarke, J.L., et al., *Leptomeningeal metastases in the MRI era.* Neurology, 2010. **74**(18): p. 1449-1454.

155. Le Rhun, E., S. Taillibert, and M.C. Chamberlain, *Carcinomatous meningitis: Leptomeningeal metastases in solid tumors.* Surgical neurology international, 2013. **4**(Suppl 4): p. S265-S288.

156. Witzel, I., et al., *Breast cancer brain metastases: biology and new clinical perspectives.* Breast Cancer Research, 2016. **18**(1): p. 8.

157. Bailleux, C., L. Eberst, and T. Bachelot, *Treatment strategies for breast cancer brain metastases.* British Journal of Cancer, 2021. **124**(1): p. 142-155.

158. Franzoi, M.A. and G.N. Hortobagyi, *Leptomeningeal carcinomatosis in patients with breast cancer.* Critical Reviews in Oncology/Hematology, 2019. **135**: p. 85-94.

159. Zagouri, F., et al., *Intrathecal administration of anti-HER2 treatment for the treatment of meningeal carcinomatosis in breast cancer: A metanalysis with meta-regression.* Cancer Treatment Reviews, 2020. **88**: p. 102046.

160. Huang, Q., et al., *Fluid shear stress and tumor metastasis.* American journal of cancer research, 2018. **8**(5): p. 763-777.

161. Takimoto, C.H., et al., *The Macrophage ‘Do not eat me’ signal, CD47, is a clinically validated cancer immunotherapy target.* Annals of Oncology, 2019. **30**(3): p. 486-489.

162. Nagel, T., et al., *Shear stress selectively upregulates intercellular adhesion molecule-1 expression in cultured human vascular endothelial cells.* The Journal of Clinical Investigation, 1994. **94**(2): p. 885-891.

163. Morigi, M., et al., *Fluid shear stress modulates surface expression of adhesion molecules by endothelial cells.* Blood, 1995. **85**(7): p. 1696-1703.

164. Klingen, T.A., et al., *Tumor-associated macrophages are strongly related to vascular invasion, non-luminal subtypes, and interval breast cancer.* Human Pathology, 2017. **69**: p. 72-80.

165. Morandi, A., et al., *The Colony-Stimulating Factor-1 (CSF-1) Receptor Sustains ERK1/2 Activation and Proliferation in Breast Cancer Cell Lines.* PLOS ONE, 2011. **6**(11): p. e27450.

166. Sousa, S., et al., *Human breast cancer cells educate macrophages toward the M2 activation status.* Breast Cancer Research, 2015. **17**(1): p. 101.

167. Qiu, S.-Q., et al., *Tumor-associated macrophages in breast cancer: Innocent bystander or important player?* Cancer Treatment Reviews, 2018. **70**: p. 178-189.

168. Upton, R., et al., *Combining CD47 blockade with trastuzumab eliminates HER2-positive breast cancer cells and overcomes trastuzumab tolerance.* Proceedings of the National Academy of Sciences, 2021. **118**(29): p. e2026849118.

169. Barok, M., et al., *Trastuzumab-DM1 causes tumour growth inhibition by mitotic catastrophe in trastuzumab-resistant breast cancer cells in vivo.* Breast Cancer Research, 2011. **13**(2): p. R46.

170. Bothwell, S.W., D. Janigro, and A. Patabendige, *Cerebrospinal fluid dynamics and intracranial pressure elevation in neurological diseases.* Fluids and Barriers of the CNS, 2019. **16**(1): p. 9.